MIT/WHOI

Massachusetts Institute of Technology
Woods Hole Oceanographic Institution

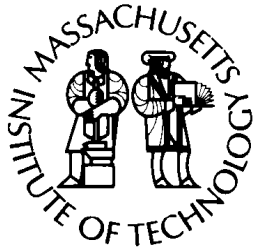

Joint Program in Oceanography/ Applied Ocean Science and Engineering

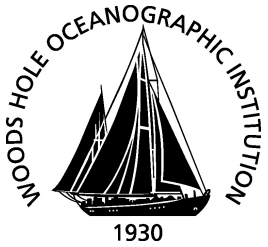

MASTER OF SCIENCE THESIS

Development and deployment of a novel deep-sea *in situ* bubble sampling instrument for understanding the fate of methane in the water column

by

Andrew S. Johnson

September 2019

Development and deployment of a novel deep-sea *in situ* bubble sampling instrument for understanding the fate of methane in the water column

by

Lieutenant Andrew S. Johnson

Submitted to the Joint Program in Applied Ocean Science & Engineering
in partial fulfillment of the requirements for the degree of
Master of Science in Mechanical Engineering
at the
MASSACHUSETTS INSTITUTE OF TECHNOLOGY
and the
WOODS HOLE OCEANOGRAPHIC INSTITUTION
September 2019

Author .....
Joint Program in Applied Ocean Science & Engineering
Massachusetts Institute of Technology
& Woods Hole Oceanographic Institution
August 9, 2019

Certified by .....
Scott D. Wankel
Associate Scientist
Department of Marine Chemistry & Geochemistry
Woods Hole Oceanographic Institution
Thesis Reader

Certified by .....
Henrik Schmidt
Professor
Mechanical Engineering Department
Massachusetts Institute of Technology
Thesis Reader

Certified by .....
Anna P. M. Michel
Associate Scientist
Department of Applied Ocean Physics & Engineering
Woods Hole Oceanographic Institution
Thesis Supervisor

Accepted by .....
Nicolas Hadjiconstantinou
Chair, Mechanical Engineering Committee for Graduate Students
Massachusetts Institute of Technology

Accepted by .....
David Ralston
Chair, Joint Committee for Applied Ocean Science & Engineering
Massachusetts Institute of Technology
Woods Hole Oceanographic Institution

Development and deployment of a novel deep-sea *in situ* bubble sampling instrument for understanding the fate of methane in the water column

by

Lieutenant Andrew S. Johnson

Submitted to the Joint Program in Applied Ocean Science & Engineering
Massachusetts Institute of Technology
& Woods Hole Oceanographic Institution
on August 9, 2019, in partial fulfillment of the
requirements for the degree of
Master of Science in Mechanical Engineering

Abstract

Methane (CH_4) is a potent greenhouse gas that is often found in a solid, hydrate clathrate form in marine sediments along continental margins and will often escape from the seafloor and rise through the water column as bubbles. The estimated marine methane hydrate inventory is over 600 times greater than the current atmospheric concentration so the fate of this ebullitive methane flux is of great interest. Traditional methods of measuring this flux such as acoustic imaging, optical sensors, and modeling suffer from limited information regarding the bubbles' composition. Studies that attempt to constrain CH_4 bubble composition suffer from low spatiotemporal resolution and adaptability. The current study presents the design, development and deployment of a novel, *in situ* bubble sampling system, the Bubble Delivery System (BDS), to quantify gas chemical composition in the water column. The BDS was deployed at the Cascadia Margin – a region well known for its active CH_4 bubble seeps – where 95 samples were collected from McArthur Ridge, Hydrate Ridge, Heceta Deep and Heceta Shallow over the course of seven remotely operated vehicle dives. By combining this approach with the use of an underwater mass spectrometer, *in situ* analysis of these samples indicated that the bubbles contained between 84.6 to 100% CH_4 and exhibited a high level of variability both spatially and temporally. Bubbles emitted from Heceta Deep exhibited anomalously elevated levels of carbon dioxide compared to the other sites.

Thesis Supervisor: Anna P. M. Michel
Title: Associate Scientist
Department of Applied Ocean Physics & Engineering
Woods Hole Oceanographic Institution

Acknowledgments

I have been incredibly fortunate to have the opportunity to participate in the Joint Program and have many people to thank. First, I'd like to thank my wife, Kathryn, for encouraging me to apply for this program in the midst of a particularly intense time at work. Even though we sacrifice a lot of time together, she still pushed me to attend fully knowing that the time commitment would be non-trivial and this tour would not be as "easy" as it could have been. If it were not for Kathryn's understanding and patience, I would never be in the place I am today.

Next, I'd like to think my advisor, Dr. Anna Michel, for providing the right mix of space and advice to get complete this project. She knew I had been out of academia for quite a while and might need a different kind of advising than her typical PhD students. She helped me understand the ins and outs of MIT academics and provided a great opportunity to work on a project that was far out of the realm of my experience. I've learned more about engineering and ocean science by working through this project than I would have doing a typical Navy project and that is one of the most valuable outcomes from me being here.

Scott Wankel was more of pseudo-advisor than just a collaborator. I appreciate your help in framing the project and providing feedback on the design as it developed. Your frequent reminders that the Falkor cruise was built around the BDS when the components were little more than CAD drawings and stock material were great motivation to get the work done!

I'd like to thank Dan Hoer for his assistance with the ISMS and helping me consider its integration with the BDS. Early in the project, he helped me test the feasibility of building the BDS and helped me tease out useful data in post processing. He devoted many hours in his busy schedule to run experiments with me where we discovered oddities in the ISMS data and figured out ways to back useful data out of it. Without his help and the use of Pete Girguis's lab at Harvard many of the insights about the cruise data would have been less developed or non-existent.

My lab mates have also played no small part in my success. I often joke Beckett was the reason I made it through my first semester at MIT, and its not far from the truth! Our optics study sessions made the class manageable and gave me the time to work on research and my other classes. In addition to academics, Beckett has taught me all of the basic electronics

and engineering that I know. When I had a question, he was always around and willing to fully devote his attention to my problem. I'm also grateful to Alexandra and Victoria for reading multiple iterations of my thesis, providing feedback on my code, and asking great questions in our lab meetings that significantly improved my research.

I could not have built the BDS without the help and oversight from the guys in Dunkworks and the WHOI machine shop. DC taught me how to use all of the equipment in Dunkworks and made at least 100 trips to the machine shop to help me find the tool I needed or make a cut for me. With Jim's insight, advice, and patience I learned basic craft and obscure techniques to make cuts or drill holes in places and angles that seemed impossible on first look. I think everyone in the shop has helped me at one point or another and I'm grateful for their willingness and time.

There were many other people in and around Blake that helped me with both technical and administrative problems. The Sentry team, especially Manyu Belani and Jason Fuji, provided critical advice designing oil compensated enclosures. Advice from Jason Kapit helped me form the BDS design foundations early in the project. John Bailey helped me rethink many design features to make them easier to use and was a life saver when building out the electronics. Judy Fenwick, Heather Moats, Celeste Simmons, and Karen Pipken all helped me navigate the WHOI administrative system and were always available to answer my questions. I appreciate the assistance and advice from the Joint Program and MIT Mechanical Engineering staff, especially Kris Kipp, Lea Fraser, and Leslie Regan, in their help navigating all of the Joint Program administration.

My funding was provided by the United States Navy's CIVINS program through the MIT/WHOI Joint Program. I am grateful to the United States Navy for allowing me to attend this program and meet so many smart, talented people. This project was funded by the National Science Foundation (OCE#1443683).

Contents

THIS PAGE INTENTIONALLY LEFT BLANK

List of Figures

List of Tables

THIS PAGE INTENTIONALLY LEFT BLANK

List of Algorithms

THIS PAGE INTENTIONALLY LEFT BLANK

Chapter 1

Introduction

1.1 Motivation

While carbon dioxide (CO_2) often receives widespread attention as the primary driver of climate change, methane (CH_4) also plays a critical role [1–4]. CH_4 is over 30 times more potent of a greenhouse gas and has a radiative efficiency 1000 $^{W}/_{m^2\text{-}ppb}$ greater than CO_2 [5]. While CO_2 accounts for over 60% of atmospheric radiative forcing, its absolute atmospheric concentrations are approximately 213 times that of CH_4 [5]. According to the Intergovernmental Panel on Climate Change (IPCC), greater than 50% of atmospheric CH_4 comes from anthropogenic sources, but natural sources such as wetlands and thawing permafrost account for a large portion as well [5]. Once CH_4 is released to the atmosphere, its direct radiative effect is powerful but short lived. A single molecule of CH_4 has an average lifetime in the atmosphere of only 11 y before it is oxidized to water vapor and then CO_2 [6]. Other natural sources of CH_4 are large reservoirs stored as gas hydrate, a solid, ice-like state, along the continental margins and in frozen tundra in the northern latitudes (Figure 1-1) [3, 7]. Approximately 99% of the world's methane hydrate is stored in marine sediments and modern estimates place the total reservoir size at 1800 Gt C [1].

Methane clathrate hydrate (hereafter referred to as methane hydrate) is formed under high pressure, low temperature conditions by encaging CH_4 molecules in a matrix of water molecules [8]. In the ocean, the top of the hydrate stability zone (THSZ) begins in the water column usually around 300-500 meters below sea level (mbsl). Since temperature decreases and pressure continues to increase approaching the seafloor, the bottom of the hydrate stability zone (BHSZ) is located below the seafloor at the point where geothermal

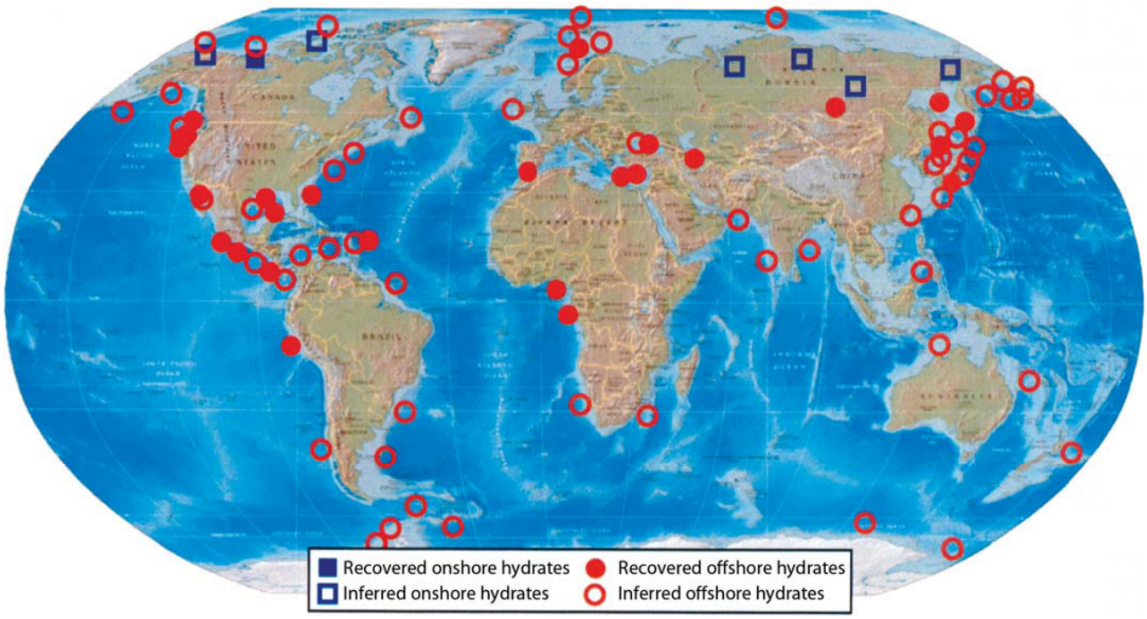

Figure 1-1: Map displaying the worldwide distribution of known and inferred methane hydrates. Figure reprinted from [3].

temperature surpasses the effect of increasing lithostatic pressure and gas hydrates are no longer stable (Figure 1-2) [1]. The extent of this zone from the THSZ to the BHSZ is known as the gas hydrate stability zone (GHSZ). With some exceptions (see Section 1.3.2), CH_4 within the GHSZ exists almost exclusively in its hydrate form, and when free gas escapes into the water column as bubbles, they form a hydrate film on the surface. Methane hydrates concentrate CH_4 gas into a much smaller volume than free gas. One square meter of methane hydrate contains over $170\,m^2$ of CH_4 gas, at standard temperature and pressure [1].

The existence of methane hydrates in marine sediment can often be inferred by acoustically imaged CH_4 bubble flares originating within the GHSZ or by seismic sediment reflection surveys [1]. The density of gas hydrate is typically less than that of the surrounding sediment so the change in the impedance of sound traveling through the sediment during a seismic survey results in a bottom simulating reflection (BSR) that is interpreted as the BHSZ [9, 10]. The International Ocean Drilling Program (IODP) has recovered many samples of gas hydrates sparsely distributed in the pore space of drill cores [11]. This finding has led to drastically reduced estimates of the world wide gas hydrate inventory which assumed that *all* of the available pore space in areas with BSRs were filled with hydrates [3].

With an atmospheric CH_4 concentration of approximately 3 Gt C, the estimated global inventory of methane hydrate has led to discussion of the potential climatological impacts

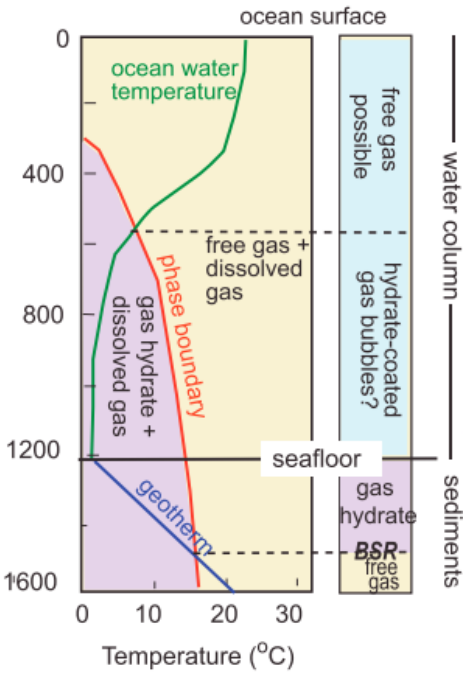

Figure 1-2: Schematic depicting the GHSZ. Hydrostatic pressure increases linearly with depth and the green line indicates water temperature. Inside the yellow zone, CH_4 exists in its gaseous state. Inside the purple zone, methane hydrates are stable. Once below the seafloor, the temperature increases until it it outside the GHSZ. Figure reprinted from [1].

if these reserves or a fraction thereof are rapidly released to the atmosphere due to warming ocean waters (in the case of marine reserves) or warming atmosphere (in the case of the terrestrial reserves) [6, 9, 12–16]. These discussions reference current rising temperature trends and historic thermal maximums shown in the paleoclimate record in which isotopically light carbon tracers indicated elevated levels of atmospheric CH_4 which could have caused global scale warming [2, 17, 18].

There is a continuous release of CH_4 gas bubbles from marine sediments in these methane hydrate rich continental margins that may be amplified by rising ocean temperatures [1, 6]. The ebullitive, or bubbling, CH_4 flux from the seafloor, into the shallow mixed layer, and ultimately into the atmosphere is poorly constrained. In order to understand the fate of the released CH_4 gas, it is important to know where the gas came from and how it is released into the water column. The following sections explore our current knowledge of the sources of CH_4 and methane hydrate in marine sediments (Section 1.2), the forcing mechanisms that cause its ebullition (Section 1.3), and a review of the studies that attempt to constrain its flux (Section 1.4).

1.2 Methane Sources in Marine Sediments

The origins of CH_4 in marine sediments are divided into two categories: biogenic and thermogenic [3, 4]. Both biogenic and thermogenic production find their sources in organic material, but biogenic CH_4 is created by biological processes whereas thermogenic CH_4 is created by geologic processes. Biogenic production takes place in the top layers of marine sediments over much shorter time scales (days) than thermogenic production [19]. Meanwhile, thermogenic production occurs thousands of meters below the seafloor over periods of centuries [20].

The source of the gas can be determined by measuring the ratio of carbon-13 to carbon-12 and comparing it to an internationally recognized reference material (Vienna Pee Dee Belemnite, VPDB). This comparison of ratios is expressed in delta notation ($\delta^{13}C$) and calculated by the following equation [21]:

$$\delta^{13}C(‰) = \left[\frac{\left({}^{13}C/{}^{12}C\right)_{measured}}{\left({}^{13}C/{}^{12}C\right)_{standard}} - 1 \right] \times 1000 \tag{1.1}$$

Methane gas from thermogenic sources tend to have a lower $\delta^{13}C$ (-20 to -50 ‰) than that from biogenic sources (-58 to -90 ‰). $\delta^{13}C$ between -50 to -58‰ is a result of biogenic and thermogenic source mixing [19, 22]. From these values, the predominant source of the CH_4 can be determined.

1.2.1 Biogenic Sources

The primary source of biogenic CH_4 in marine sediments is the remineralization of organic carbon by anaerobic microbes [23]. The last step of this remineralization is performed by a unique set of archaea known as methanogens and can be simplified to the following reaction [2, 4]:

$$CO_2 + 8H^+ + 8e^- \rightarrow CH_4 + 2H_2O \tag{1.2}$$

Organic carbon reduction in marine sediments is subject to a hierarchy of energetically favorable reactions. Valentine [4] describes this as the "redox ladder" in which a multitude of more thermodynamically favorable redox reactions occur before CO_2 is reduced to produce CH_4. In general, the ladder begins with oxygen (O_2) and is followed by nitrate, Mn(IV), Fe(III), $SO_4{}^{2-}$, and some halogenated organic compounds [4, 24]. Reduction of CO_2 to CH_4

is at the bottom of the ladder. Of all of these electron accepting species, the most abundant in marine sediment is SO_4^{2-} whose preferential reduction results in a notable CH_4 depletion zone in the top layers (Figure 1-3). This zone can vary from a few hundred centimeters [19] to several hundreds of meters along the continental margins where methane hydrates are known to occur [3, 25]. CH_4 can be oxidized by SO_4^{2-}, so any CH_4 that might be present is consumed [19]. Once the sulfate is depleted, net CH_4 generation can occur.

There is also a pathway for CH_4 production even in the sediment layers where SO_4^{2-} reduction is taking place. Fermentation of methyl amines and other organic sulphur compounds has been observed in sediment [4, 19]. The reaction typically takes the form:

$$CH_3 - A + H_2O \rightarrow CH_4 + CO_2 + A - H \tag{1.3}$$

where A represents the amine. While the extent of these reactions in marine sediments is unclear, they have been observed in several freshwater environments and salt marshes [19].

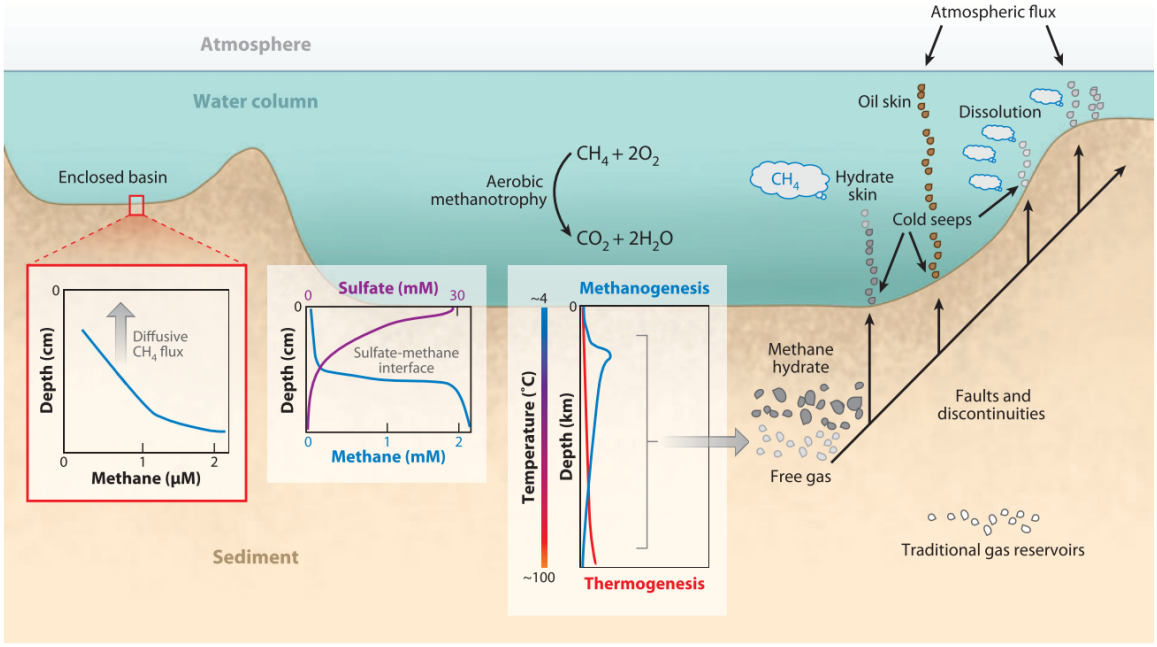

Figure 1-3: Summary of biogeochemical and transport processes affecting CH_4. Figure reprinted from [4].

1.2.2 Thermogenic Sources

Thermogenic CH_4 production begins with the deposition of organic material on the seafloor. As more material is deposited, prior deposits are compressed, heated, and pushed further below the seafloor where it is broken into smaller molecules. In general, the hydrocarbons produced get smaller with increasing depth. The organic materials that serve as the precursors for deep hydrocarbon production are known as kerogens and range from low molecular weight (i.e., algae and plankton) to high molecular weight (i.e., land plants) [20, 22]. Low molecular weight organic material is the precursor for type I kerogens while high molecular weight material forms type III kerogens [20]. At shallower depths (around 1500 m), heavier crude oil production from type I kerogens dominates. CH_4 production peaks much deeper (around 2500-5000 m) from mainly hydrogen-rich type III kerogens [20].

Types I and II kerogens can also lead to the production of CH_4, but it is not as common [19]. Once formed, hydrocarbons migrate up the lithostatic pressure gradient toward the seafloor. Lighter hydrocarbons such as CH_4 are more likely to reach the surface due to their greater buoyancy and ability to permeate sediments [20, 26].

1.3 Free Methane Forcing

When the thermogenic CH_4 nears the seafloor, it forms a reservoir of free gas below the BHSZ where it may mix with any biogenic CH_4 that is present and then migrates through the overlying sediment where it is released as bubbles in the water column [20, 27]. CH_4 bubble seeps are erratic in their intensity and periodicity [28] with reported hourly [28, 29], seasonal [29–31], and decadal [27] variability. The reasons for this ebuillitive variability are not well understood.

The basic mechanism by which gas is transported to the seafloor is by the formation of fractures in the sediment. Once the gas has reached the seafloor, its variability might be regulated by hydrostatic pressure. There are three predominant theories proposing how the transport from gas reservoirs to the seafloor occur and why the rate and occurrence might be variable: (1) seismic forcing (Section 1.3.1), (2) hydraulic forcing (Section 1.3.2), and (3) tidal forcing (Section 1.3.3). Seismic and hydraulic fracture theories outline possible transport mechanisms and seep periodicity while tidal forcing theory focuses on periodicity alone.

1.3.1 Seismic Forcing

The proposed mechanism for seismic forcing is rather simple – seismic activity places enough shear stress on the sediment to create fractures for gas to flow through [29]. Several studies have inferred earthquake driven CH_4 ebullition using various modeling techniques or observing bubble activity after a quake. Work by Kessler *et al.* [32] used radiocarbon dating and hindcast modeling to determine that an active CH_4 seep in the Cariaco Basin off the north-central coast of Venezuela began between 1958 and 1967. A moderate earthquake occurred in the Caribbean Sea 70 km northwest of the Cariaco Basin seep in 1967 that could have initiated the ebullition. In another study, Alpar [33] first noted a significant increase in bubble seep activity using ship-mounted multibeam sonar in the Gulf of Izmit, a small, isolated inlet off of the Sea of Mamara in northwest Turkey, after the large Kocaele Earquake in 1999. This increased seep activity has been confirmed and investigated further by several other studies [34–36]. Field and Jennings [37] presented evidence of seismic forced seep activity off the coast of northern California during an eight year survey of the Klamath River delta. In the middle of this survey (November 1980), an earthquake occured and the authors noted increased, short term (less than three years) gas ebullition using seismic reflection surveys and ship mounted side scan sonar. Finally, a study by Obzhirov *et al.* [38] using temporally sparse acoustic flare observations has indicated seismic activity may play an important role in bubble flare formation and periodicity in the Okhotsk Sea near Russia. These studies rely on multiple discrete observations or inference to establish the role of seismic activity in CH_4 ebullition, but better temporal resolution is needed to constrain its effect.

Many studies with enough temporal resolution and range to attempt to demonstrate the correlation between gas ebullition periodicity and seismic activity measure dissolved CH_4 concentration in pore fluid or acoustically image bubble flares. Elevated dissolved CH_4 concentration can result from methane-rich water flow from the sediments or from CH_4 bubbles dissolving as they rise through the water column. Thus, dissolved CH_4 concentration is a good proxy for the presence of bubbles, but it is not definitive. Some studies have reported increased dissolved CH_4 concentrations after earthquakes [32, 39] while some could not correlate observed periodicity with earthquakes at all [40, 41]; thus, using dissolved CH_4 activity to show a correlation between seep and seismic activity is fairly inconclusive. Acoustic imaging does not rely on proxies such as dissolved CH_4 for flare activity as the

backscatter from the CH_4 is directly observed. Only one study, performed by Römer *et al.* [29], has made continuous, long-term acoustic observations of a seep over a large temporal scale at Clayoquot Slope off the coast of Vancouver, Canada. Despite observing over 70 earthquakes during the year long study, no correlation could be found between bubble flare periodicity and seismic activity.

1.3.2 Hydraulic Fracture

Tryon *et al.* [42] describe a three-stage mechanism by which a reservoir of gas can fracture the hydrate boundary above it and can migrate to the surface (Figure 1-4). In stage one, the gas reservoir volume increases as it is fed by porous sediment passages from deeper sources and displaces pore fluid into the water column (Figure 1-5) [10, 27]. This migration has been studied in detail by IODP cruises, seismic reflection surveys [10, 11, 27], and numerical simulation [43]. In stage two, the volume of accumulated gas is large enough to fracture the sediments above the reservoir which allows the gas to rapidly escape [42]. In the final stage, the gas volume has decreased to a point that pore fluids can begin to flow back into the reservoir area. Eventually gas flow will stop and the process can begin again. This is a dynamic process that takes decades to complete. Daigle *et al.* [43] modeled the temporal scale by considering a wide array of dynamic factors including reservoir size and depth below the seafloor, water depth, and overlying sediment type at Hydrate Ridge, an extensively studied site off the coast of Oregon known for frequent methane seepage. The authors estimated that the three stages of hydraulic fracture takes 52-61 years at this site.

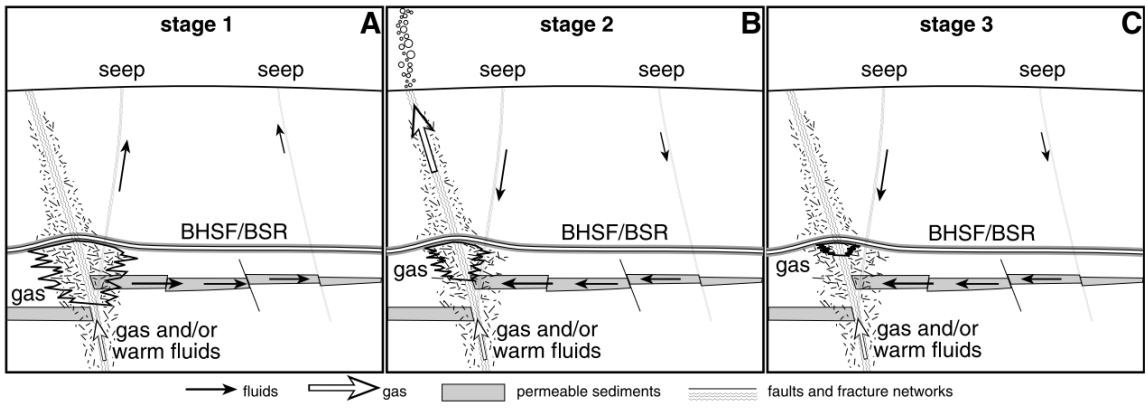

Figure 1-4: Schematic drawing depicting the stages of hydraulic fracture at Hydrate Ridge along the Cascadia Margin. Figure reprinted from [42].

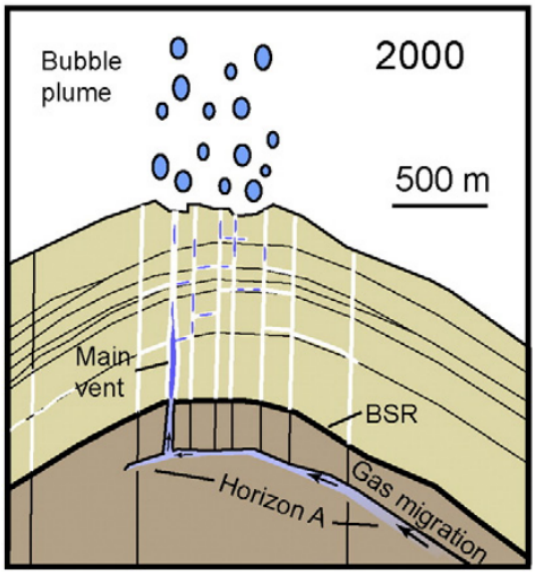

Figure 1-5: Illustration of the proposed migration path along porous sedimentary pathways at Hydrate Ridge. The migration pathway, "Horizon A," is identified as a second seismic reflection below the BSR [3, 27]. Image reprinted from [27].

The propagation of free gas through the GHSZ is confounding in the hydraulic fracture model. Intuitively, the gas traveling through the GHSZ would quickly form into methane hydrate and block flow. However, studies have shown that the gas can slowly migrate through fractures by forming hydrate boundaries around the channels that will separate the gas from the surrounding pore water – a key requirement of hydrate formation [44, 45]. Torres *et al.* [46] has altered the original fracture theory to include the fact that free gas can occur within the GHSZ. In this modified model, the possibility that the fracture can occur at a continuum of depths rather than just below the BSR is considered.

1.3.3 Tidal Forcing

Tidal forcing is the most widely observed cause of short-term methane bubble flare periodicity [29]. As with seismic forcing, there are few studies with the required temporal resolution to link tides with flare periodicity. However, tides are predictable whereas earthquakes are not. Several studies have noted a tidal component to the fluctuation in gas ebullition [29, 46–50] based on short term studies of hours to days, while some studies fail to establish a link [51]. Boles *et al.* [47] and Römer *et al.* [29] have quantified the relationship.

Boles *et al.* noted tidal components to the gas flux from a seep at a depth of 65 m at Coal

Point off the coast of California. The seep they studied was covered by a large metal "tent" that was already in place for collecting and pumping gas to a shore facility for industrial use. The researchers used the time dependent flow variability to the shore facility as a proxy for time dependent seep intensity. In the frequency spectrum of the fluctuations, the group noted strong peaks at 12 h, 12.4 h, 23.9 h, and 25.8 h corresponding to S2, M2, K1 and O1 tidal frequency constituents. In this study, the seep site was isolated from the change in hydrostatic pressure caused by the tidal cycle. Additionally, the ebullition could have been affected by the build up of gas at the top of the tent that may have created an artificially high pressure inside the tent after a vigorous release of bubbles.

Römer *et al.* [29] used a node of the Ocean Network Canada's North-East Pacific Time Series Underwater Networked Experiments (NEPTUNE) array at Clayoquot Slope (1250 mbsl) to quantify tidal contributions to CH_4 ebullition along the Cascadia Margin. The study collected approximately a year of continuous data from a rotating multibeam sonar that was co-located with a known bubble flare combined with a current meter and bottom pressure recorder. They found a 12.4 h periodicity in the seep which corresponds to the M2 tidal frequeny constituent. Interestingly, only one tidal cycle appeared to contribute to the periodicity at the deeper Clayoquot Slope seep. This may have been due to the fact that the range in tidally influenced pressure changes, as measured by the bottom pressure recorder at Clayoquot Slope, was only 0.15% of the hydrostatic pressure at 1250 m while the tidal pressure changes at Coal Point were 3.3% of the hydrostatic pressure at 65 m.

Tidal forcing models hinge on changes in hydrostatic pressure (P_H) with the rising and falling tides. Boles *et al.* [47] describe a pore activation model in which the change in hydrostatic pressure affects pore sizes differently. Römer *et al.* [29] reference a conduit dilation model in which the change in hydrostatic pressure, in tandem with changes in shear stress in the sediments, can form a pathway for gas release. These two models are explored in more detail below.

Pore Activation Model

In the bubble forcing model proposed in the Coal Point study, bubbles originate in a reservoir and travel in slugs to the surface after release through sediment pores into a fracture channel.

In this model, bubbles will be released if the following is true:

$$P_H < P_{ST} + P_F \tag{1.4}$$

where P_H is hydrostatic pressure, P_{ST} is the Laplace pressure of the bubble, and P_F is the fracture pressure [47]. Due to the viscous interaction between the gas and the surrounding sediment in the fracture, P_F decreases as the gas moves further from the source. P_{ST} is dependent on the surface tension (T) of a bubble and the bubbles radius (r) [47]:

$$P_{ST} = P_{inside} - P_{outside} = \frac{4T}{r_{bubble}} \tag{1.5}$$

As a bubble forms in a pore, P_{ST} and P_F increase until they reach the point at which the bubble is released into the fracture. When a bubble is released, $P_{ST} + P_F$ momentarily drops and the pore becomes inactive [3, 42, 47].

Conduit Dilation Model

The conduit dilation model proposes a dynamic physical change in the sediment rather than the bubbles as a mechanism for release (Figure 1-6). In the model, there is a conduit near the surface (formed as described in Section 1.3.1 or 1.3.2) from which the bubbles might be released based on the effective stress (σ') felt by the sediment:

$$\sigma' = \sigma - P_g \tag{1.6}$$

where P_g is the gas pressure in the sediment and σ is real stress. P_g is a function of P_H alone, while σ is a function of both P_H and lithostatic pressure [52]. As P_H decreases, the volume of the gas increases and the cavity in which the gas is held deforms. Conduit dilation occurs when σ' becomes negative and reaches the tensile limit of the sediment. The conduit dilation and cavity deformation work in tandem to release gas. If hydrostatic pressure increases to the compression limit (C), the conduit can plastically close [52].

1.3.4 Composite Mechanism

The three forcing mechanisms (seismic, hydraulic, and tidal) cannot individually characterize all CH_4 seep behavior. Most studies observe changes in flow that cannot be fully accounted

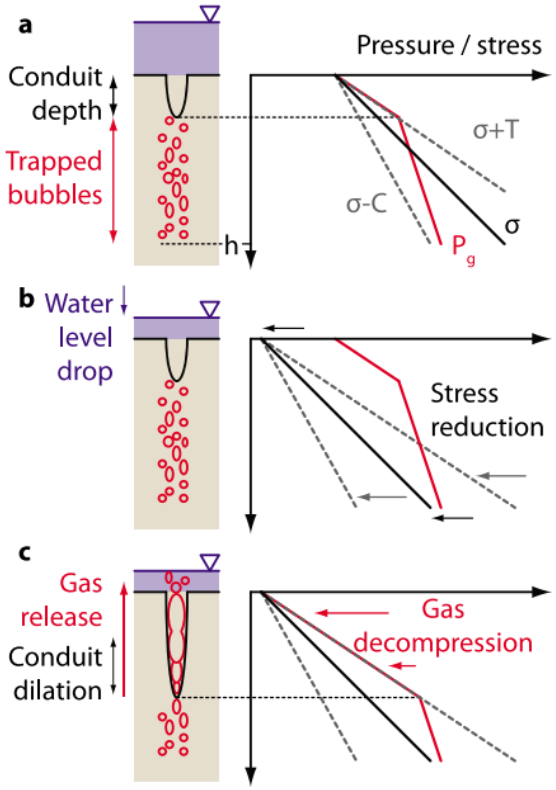

Figure 1-6: Depiction of the effect of water level drop on the conduit system. a) In the initial condition, the water level (shown in purple) is high and there are trapped bubbles below the conduit. The depth at which the conduit opens is when σ' reaches its tensile limit, $-T$. b) When water level drops, the stress on the system (mainly in the form of hydrostatic pressure) drops. For the purpose of this drawing, the gas pressure remains the same. c) In the final step of the model, the gas decompresses and the conduit opens at the depth dependent tensile limit. $T(h)$ increases linearly with depth in the sediment. Since the sediment stress is lower due to decreased hydrostatic pressure, σ' reaches its tensile limit deeper in the sediment. Thus, the conduit opening expands and allows gas to escape. Figure reprinted from [52].

for by tidal variation [27, 40, 46, 53]. Studies that try to constrain flow based on hydraulic or seismic fracture lack compelling data to definitively say that flare periodicity is due to either mechanism alone. However, if all three mechanisms are viewed in tandem, a more complete view of the erratic ebullition can be achieved.

The hydrate-coated gas transport fractures will not always be free flowing. The pathways can become capped by hydrate if the flow ebbs to the point where vertical water intrusion is allowed [11]. Indeed, evidence of these caps is readily seen in seismic imaging [27, 29] and by core samples showing bubble-textured hydrate deposits [10, 44–46]. Hydrate cap formation is dependent on reservoir gas pressure and thus will be highly unpredictable.

The caps would need to be fractured by hydraulic or seismic means in order for flow to continue. Additionally, reservoir gas pressure can have a great effect on a seep's sensitivity to hydrostatic pressure [10]. In a situation where the gas pressure is much greater than the hydrostatic pressure, flow will be vigorous and not susceptible to pressure changes. As the reservoir pressure approaches P_H, the seep will be more susceptible to the effects of changing P_H, and the seep will be more likely to form a hydrate cap that must then be hydraulically fractured.

1.4 Ebullitive Methane Flux in Marine Environments

The amount of CH_4 released from marine sediments that reaches the air-sea interface is poorly constrained. In shallow (< 200 m) or very vigorous bubble flares, a clear CH_4 flux at the air-sea interface can be observed [39, 54, 55]. However, it is often assumed that CH_4 from flares originating deeper than approximately 500 m does not make it to the ocean surface [1, 56, 57]. Since the early 2000's, there has been a significant effort attempting to constrain this problem [1, 39, 51, 55, 58–62].

The most common methods for determining bubble flare rise in the water column are acoustic imaging [26, 53, 56, 58, 60, 62–64], modeling [55, 65], and using optical instruments [59, 61, 66–68]. The purpose of these studies was to quantify the extent to which CH_4 is transported from the seafloor to the water column. In studies where acoustic imaging was used extensively, multibeam sonar was used to visualize how high in the water column the bubbles rise. This method was used to successfully determine that the bubbles do not often make it to the surface of the water. However, the sonar can have difficulty imaging the terminal stage of the bubble rise because the bubbles are much smaller and the sonar is tuned to image bubbles in the bulk of the flare.

Optical instruments track the rate of change of a bubble's radius once it is emitted from the seafloor. This method requires a remotely operated vehicle (ROV) to follow the bubble through the water column and to track how quickly the bubble shrinks or to remain stationary and observe the bubble flare at its source. Except in the most vigorous flares, it is difficult to find bubbles in the water column once above 10-20 m above the seafloor. In order to track the bubbles, Rehder *et al.* [59] surrounded the bubbles with a clear plastic box and followed them through the water column. This method was problematic because

the bubbles in the box are not experiencing the dynamic geochemical gradients and currents that a bubble normally would during its ascent, thus affecting the rate of bubble dissolution. Additionally, the rise rate of the bubble is biased upward due to the drag forces imposed by the box. The stationary optical methods rely on data from a single altitude and must extrapolate the rate of change of the bubble radius [61, 66–68]. In a bubble's rise, it may encounter a wide range of ambient conditions that may cause it to shrink at a rate different than at its source.

Both the acoustic imaging and optical instruments fail to consider the chemical composition of the bubble after it leaves the seafloor. The dissolved gas concentration in the water surrounding the bubbles is below saturation with respect to CH_4 so this extreme concentration gradient causes the CH_4 inside the bubble to diffuse into the water column. Gases already dissolved in the water column such as O_2, CO_2, and nitrogen (N_2) diffuse into the bubble and replace some of the volume that is lost [21, 65]. The gas exchange has been modeled in a few studies [55,65], but little work has been done to validate the models in the field. Leonte *et al.* [21] used the Texas A&M Oil spill (Outfall) Calculator (TAMOC) [69,70] to quantify the fraction of hydrocarbon gas remaining in a bubble released from a 890 m deep seep at different rise heights in the Gulf of Mexico. The authors used the natural stable carbon isotope fractionation that occurs when CH_4 dissolves from a bubble to determine the fraction of CH_4 that dissolved from a bubble flare into the surrounding water column at multiple depths and compared it to the remaining fraction of CH_4 predicted by TAMOC. The study found that within the first meter of bubble rise, 58.2±31.1% of the CH_4 had left the bubble and that 97.5±4.7% of the CH_4 had left the bubble after 766 m of bubble rise (124 mbsl).

Another method to constrain ebullitive CH_4 flux is to consider the chemical composition of a bubble once it has left the seafloor. Chemical composition analyses are not often performed because it is difficult to collect gas samples from the flare and analyze them. To date, few authors have performed chemical composition analysis on bubbles collected from a CH_4 flare. Leonte *et al.* [21] collected bubbles from a seep in the Gulf of Mexico with modified Niskin bottles attached to a ROV and brought them to the surface for separation by gas chromatography and compositional analysis by thermal conductivity and a flame ionization detector (FID). The collection apparatus allowed the bubbles to expand as the ROV returned to the surface and the compositional analyses were performed in a ship-board

laboratory. Baumberger *et al.* [71] collected bubble samples from the Cascadia Margin in the northeast Pacific in a custom gas-tight bottle connected to a ROV that did not allow the bubbles to expand as they were brought back to the surface. The authors analyzed the samples in a similar manner to Leonte *et al.* except the analyses were performed at a shore-based facility after the cruise.

These two studies were limited by their collection methods and *ex situ* chemical analyses. Both collection methods allowed for a limited number of samples to be collected on each dive. Leonte *et al.* were limited in the number of samples they could collect on each dive and only collected three samples in the entire study. Baumberger *et al.* dove with multiple gas-tight bottles that could only be used once per study since the chemical analyses were performed on shore. Additionally, the authors were limited by the number of collection bottles that could be brought on the dive and the cruise. As a result, the study only analyzed five samples. With all of the sample analyses occurring *ex situ* in both studies, the authors had no ability to employ dynamic sampling strategies based on real-time results from prior samples. Finally, the sparse sampling patterns that had to be employed because of resource-heavy sampling methods gave spatiotemporally limited results.

In order to improve the spatiotemporal range and resolution of bubble chemical composition studies, a sampling tool that can be used multiple times in a single dive is needed. If the samples are analyzed *in situ* and the operator has access to the real-time output from an *in situ* instrument, a dynamic sampling plan can be used to better characterize a CH_4 seep. This multi-use sampling tool with *in situ* analysis techniques will be limited by ROV dive time rather than the number of sample bottles. Michel *et al.* [72] successfully collected CO_2 bubbles and analyzed them with an *in situ* laser spectrometer that is used to measure carbon isotopes of CH_4, but this did not allow for the full characterization of a bubble's chemical composition.

An *in situ* mass spectrometer (ISMS) (e.g., Wankel *et al.* [73]) would be a more useful tool to characterize a bubble's chemical composition. The ISMS is a type of membrane inlet mass spectrometer (MIMS) in which a thin, semi-permeable membrane is used to allow dissolved gas from a sample stream to diffuse into the mass spectrometer for analysis. The ionization chamber and detector of the mass spectrometer are kept at an extremely high vacuum (10^{-5} Torr) thus the pressure gradient accross the membrane is immense. The instrument is built around a Stanford Research Systems Residual Gas Analyzer (SRS RGA100) in which

the ion signal of discrete ion mass charge ratios are plotted against time. SRS has developed proprietary software that provides a real-time display of the time course response of the instrument.

The goal of this thesis is to outline the development of a bubble delivery system (BDS) for collecting bubbles for analysis by the ISMS developed by Wankel *et al.* [73]. Chapter 2 outlines the design and development of the BDS. Chapter 3 describes first deployment of the BDS. The chemical composition results from the deployment are discussed in Chapter 4 and concluding remarks are presented in Chapter 5.

Chapter 2

Bubble Delivery System Design

The Bubble Delivery System (BDS) is designed to be manipulated by an ROV to sample and analyze bubbles *in situ* at depths of up to 1200 m. The construction of the BDS can be broken down into four major subsystems: (1) the deep-sea Bubble Acquisition Tool (SeaBAT), (2) the bubble accumulation chamber (BAC), (3) the high-pressure purge assembly (HPA), and (4) the component control circuitry. These four subsystems work in tandem to collect small aliquots of bubbles and deliver them to an *in situ* mass spectrometer for analysis (Figure 2-1). This chapter will begin with a brief overview of the operation of the BDS (Section 2.1), followed by general design decisions (Section 2.2), and finally by a detailed discussion of each of the subsystems (Sections 2.3 – 2.6).

2.1 BDS Overview

The first step of the bubble sampling workflow (Figure 2-2) is accomplished by the SeaBAT. The SeaBAT is deployed by the ROV manipulator arm to collect bubbles for analysis and is built around a low pressure, four port, two position stream selector valve (C45R-8144; Valco Instruments Company Incorporated, Houston, TX). Bubbles are collected in a funnel that is attached to the exterior of the valve enclosure and enter the head of the valve via passive buoyant forces. If operating in the GHSZ, the bubbles may have a hydrate shell that must be melted before rising into the valve head by a heater that is integrated in the SeaBAT. To collect a bubble sample, the valve is cycled and the bubble is placed inline with the discharge of a variable speed, bi-directional gear pump (McLane Research Laboratories, East Falmouth, MA) whose suction source is ambient seawater. Design specifics and sampling

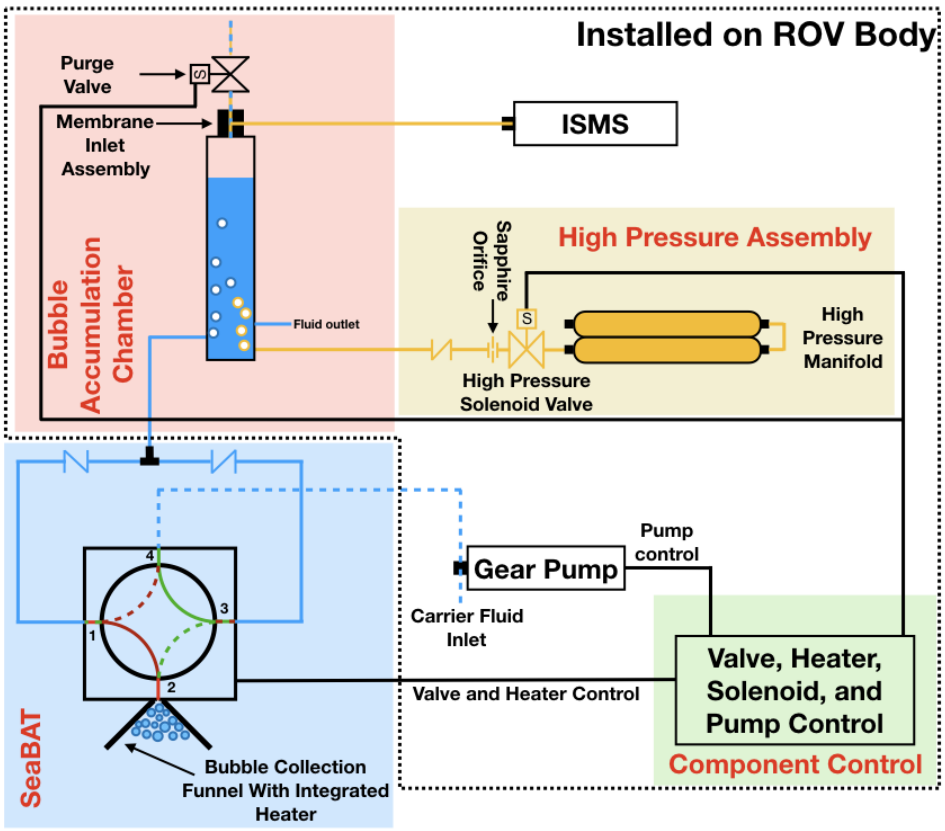

Figure 2-1: Overview of the BDS shown coupled to the ISMS. Blue lines indicate fluid flow paths, yellow lines indicate gas flow paths, and black lines indicate electrical connections. Individual BDS components are labeled in red. In the SeaBAT, red lines indicate Groove A and green lines indicate Groove B. Solid lines indicate groove connections in Position 1 and dashed lines indicate Position 2.

flow paths of the SeaBAT are detailed in Section 2.3.

After a bubble sample has been collected by the SeaBAT, the gear pump is used to transfer the sample to the BAC at 125 $^{mL}/_{min}$. The BAC consists of a collection chamber, membrane inlet assembly, purge valve, and ISMS. The membrane inlet assembly sits on top of the main chamber. A volume of air (gas headspace) is established in the interior of the membrane inlet assembly and the top portion of the main chamber while the bottom portion of the main chamber is filled with water. The sample will enter the BAC via a port at the bottom of the main chamber, rise to the top, and burst in the gas headspace. The resulting change in composition of the gas headspace is determined by the ISMS which will provide real-time results.

When methane (CH_4) comprises approximately 50 % of the gas headspace volume, it

should be collapsed (i.e. filled with water) and then re-established with air from the HPA and the purge valve from the BAC. To collapse the gas headspace, the purge valve is opened and the gas headspace will empty to the surrounding water. When the gas headspace is fully collapsed, the purge valve is shut. To refill the gas headspace, the high pressure solenoid is opened and high pressure air flows from the high pressure manifold, through the high pressure solenoid and flow control components into the BAC where it collects at the top of the main chamber. Details of the design and operation of the BAC and HPA are in Sections 2.4 and 2.5, respectively. Electronic control of these components is detailed in Section 2.6.

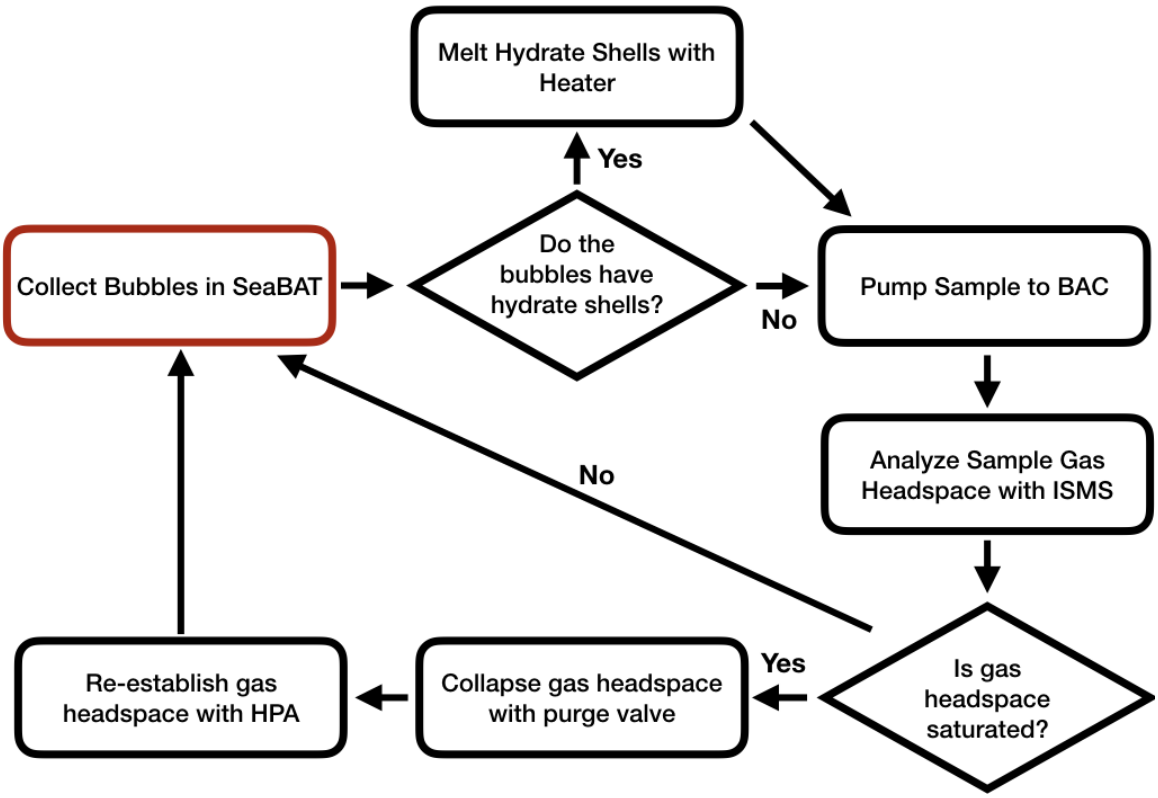

Figure 2-2: BDS sampling workflow. The red box indicates the beginning of the workflow.

2.2 General Design Considerations

Deploying the BDS in the deep ocean presents a unique set of design challenges. The materials used must be able to perform as desired in cold temperatures (0-4 °C), high pressures (>100 bar), and corrosive salt-water environments. Since this instrument is deployed by an

ROV, the components cannot be too heavy or large. Additionally, any component, such as the SeaBAT, used by the ROV manipulator arm is subject to unexpected mechanical shock and cable strain due to the dynamic nature of the arm movement. To this end, several general material selection and design considerations have been applied to the BDS design.

2.2.1 Oil Compensated Enclosures and Structural Materials

Electronic components such as valves and circuit boards cannot be exposed to sea water. Since the BDS is deployed *in situ* in the deep ocean, the only options to protect these components from exposure to sea water is to enclose them in a pressure vessel or to oil compensate them. Pressure vessels keep electronics completely dry and under atmospheric pressure. This is ideal for sensitive electronics that cannot withstand the intense pressures of the deep ocean (e.g., circuit cards and microcontrollers). Pressure vessels that can withstand the pressures outlined above are often made of stainless steel or titanium. Both of these materials are heavy and expensive to machine.

A lower cost option is to oil compensate the electronics. This method protects electronics by enclosing them in a housing that is filled with mineral oil. Mineral oil is effectively incompressible, so the differential pressure across the walls of the enclosure will be minimal. Thus, lighter components (often plastic) can be used for the enclosure walls. The drawback is that the electronics that are oil compensated are exposed to hydrostatic pressure. This limits the application to components that can withstand high pressure such as motors, valves, and junction boxes. While the BDS employs some electronics that cannot be oil compensated (see Section 2.6), there are several components that can withstand high pressures and thus were oil compensated:

1. SeaBAT Valve
2. BAC Purge Valve
3. HPA High Pressure Valve

The general design of an oil compensated housing is the same regardless of what is enclosed. The two features that are common to all oil compensated housings are the enclosure itself and a flexible bladder. For the BDS, several types of plastic commonly used for these type of enclosures were considered: Acetyl copolymer, Acetyl homopolymer, polyvinylchlo-

Table 2.1: Comparison of oil compensated enclosure material choices. Acetyl homopolymer was chosen because of its high strength, ease of machining, and lack of porosity.

Material	Temperature Range (°C)	Tensile Strength (kPa)	Ease of Machining	Cost
Acetyl Copolymer	-29 – 82	44,126	Easy	$$
Acetyl Homopolymer	**-29 – 82**	**62,052**	**Easy**	**$$$**
Polyvinylchloride (PVC)	-17 – 82	4,136	Moderate	$
High Density Polyethylene	10 – 82	27,579	Moderate	$$$
Nylon	-40 – 85	77,221	Difficult	$

ride (PVC), high density polyethylene (HDPE), and nylon. The important material characteristics are outlined in Table 2.1. All of the oil compensated enclosures were machined and built by the author in DunkWorks,[1] so the difficulty of machining was an important factor in the material choice. For that reason, Nylon was not used. Additionally, PVC becomes brittle at low temperatures and HDPE did not meet the minimum temperature requirement so neither was a good choice for this application. Although acetyl homopolymer has a higher tensile strength than acetyl copolymer, it is slightly more expensive. More importantly, the manufacturing process of large acetyl homopolymer stock often introduces low density air pockets that can affect the structural integrity of the component. For those reasons, acetyl copolymer was chosen for this application.

Although considered mostly incompressible, under large pressure increases, the volume of a fixed mass of oil decreases. The extent of the compression is given by [74]:

$$\frac{-\Delta V}{V_o} = \frac{\Delta P}{K_{oil}} \tag{2.1}$$

where ΔV is the change in volume, V_o is the starting volume, ΔP is the change in pressure, and K_{oil} is the bulk modulus of the oil. Given a maximum expected pressure change of 100 bar and K_{oil} is 2.41 GPa [74], the volume of the oil will only compress by 0.4 %.

The oil is allowed to compress by the use of flexible silicone bladders and all of the enclosures employed two such bladders. The first consisted of a 1.6 mm silicone sheet compressed by a 9.5 mm piece of acrylic plastic. The acrylic had a ⌀38 mm hole cut in the center to allow the bladder to experience the hydrostatic pressure, flex inward, and compress the oil. This single bladder was expected to accommodate the oil compression, but a fill line was

[1] DunkWorks is a rapid prototyping facility and is a part of the Center for Marine Robotics at Woods Hole Oceanographic Institution, Woods Hole, Massachusetts

needed to add and drain oil from the enclosure. The volume of this ⌀6.4 mm i.d. fill line was used as a backup bladder to accommodate at least 90% of the expected compression as a safety margin to avoid crushing the enclosure. This is an overly cautious inclusion because the internal volume of each of the enclosures was calculated as if there was no component in the enclosure. For example, the BAC Purge Valve enclosure internal volume was calculated without taking into account the volume that the valve itself would occupy.

The tubing also served as the oil fill line, so the caution came with little cost. At one end of the tubing, a quick-connect tubing connector was included so the enclosure could be filled from an external tank. A vent to allow the air displaced by the oil was located opposite of the oil fill line and is sealed with a gasketed screw when not in use. To fill the enclosure, the vent screw is removed and oil is added through the fill line. When oil begins to seep from the vent hole, the sealing screw is replaced and any excess air bubbles are evacuated using the fill line.

Details of the fill line internal volume and other features of the oil compensated enclosures are included in Sections 2.3, 2.4.3, and 2.5.2.

2.2.2 Metal Components

Salt water can cause corrosion that can bind fasteners and dissolve metal components. Galvanic corrosion can be a concern in strong electrolytic environments such as sea water, as well. To counteract these two effects, 316 Stainless Steel was chosen for all metal components (e.g., solenoid valve casings, high pressure tubing, fittings, fasteners, etc.) with few exceptions that will be discussed in the component descriptions.

2.2.3 Tubing and Electrical Connectors

With the exception of the HPA, the pressure inside all of the components and tubing is the same as hydrostatic pressure. Swagelok® 316 Stainless Steel tube fittings and adaptors (Swagelok Company, Solon, OH) were used throughout the instrument. In order for these fittings to create a good seal, the fluid tubing must be hard but must also be flexible because it will run along the ROV manipulator arm from the SeaBAT to the ROV body. The tubing must be transparent in order to observe bubbles moving through it. For these reasons, flexible nylon tubing was chosen for all fluid tubing. In all high pressure applications, 1/4 in. 316 stainless steel tubing rated to 4,300 psi was used.

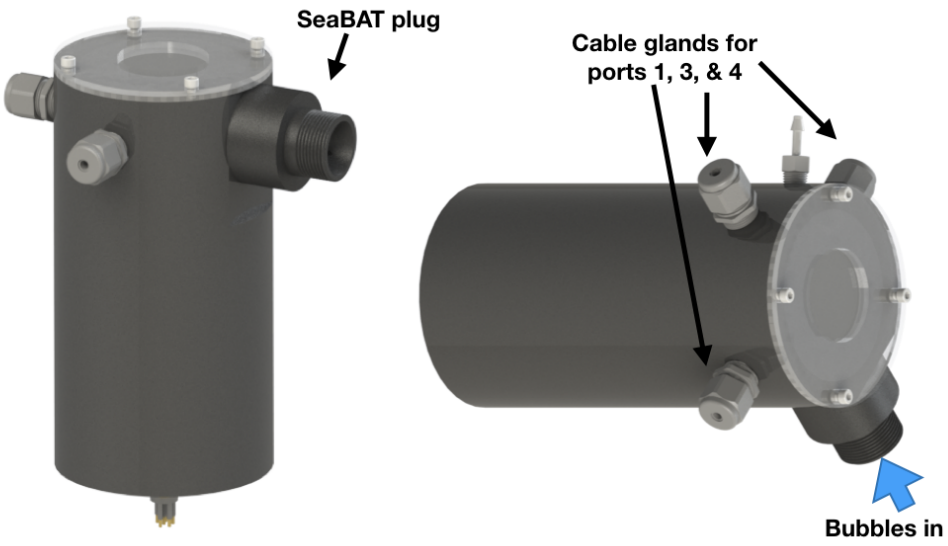

Figure 2-3: Rendering of the SeaBAT assembly.

All electrical connectors that are exposed to water are SubConn Micro Circular (MacCartney Inc., Esbjerg V, Denmark). Bulkhead connectors are male and all inline connectors are female. Molex inline connectors (SL 70066 Series) are use for all hook-ups inside pressure vessels and oil compensated enclosures.

2.3 SeaBAT Design

The SeaBAT consists of three major components: the (1) selector valve, (2) funnel plug, and (3) heater. The valve is oil compensated as described in Section 2.2.1 in a cylindrical enclosure with exterior dimensions of approximately $\varnothing 11.4\,\text{cm} \times 22.8\,\text{cm}$ and an interior volume of 962 mL (Figure 2-3). From Equation 2.1, the oil will compress by 3.8 mL. Thus, the oil fill line was 11 cm with an internal volume of 3.4 mL to accommodate 90 % of the oil compression. The SeaBAT was designed to meet the following requirements:

1. In order to reduce system complexity, a separate pump to move the bubble samples from the funnel into the valve is not used. Thus, the bubbles must be able to rise

passively into the valve.

2. The portions of the SeaBAT that come in contact with the sample must be chemically inert to prevent any chemical interaction with the gas.

3. Bubble streams are found at a variety of depths inside and outside of the GHSZ. The SeaBAT must be capable of sampling bubbles with and without hydrate shells.

4. The SeaBAT will be positioned above bubble streams by the ROV manipulator arm and its tubing/cable must be capable of extending the entire length of the arm.

2.3.1 Valve

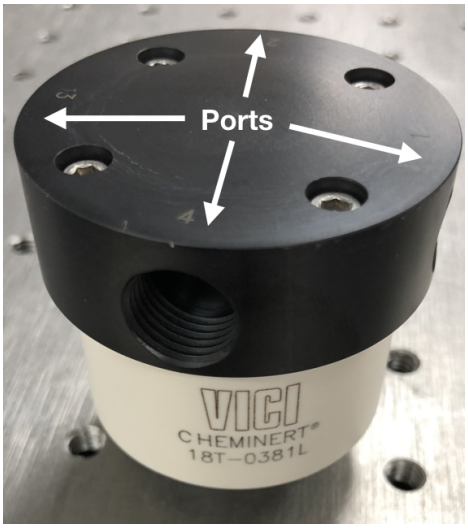

(a)

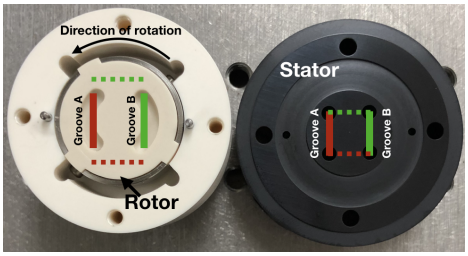

(b)

Figure 2-4: SeaBAT valve head images. a) Assembled valve head. Each port allows fluid/gas to enter or exit the valve head. b) Disassembled valve head. Streams that enter the assembled valve ports in the stator are connected via grooves cut in the rotor. To change the stream alignment, the stator rotates and the grooves will line up with the outlets of the ports in the stator. In this figure, the solid lines indicate the ports aligned by the grooves in position 1 while the dashed lines indicate the alignment in position 2.

The selector valve connects streams by rotating a grooved internal disc (the rotor) that directs flow between the four ports in a stationary cap (the stator) (see Figure 2-4). In position 1, streams 1 and 2 are connected by groove A while streams 3 and 4 are connected by groove B. Seawater flows in through port 4 and out through port 3 (Figure 2-5a). While in position 1, the sample rises into groove A (Figure 2-5b). Upon actuation, the grooved disc rotates counterclockwise (Figure 2-4b) to position 2. In position 2, streams 2 and 3 are connected by groove B while streams 1 and 4 are connected by groove A.

This rotation aligns the sample that was collected in groove A with the flow of seawater coming from port 4 and the bubbles are sent to the BAC. Check valves (1 psid cracking pressure) are positioned on the output of ports 1 and 3 to prevent the collected sample from back flowing into the opposite port while being pumped to the BAC. Meanwhile, the next sample begins to collect in groove B (Figure 2-5c). When the valve is cycled again, the rotor will rotate clockwise and return to position 1 where the bubbles collected in groove B will be sent to the BAC.

The rotor is made of a proprietary (Valco Instruments Company Incorporated, Houston, TX) polytetrafluoroethylene (PTFE) blend (Valcon E2). This material is slick and chemically inert to any of the gases that it might be used for in this application. The stator is made from Polyphenylene sulphide (PPS) which is also chemically inert [75]. A 4.2 mm inlet bore runs into both the rotor and the stator. Typical bubble sizes range from 2–5 mm [28,65] so this is large enough to allow most bubbles to enter the valve.

The valve is attached to a gear box and 24 V stepper motor. The stepper motor is actuated using a proprietary motor controller that is housed in a titanium enclosure on the ROV body along with the gear pump motor controller and the solenoid valve controls (discussed in detail in Section 2.6). Commands are sent to the motor controller using a terminal emulator and serial (RS-232) communication. Communication between the controller and the motor is over 6 m of underwater cable.

2.3.2 SeaBAT Plug

Nylon tubing is passed into the SeaBAT enclosure to ports 1, 3, and 4 using simple, watertight cable glands, but port 2 must interface with a funnel to collect bubbles (Figure 2-3). This requires a unique bulkhead penetration that will allow bubbles that have collected in the funnel to enter the valve head. Additionally, if the collected bubbles have a hydrate

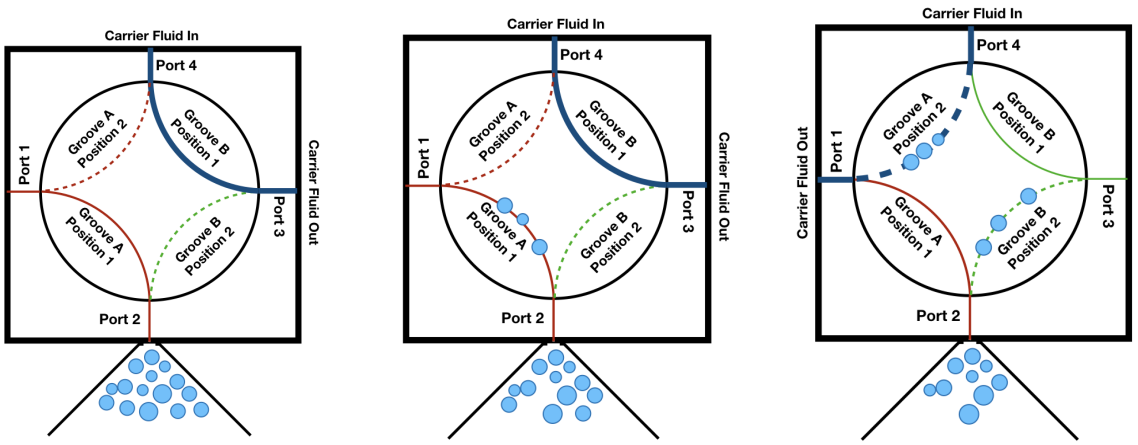

(a) Step 1 (b) Step 2 (c) Step 3

Figure 2-5: SeaBAT Sampling Steps. a) In step one, the SeaBAT is positioned over the bubble stream by the ROV manipulator arm and bubbles collect in the funnel. Fluid flow enters the selector valve via port 4. While the valve is in position 1, seawater exits the valve via port 3. b) Bubbles passively rise into the groove aligned with port 2. In position 1, the bubbles rise into groove A. c) When the valve is cycled, groove A connects port 4 and port 1. The bubbles that were collected in groove A are pushed to the BAC by the discharge of the gear pump. Meanwhile, the next sample collects in groove B while it is aligned with port 2.

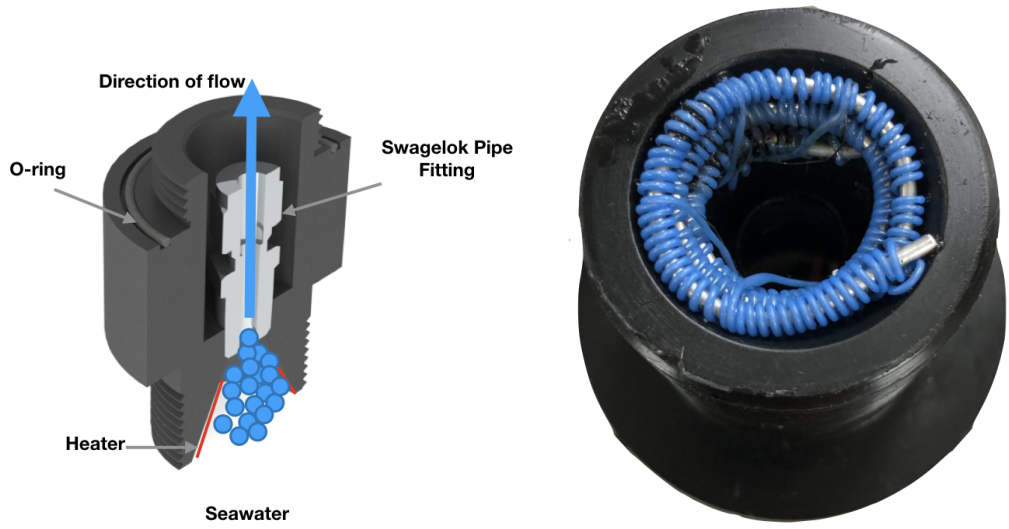

(a) (b)

Figure 2-6: SeaBat plug detail. a) Rendered cross section of the SeaBAT plug. Bubbles are represented as blue circles coming in from the bottom of the image. The red lines indicate where the heater is located and outline the heated volume of water. The O-ring and Swagelok tube fitting form the boundaries that separate sea water and the oil inside the enclosure. The shorter section of threading at the top of the image screws into the SeaBAT enclosure and the larger section at the bottom is where the funnel attaches to the plug. b) Image of a heater that has been integrated into a SeaBAT plug.

shell, the bulkhead penetration must include a heater to dissociate the gas hydrate before sampling. To meet these challenges, a plug was designed that screws into the enclosure and that also allows a funnel to be screwed onto the other end of it (Figure 2-6). The end of the plug which interfaces with the funnel is threaded on the outside (1 1/2 - 12 UNC). The inside of this end is also in the shape of a funnel so that bubbles collected in the funnel continue to collect at the opening that goes to the valve. The end of the plug which interfaces with the enclosure is threaded on the outside, as well (1 1/2 - 12 UNC). A Swagelok tube fitting is screwed into the bottom of this end of the plug and serves as a watertight connection to transfer the bubbles from the funnel to the inside of the valve. A watertight face seal is made against the face of the enclosure using a 2-031 Buna-N O-ring. A $\varnothing$2.8 mm hole is drilled next to the tube fitting to route heater wires through.

2.3.3 Hydrate Heater

Gas hydrate shells formed on CH_4 bubbles have a surface tension of up to 30 N/m [76]. Thus, it would be difficult for bubbles with a hydrate shell to passively rise into the valve as designed. In order to dissolve hydrate shells, the temperature must be raised or the pressure must be lowered until the ambient conditions around the bubble are outside the GHSZ. The simplest way to lower the pressure is to go up in the water column. This is not ideal because it is time consuming and will allow the bubbles to equilibrate with the surrounding water. Additionally, the ROV may have to travel well out of visual range of the sampling site and have a difficult time re-establishing the exact same sampling conditions. Raising the temperature of the seawater allows the ROV to remain on station, but faces the challenge of heating a nearly unlimited heat sink. However, if the volume of water is sufficiently small and insulated, a heater can be used to raise the temperature of the water to a point where the hydrate shells dissolve.

A heater is included in the funnel plug to heat a small volume of water immediately outside the opening of the tube fitting. The energy required to heat a volume of liquid (E_H) is given by:

$$E_H = m_l c_p \Delta T \tag{2.2}$$

where m_l is the mass of the liquid, c_p is the specific heat capacity of the liquid, and ΔT is the change in temperature required. The hollow mass on the funnel side of the plug is

7.24 cm^3 (neglecting the volume of the heater coil). Since the average density of seawater at 1000 m is 1.0375 g/cm^3, the mass of water in the hollow volume is 7.50 g. The average specific heat capacity of seawater is 4.0 J/g-K. The temperature below the thermocline in deep water is usually between 0-4 °C. Under isobaric conditions at 1000 m, the minimum temperature outside the GHSZ is 20°C. This gives a Δ T of 17 K. From Equation 2.2, 510.7 J is required to heat this mass of water by 17 K. The heated mass of water is enclosed by the acetyl copolymer funnel plug except for one small area. The large part of the funnel opening is the only surface area in which the heated mass of water is exposed to the surrounding water. The area of this cross section is 7 cm^2. Thus the heat loss to the surrounding environment was considered negligible.

The power (P) needed to heat this mass of water is given by:

$$P = \frac{E_H}{\Delta t} \tag{2.3}$$

where E_H is calculated from Equation 2.2, and Δt is the heat up time. A heat up time of 20 s was chosen to limit the amount of time bubbles are exposed to high heat to prevent any potential thermal degradation of the sample. From Equation 2.3, the power required to heat the small mass of water in 20 s is 25.5 W. The system is designed to work off of a 24 VDC power supply. Thus, from Ohm's law, a total resistance of 22.6 Ω is required for the heater.

It was difficult to find a commercially available heater that was small and malleable enough to fit in the funnel side of the plug and could withstand the high pressure and corrosive conditions of this application. Therefore, a custom heater coil was designed to meet these requirements. In order to accumulate 22.6 Ω in such a small space, the heater wire must be flexible, low gauge, have a high resistance per unit length, and have an insulation that is resistant to seawater but is thin enough to allow efficient heat transfer to the water. Alloy 294 (32 AWG, Pelican Wire, Naples, FL) was chosen to meet these needs. Alloy 294 is made from 55% copper and 45% Nickel, has a resistivity of 4.9 $\times 10^{-5}$ Ω-cm, and is coated in 228 μm Fluorinated ethylene propylene plastic. The 32 AWG wire used has a resistance of 0.15 Ω/cm. Thus 1.5 m of wire is required to make a 22.6 Ω heater coil.

The heater was made by tightly winding the Alloy 294 wire around 14 AWG 1100 Aluminum. By wrapping the flexible heater wire around a more malleable wire, the heater can

be made into any shape. In this case, the wound heater was shaped to fit inside the funnel shape of the SeaBAT plug (Figure 2-6b). The two ends of the heater wire were routed through the hole in the SeaBAT plug to the inside of the SeaBAT enclosure where they were connected to power and then the hole was sealed with epoxy.

2.4 Bubble Accumulation Chamber (BAC)

The BAC is the final stop for bubbles pumped from the SeaBAT before analysis by the ISMS. The BAC was designed to fulfill the following requirements:

1. The lower portion of the gas headspace where the bubbles collect must be clear so an operator can verify that the bubbles collected by the SeaBAT are entering the headspace.

2. The overall height of the BAC must be less than 61 cm in order to fit on the ROV.

3. There must be a mechanism to purge and re-establish the gas headspace.

4. The gas headspace must integrate with the ISMS for analysis.

The BAC consists of three subcomponents: (1) the membrane inlet assembly, (2) a collection chamber, and (3) a purge valve. To provide stability, the chamber and the membrane inlet sit between two acetyl copolymer plates with additional support provided by four $\varnothing 1.3\,\mathrm{cm}$ high-strength polycarbonate stand-offs. The membrane inlet is fastened to the top plate and is sealed with a 2-018 O-ring. The bottom of the membrane inlet has a groove that is slightly larger than the diameter of the chamber where a custom gasket sits to create a seal between the membrane inlet and the chamber. Similarly, the base plate has a gasket groove to create a seal between the chamber and bottom plate. The bottom plate has grooves cut in several different patterns to allow for mounting the BAC to the ROV.

2.4.1 Membrane Inlet Assembly

The membrane inlet is the interface between the ISMS and the gas headspace and consists of two pieces: the membrane support block and the gas block (Figure 2-8). The construction of the ISMS is described in [73], but its operation is analogous to that of any membrane inlet mass spectrometer (MIMS) technology. MIMS technology is used extensively in underwater

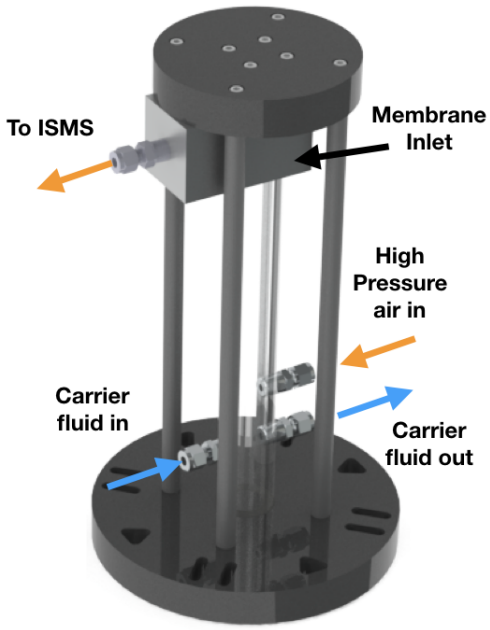

Figure 2-7: Rendered view of the BAC assembly. Fluid flow paths in and out are noted in blue while the high pressure air flow path is noted in orange. To purge the BAC, the gas headspace flows through the tube fitting at the top of the assembly to the purge valve. The hole pattern on the base plate is designed for multiple mounting options.

mass spectroscopy (UMS) because it allows the detection of dissolved gases or volatile organic compounds (VOC) with little or no sample processing. The membranes used are often hydrophobic and semi-permeable to gases based on the gas molecule size and chemical interaction with the membrane material. The instrument side of the membrane is at a vacuum greater than 10^{-5} Torr while the sample side pressure is limited by the structural integrity of the membrane. When water that contains dissolved gas or a slug of free gas passes the membrane, the pressure gradient between the partial pressure of the gas in the water and the vacuum in the mass spectrometer allows the dissolved gas to migrate across the membrane into the instrument where it is detected by the mass spectrometer. For this use, a Teflon AF membrane (Random Technologies, San Francisco, CA) was selected due to its excellent permeability to N_2, O_2, CH_4, and CO_2. A thorough review of current UMS technology is given by Chua *et al.* [77].

Since the BDS is operated in the deep ocean, the membrane must be mechanically supported to avoid rupturing under the high pressure. The membrane is supported by a $\varnothing$1.27 cm, 5 micron stainless steel frit (Applied Porous Technologies, Tariffville, CT) that is set into the 5.08 $\times$5.08 $\times$1.27 cm stainless steel membrane support block. O-rings keep high

pressure water from entering the ISMS from underneath the edges of the membrane. If the membrane or O-rings fail, the ISMS can be critically damaged. Since the consequences of a failed O-ring are so high, three separate O-rings are used and sealed against the face gas block. The two blocks are fastened by four, $^1/_4$-20 UNC screws.

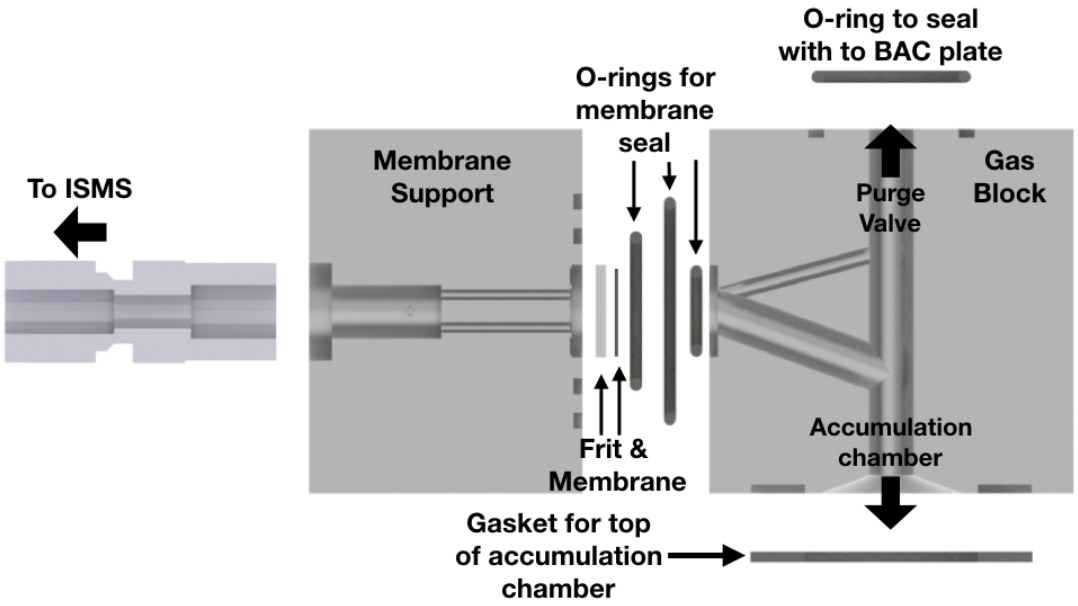

Figure 2-8: Exploded view of the membrane inlet. The Swagelok fitting on the left is connected to the ISMS. The largest membrane seal O-rings both seat in grooves in the left piece while the smaller O-ring seats in the cavity on the right piece. The frit seats in the cavity on the left piece and supports a thin membrane material.

The purpose of the gas block to connect the bubbles that have gathered at the top of the collection chamber to the membrane inlet and to allow a path to evacuate the gas headspace through the purge valve. The gas block has a $\varnothing$1.27 cm hole that runs the length of the piece and connects the chamber to the purge valve. The main channel is connected to the membrane by two smaller, angled channels. When the gas headspace is evacuated as described in Section 2.1, all of these channels will fill with water. When the headspace is re-established, the water must then drain from the channels. If the connecting channel met the main channel at a right angle, the water might not drain from the volume in front of the

membrane. To correct this, two connecting channels were drilled – one at an upward angle and the other at a downward angle. If only the downward channel were present, when filling the volume with water, the gas that was sitting in front of the membrane would have no escape path. Additionally, if the gas was somehow displaced and the volume was filled with water, capillary action and vacuum could keep the water in front of the membrane. The upward channel serves as an escape path during headspace collapse and a vacuum breaker when the headspace is re-established.

2.4.2 Collection Chamber

The chamber is made of a ⌀3.8 ×25 cm clear acrylic tube with a wall thickness of 0.6 cm. The bubble samples that are being delivered to the BAC have a volume of approximately 1 mL. In order to detect the change in gas headspace composition when a bubble sample enters, the volume of gas in the headspace must be as small as possible. The internal volume of the membrane inlet assembly is 6.5 mL. The volume that the gas headspace extends into the collection chamber must be kept as small as possible while still extending far enough that the bubbles can be seen rising into the gas headspace. A headspace length of 0.6 cm is adequate for observation and with an inner diameter of 2.5 cm the headspace volume is only 3.3 mL. The sample is 10 % of the initial gas headspace volume and its addition to the headspace devoid of any CH_4 should be clearly indicated by the ISMS output.

The thick walls of the collection chamber allow threads to be tapped for tubing penetrations and the acrylic is optically clear to allow for observation of the samples rising (Figure 2-7). There are three tubing penetrations in the bottom half of the acrylic tube. Two of the penetrations are used for carrier fluid/bubble flow in and out. The third penetration is above the fluid flow penetrations and is a high pressure air inlet. The high pressure air inlet is placed above the fluid inlet and outlet in order to eliminate the risk of high pressure air escaping through the fluid flow path.

2.4.3 Purge Valve

The purge valve is a 2-way, normally closed, 24 VDC solenoid valve (7000 Series, Parker-Hannfin, New Britain, CT) and is oil compensated as described in Section 2.2.1 with a silicone bladder. The enclosure dimensions are 15.4×7.6×7.6 cm with an internal volume of 681 mL. From equation 2.1, the oil will compress by 2.7 mL. Thus the internal volume of the

oil fill line was 8.7 cm to accommodate 90 % of the oil compression.

The solenoid valve is mounted to the bottom of the enclosure using 10-32 UNC sealing screws with 0.8 cm stand-offs. Stand-offs are necessary to align the inlet and outlet of the valve with the holes tapped for cable glands used as bulkhead penetrations for the tubing. The valve is opened by supplying voltage to the solenoid coil. The control circuitry (described in Section 2.6) can be damaged by the large currents caused by the "inductive kick" caused by the rapid collapse of the solenoids electric field when power is removed. Protection is provided by a 1 kV 1A "flyback" diode that allows the inductive current to dissipate in a loop back through the solenoid coil.

2.5 High Pressure Assembly

The HPA is in place to re-establish the gas headspace in the BAC after it has been evacuated using the purge valve. The assembly is mounted on the ROV body and is controlled remotely from the ROV command center shipboard. There are three subcomponents that make up the HPA: (1) high pressure manifold, (2) high pressure solenoid valve, and (3) flow control assembly. To re-establish the gas headspace in the BAC, the high pressure solenoid is actuated and high pressure air flows from the high pressure manifold, through the high pressure solenoid and flow control assembly into the BAC (see the orange section of Figure 2-1). The HPA was designed to meet the following design specifications:

1. The assembly must be able to re-establish a headspace up to 1000 meters below sea level (mbsl).

2. The flow of gas must be low enough that the creation of the headspace is easily controlled.

3. The assembly must be able to withstand the high differential pressure between the contained gas at the surface as well as the pressure change as the assembly is lowered to dive depth.

2.5.1 High Pressure Manifold

Two 0.5 L, stainless steel, 5000 psig cylinders (316L-50DF4-500, Swagelok Company, Solon, OH) were mounted on the ROV body and used for high pressure air storage when diving.

Both ends of each cylinder are open and tapped for 1/4 FNPT. The high pressure air manifold was created by plugging one end of both cylinders and connecting the other two ends using a "T" union.

2.5.2 High Pressure Solenoid

A high pressure, two-way, normally closed, 24 VDC solenoid valve (H22M9DCM, Peter Paul Electronics Company, New Britain, CT) is used to control the on/off flow of high pressure air to the BAC. This valve is rated to 3000 psi of gas pressure compared to the 600 psi rating of the purge valve in the BAC assembly. The valve mounting and enclosure are identical to the purge valve enclosure described in Section 2.4.3.

2.5.3 Flow Control Components

There is no indication of pressure in the high pressure manifold, so if the pressure in the tanks dipped below the hydrostatic pressure either by fill error on the surface or by over expending the air inventory at a shallow depth, a check valve (SS-4CA-50, Swagelok Company, Salon, OH) is included in the flow path downstream of the high pressure solenoid to prevent rapid back flow of seawater into the "dry" high pressure manifold. Upstream of the high pressure valve, a 40 micron filter was used to prevent the accumulation of particulates inside the valve body. The final component was a 63.5 µm sapphire orifice (Bird Precision, Inc., Waltham, MA) to limit the gas flow into the BAC to a rate at which the gas headspace can be reestablished with a 3 s opening of the high pressure valve.

2.6 Component Control

The control circuitry for the gear pump, SeaBAT valve and heater, and high pressure and purge solenoid were enclosed in a ⌀17.5 ×22.9 cm titanium pressure housing. Serial communications via RS-232 at 9600 baud and a terminal emulator were used to control each component. Power and communication to the BDS was provided by three independent, 24 VDC science channels on the ROV (Table 2.2). Both the SeaBAT valve and the gear pump have controllers provided by their manufacturers and are not detailed here. However, control of the SeaBAT heater, high pressure solenoid, and purge solenoid are provided by an Arduino Uno board (Rev3, Turin, Italy).

Table 2.2: The BDS requires three independent control channels to operate. Each channel receives commands from a separate controlling application.

Channel	Component(s) Controlled
A	– SeaBAT Valve
B	– SeaBAT Heater – High Pressure Solenoid – Purge Solenoid – Arduino
C	– Gear Pump

2.6.1 Arduino Wiring

The Arduino Uno accepts input voltages of 7–10 VDC and outputs 5 VDC (HIGH) and 0 VDC (LOW) on its 13 digital input/output (DIO) pins. The ROV electrical distribution system operates at 24 VDC, so the input voltage was converted to a lower compatible voltage. The Arduino output voltage was not sufficient to power 24 VDC components, so a DC relay shield (Seed Technology Co., Shenzhen, China) was used to toggle high voltage power to the components. The Arduino is capable of serial transistor-transistor logic (TTL) communications that operate at 0/+5 VDC, but is not designed to handle ± 15 VDC RS-232 standard. A RS-232 shifter (PRT-08780, SparkFun Electronics, Niwot, CO), was used to convert the RS-232 signal to an Arduino compatible TTL signal. Details of the DC conversion, high voltage circuitry, and communications are discussed below.

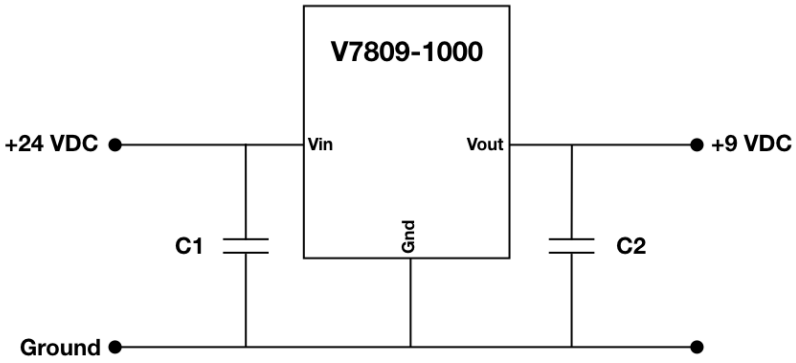

Figure 2-9: Voltage converter schematic.

Table 2.3: Arduino channel control scheme.

Arduino Pin	Relay	Component Controlled
7	1	Purge Valve
6	2	High Pressure Valve
5	3	SeaBAT Heater

DC-DC Converter

The 24 VDC input voltage was converted to 9 VDC using a non-isolated switching regulator (V7809-1000, CUI Inc., Tualtain, OR). The converter was built on a solderable breadboard and consisted of the regulator and two 10 μF capacitors (C1 & C2, Figure 2-9). The breadboard has two separate power busses – one on each side of the board. Input voltage is supplied to the bus on one side of the board and output voltage is supplied to the other bus while the grounds between the two buses are connected. There are three pins on the voltage converter – Pin 1 is connected to the input voltage, Pin 2 is connected to ground, and pin 3 is connected to the output voltage. Capacitors C1 and C2 add bulk capacitance to the power supply, which stabilize it during rapid changes in power demand. When 24 VDC is supplied to Pin 1, it is converted to 9 VDC and output to the low voltage bus.

High Voltage Circuitry

Power for the three components that are controlled by the Arduino is supplied from the same 24 VDC bus that is used for the DC-DC converter. The positive terminals are directly connected to the component while the relay is used as a low side switch to make or break the connection to ground for each component. The relays on the shield are controlled by DIO pins 5-7 (Table 2.3).

Since mechanical relays are used in this application, when current runs through the relay inductor, the switch position physically changes (Figure 2-10). The relay inductors are powered by Arduino 5 VDC control power. Current flow through the inductor is regulated by a transistor that is controlled by the Arduino DIO signal. When the DIO signal is HIGH, the controlling transistor allows current flow through the relay. Alternately, when the DIO signal is LOW, no current flows through the transistor. Form C relays are used in the relay shield, thus the relay can operate as normally closed (NC) or normally open (NO) depending on the wiring configuration. Each high voltage junction has three terminals: NO,

NC, and COM. Under non-gated conditions when the relay is not energized, the NC and COM terminals are connected. When the controlling transistor is gated and the relay is energized, the NO and COM terminals are connected.

The ground wires from the components controlled by this circuit are connected to the COM terminals of their respective relay. Ground from the high voltage bus is connected to the NO terminals of the active relay junctions and have 1.25 A fuses to protect against overcurrent conditions. When the DIO output is HIGH, the NC and COM terminals are connected and there is no power to the controlled component. Alternately, when the DIO output is LOW, the NO and COM terminals are connected and power is supplied to the controlled component. With this configuration, the relays will open on a loss of power or mechanical failure placing the system in a safe condition that will not overload the ROV power supply. Additionally, the relays are open and their loads are de-energized without expending any power energizing the relays. Since the components are de-energized most of the time, this reduces the constant load on the ROV power supply by 3.75 W and minimizes the heat generation of the relays.

2.6.2 Control Algorithm

Serial control commands are sent from a shipboard computer operated from the ROV control room. The serial signal is sent to a ship-board multiplexer where the signal is encoded in a data packet that is sent to the ROV via a fiber optic tether. When the signal is received on the ROV, it is then converted back to the traditional RS-232 signal and sent to the appropriate science channel. The commands are then received by the RS-232 switcher described in Section 2.6.1 where it is converted to a TTL signal.

The Arduino receives serial commands and places them in a queue known as the serial buffer. Once a command in the buffer is read, it is discarded. The commands used to control the components in Table 2.3 are byte sized (e.g., '1', '2', '3', etc.) to simplify the serial communication and minimize the chance of errors in the encoding process between the ship and ROV.

There are two functions required for that Arduino to function: `setup()` and `loop()` and are called automatically by the Arduino. The `setup()` function is called once when the Arduino boots up and it establishes the initial conditions of operation. In this instance, the `setup()` function prepares the Arduino for serial communication at 9600 baud and identifies

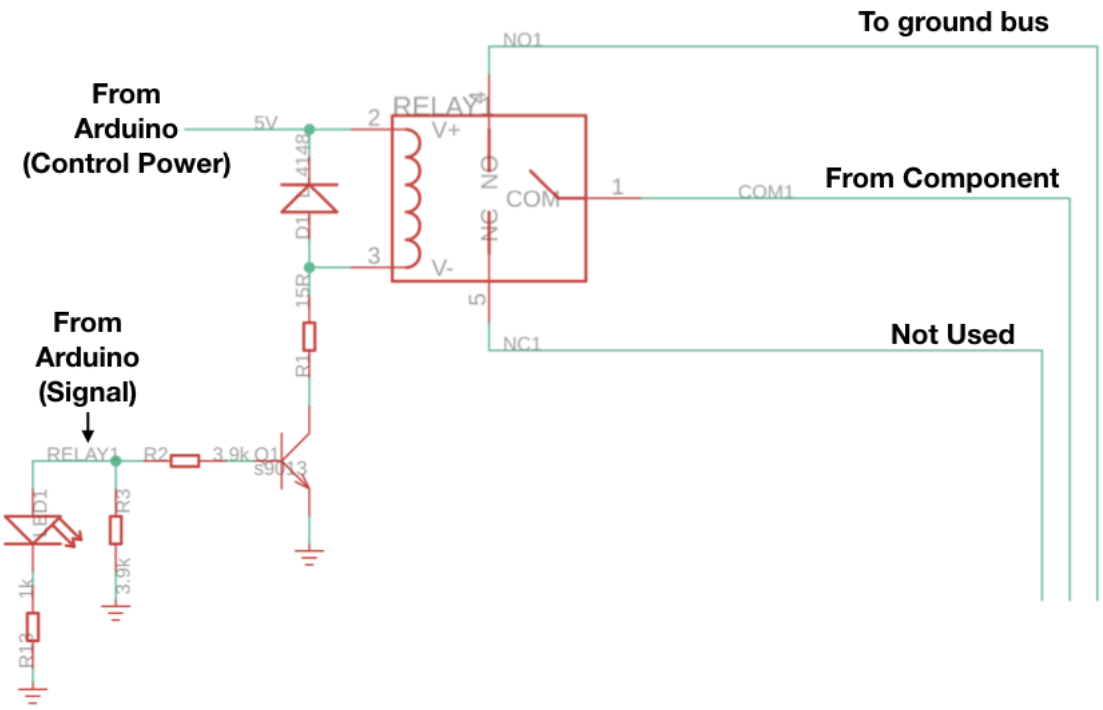

Figure 2-10: Example schematic of a relay circuit. When a HIGH signal is given, the transistor O1 is gated and 5 VDC control power from the Arduino is allowed to flow through the relay inductor to ground. This connects COM1 to NO1 and completes the high voltage circuit for the component that is being controlled.

DIO pins 5-7 as output pins and sets them to LOW so all of the connected components begin deenergized. The `loop()` is called once, but performs the functions and commands inside forever. The control algorithm is placed inside of the `loop()` function to be repeated.

The core function of the control algorithm is to cycle power to the components in Section 2.3. The algorithm includes some timers and interlocks to aid the operator and protect the equipment. There are three functions called in the control algorithm:

1. `millis()` – a native Arduino function that returns the time in milliseconds since the Arduino first booted up.

2. `handleSerial()` – takes serial input to the Arduino and controls the state of the DIO pins.

3. `waitTime()` – runs a timer in the background to limit how long the components are actuated.

First, the algorithm calls the `millis()` function and stores the returned time in a `ticker`

Algorithm 1 Main Loop

```
loop
  ticker ← millis()
  handleSerial()
  waitTime()
end loop
```

variable (Algorithm 1). Next, `handleSerial()` checks to see if there are data in the serial buffer. If there is, it reads the data and performs any action required by the command. Finally, if `handleSerial()` starts a timer to automatically deenergize one of the components, `waitTime()` keeps track of that timer and will secure the component when the timer expires. When the loop begins again, `ticker` updates with a new elapsed time and the process begins again.

When there are data in the serial buffer, the `handleSerial()` reads the byte of data and changes the state of a DIO pin (Algorithm 2, Appendix A). The function employs a while loop, so if there are multiple commands in the buffer, the main loop will stay in this function until all of the commands are cleared from the queue. In addition to translating serial commands, `handleSerial()` employs an interlock between the high pressure solenoid and purge solenoid which prevents both valves from being opened at the same time and rapidly depleting the high pressure air supply without re-establishing the headspace. The interlock also protects the BAC from mechanical failure from the internal stress of excessive high pressure air. Lastly, it initializes the variables that mark the time the signal was received to pass into `waitTime()` in order to limit the amount of time the components are energized.

The commands interpreted by `handleSerial()` are single digit cases ranging from 1-7 (Table 2.4). Case 1 and 2 open the high pressure solenoid for a set amount of time. In case 1, the high pressure solenoid is only opened for 50 ms in order to establish a gas headspace at shallow depths and to fine tune the volume of air in the headspace at deeper depths. Case 2 limits the duration of high pressure solenoid actuation to 3 s. These time limits are necessary to prevent overfilling the BAC when re-establishing a gas headspace. This actuation time is designed to establish a gas headspace of approximately 0.6 cm at 1000 m. While excess gas in the BAC would likely flow out of the fluid outlet, there is a possibility it could unseat or damage the upper or lower seals or cause other, more serious damage to the assembly.

These commands initialize the variables `hpLong` and `hpShort` and assigns them the time,

in milliseconds, that have elapsed since the Arduino has booted. These variables are used in the `waitTime()` function (Algorithm 3, Appendix A) to limit the actuation time of the valve. Additionally, in these two cases, the algorithm detects the status of the DIO pin that controls the purge valve. If the output voltage of the DIO pin 7 is HIGH, then the high pressure valve will not open.

Cases 3 and 4 open and shut the purge valve. Similar to Cases 1 and 2, if pin 6 is HIGH, then the purge valve will not open. A separate command to shut the purge valve is included because there are no significant consequences of leaving the purge valve open indefinitely and the time it needs to be opened to completely clear the gas headspace can be variable so there is no need for a timer.

Cases 5 and 6 control the hydrate heater. Case 5 energizes the hydrate heater for 30 s and provides a warning/reminder that the heater is still energized after 15 s. Similar to Cases 1 and 2 the timer variable `heater` is used here to mark the command time. This timer is in place because excessive heating could lead to thermal degradation of the sample or melting of the heater wire insulation, and it would be easy to leave the heater energized inadvertently because there is no visual feedback to indicate that it is in operation. The 30 s timer encompasses the 20 s designed heat-up time plus a 10 s buffer to allow for the complete dissolution of the hydrate shells if present. Case 6 deenergizes the heater to allow for greater control of the heating process.

Case 7 deenergizes all of the equipment. This command is reserved to ensure that all of the equipment can be placed in a safe condition quickly without having to issue several commands. For instance, if the purge valve was open and the heater was on, they can both be secured by issuing command '7' rather than '4' and '6'.

The Arduino language has a `delay()` function that stops the main loop for a set amount

Table 2.4: List of Arduino commands.

Command	Action	Interlocks
1	Open high pressure solenoid for 3 s	High pressure - Purge Valve
2	Open High pressure solenoid for 50 ms	High pressure - Purge Valve
3	Open Purge Valve	High pressure - Purge Valve
4	Shut Purge Valve	None
5	Energize SeaBAT heater for 30 s	None
6	Deenergize SeaBAT heater	None
7	Deenergize all equipment	None

of time, but when this function is called, the Arduino cannot accept any other commands. Thus, if the heater timer was active, the operator would not be able to open or shut either of the solenoids or turn off the heater without removing power from the Arduino because `handleSerial()` will not read the next command in the buffer until the timer is finished. The `waitTime()` function (Algorithm 3, Appendix A) runs a timer for the high pressure solenoid and heater independently in the background of the main loop. When the timer variable is initialized in `handleSerial()`, it stores the time that the command was executed. All of the time containing variables in this code are `unsigned long` — 32 bit integers greater than zero. This data type was chosen rather than something with more precision, like `float`, because `millis()` will overflow back to zero after 4.32×10^9 ms. The `unsigned long` data type can accommodate such large number. Additionally, the `float` data type is not native to the Arduino language and is not efficiently compiled. Overall, the use of `waitTime()` rather than `delay()` allows the operator to multitask while sampling bubbles and it provides an opportunity to protect the system by calling case 7 to de-energize all of the equipment.

2.7 Summary

The BDS is composed of three components: (1) the SeaBAT, (2) the BAC, and (3) the HPA. The SeaBAT is manipulated by an ROV to collect bubbles that are then pumped to the BAC where the chemical composition can be analyzed by an ISMS which gives real-time results. After a set volume of bubbles have been collected (see Section 2.4), the gas space of the BAC is evacuated and then refilled using the HPA. The BDS is the first bubble sampling system of its kind and allows for dynamic, *in situ* bubble collection in which the operator can adapt a collection plan based on the current chemical results. Unlike other *ex situ* sampling systems, the BDS also allows for multiple samples per dive without the need for bulky gas-tight sampling containers to transfer gas at pressure. In the following chapters, the first BDS deployment conditions and results are discussed.

THIS PAGE INTENTIONALLY LEFT BLANK

Chapter 3

BDS Deployment

In 2018, the BDS was deployed aboard the Schmidt Ocean Institute R/V *Falkor* (Cruise ID FK180824) using the ROV SuBastian on the Cascadia Margin in the northeast Pacific Ocean (Figure 3-1).

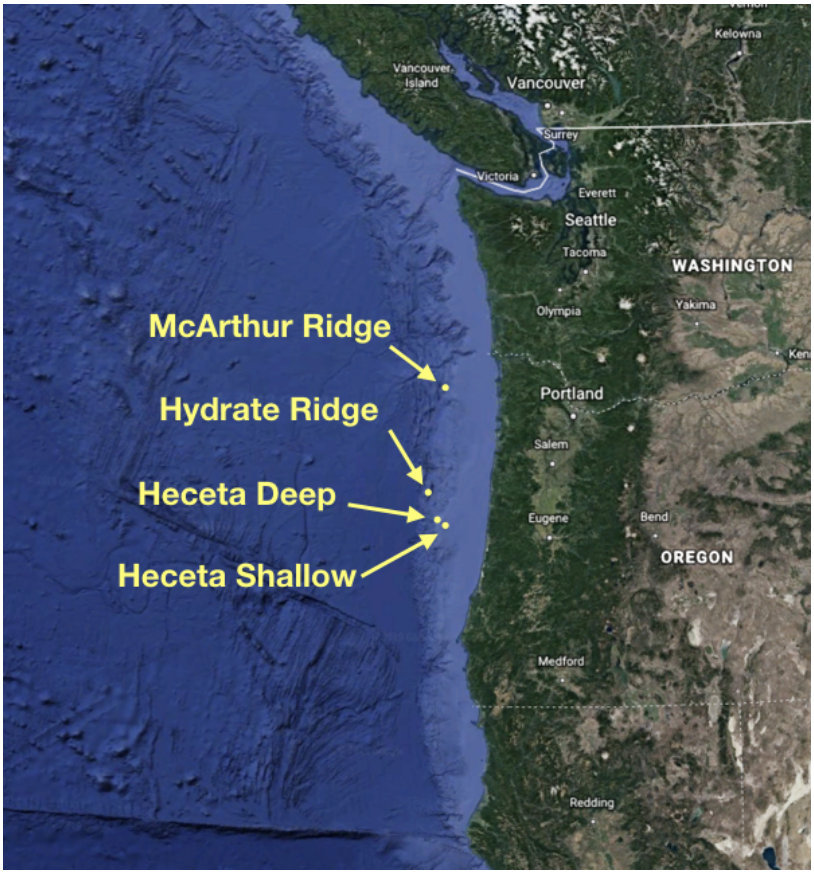

Figure 3-1: Image of all dive locations visited in this study. Locations are marked and labeled in yellow. Map background from Google Earth.

3.1 Geologic Setting

The Cascadia Margin is an extensively studied region where the Juan de Fuca plate (JdF) is actively being subducted below the North America plate to its east. The Cascadia Margin Subduction Zone (CMSZ) is well known for its extensive network of over 1100 known active methane seeps (Figure 3-2). It is estimated that approximately 88 $\times 10^{-6}$ $^{kg}/_{y}$ ebullitive CH_4 enters the water column in the CMSZ alone [28].

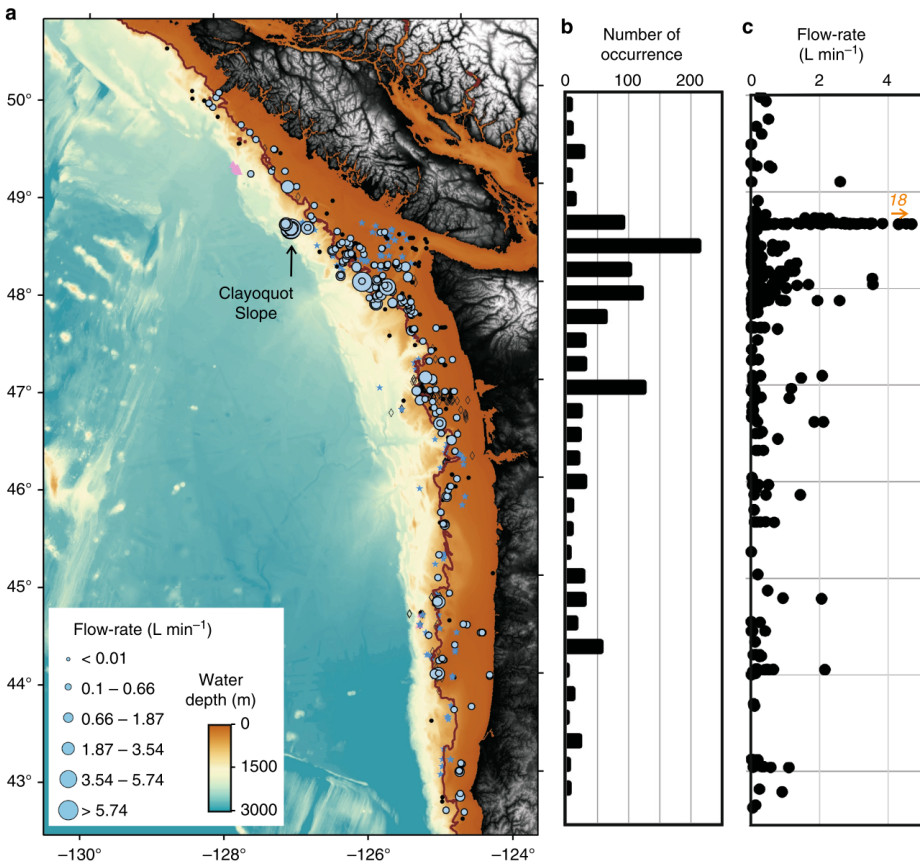

Figure 3-2: Distribution of ebuillitive methane seeps along the CMSZ. a) Distribution of observed methane seep sites visualized by gas flux. The larger the blue circle, the greater the gas flux. The red line indicates the approximate location of the 500 m isobath – the location of the TGHZ in the region. b) Histogram indicating the number of seep occurrences by longitude. c) Distribution of gas flux by longitude. Figure adapted from [28].

Modern Subduction Zone

The JdF has fractured into three smaller microplates that comprise the current configuration of the CMSZ: the Explorer plate, the JdF, and the Gorda plate. [78]. The JdF is situated

between the Explorer plate to the north and the Gorda plate to the south. The modern CMSZ runs from Vancouver Island in Canada to Cape Mendocino, California – a distance of approximately 1000 km. In this region, the JdF plate complex is pivoting around the Mendocino Triple Junction subducting below the North America plate at a rate of 20 $^{mm}/_{yr}$ in the south and over 40 $^{mm}/_{year}$ in the north [79, 80]. The region – especially the Gorda plate – is still quite seismically active, but the last major earthquake on the CMSZ occurred in 1700 [81].

Subduction zones such as the CMSZ are often characterized by deep trenches where the subduction begins and by accretionary wedges formed by accumulated material scraped from the surface of the subducted plate. There is not a notable trench along the CMSZ, however there is an immense accretionary wedge due to high carbon input from increased primary production along the west coast of the United States. This thick, permeable accretionary prism is critical in the development of these methane hydrate complexes described in Section 1.1.

3.2 Instrument Suite

The BDS was integrated onto the ROV SuBastian along with an *in situ* laser spectrometer [82] and ISMS (Figure 3-3). The plumbing configuration allowed gas samples to be taken and analyzed by the ISMS and/or the laser spectrometer. The ISMS could monitor either the BAC gas headspace or the carrier fluid being pumped through the sampling lines. Bubble sites were identified using a ship-mounted EM 710 multibeam sonar (Kongsberg Maritime, Kongsberg, Norway).

3.2.1 BDS Modifications

This cruise was the first deployment of the BDS in the field and thus there were several modifications to its operation to allow for successful collection of bubble samples. Four issues during the cruise led to significant changes in the pumping/sampling regime presented in Section 2.1:

1. Failed check valves upstream of the SeaBAT

2. ROV system ground faults caused by the SeaBAT hydrate heater

3. Difficulties refilling the BAC gas headspace with the HPA

4. Inability to send bubbles from the SeaBAT to the BAC

First, there were difficulties transferring bubbles from the SeaBAT using the plumbing shown in Figure 2-1. While troubleshooting, there was reverse flow through the SeaBAT that should have been prevented by the downstream check valves when the gear pump was run in reverse. Upon inspection, the check valves were found to be clogged by particulate matter and had failed in the open. It was determined that the 1 psid crack pressure on the valves was too low and the clogging would reoccur too frequently for the original plumbing to be successful so the check valves were removed. The plumbing was changed to that shown in Figure 3-4. As a result, the SeaBAT port connections described in Section 2.3.1 were modified to account for the lack of back flow protection that was provided by the check valves. Port 2 was still connected to the funnel, ports 1 and 4 were left open to the surrounding seawater and port 3 was connected to the gear pump suction.

There were also issues with the SeaBAT heater. When energizing the heater, the ROV experienced multiple ground fault indications in its control system. The ground fault detection system of the ROV senses small changes in the electric field in the water and when the heater was energized, the change in the field indicated there was a circuit shorted to ground in the system. After troubleshooting to confirm the heater was the cause of the ground fault warning, power to the heater was disconnected at the 24 VDC distribution board.

It is unclear why the heater might have caused a ground fault warning. None of the other components powered by the distribution board caused a fault when energized so it is unlikely the cause lay in the control and power distribution circuit. If the operator cleared the fault while the heater was energized the fault would immediately return, so the rapid change in current (and subsequent change of electric field in the water) on heater energization did not cause the fault. Since overcurrent protection was included in the power distribution board, if there was a break in the heater insulation, a fuse would have blown and the fault conditions would have cleared. After exploring these options, the only likely explanation for the fault is that the heater insulation was so thin, it allowed a strong enough electric field to be generated in the water that it caused a ground fault on the ROV. Regardless of the cause, the heater was not used for the duration of the cruise and the sampling technique was modified to include mechanical agitation to break the hydrate shells (described in detail in

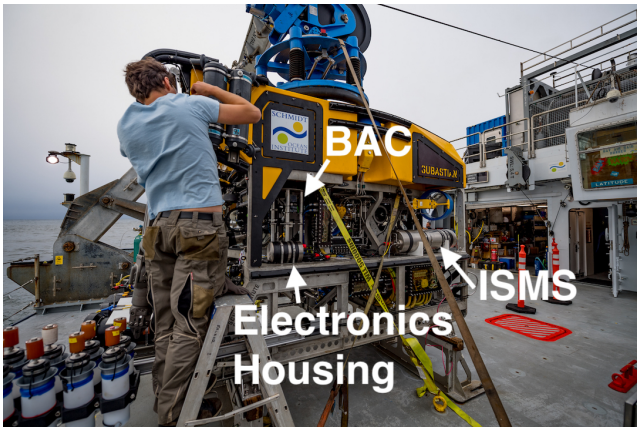

(a) Port View

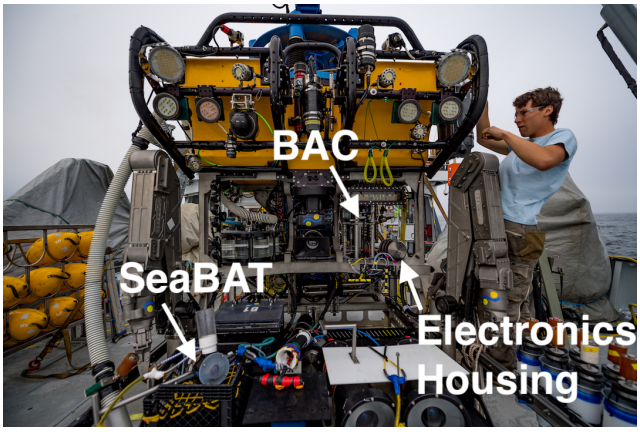

(b) Front View

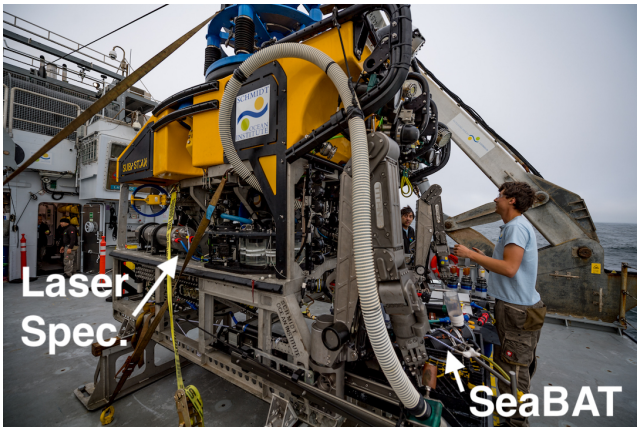

(c) Starboard View

Figure 3-3: Instrument suite mounted on ROV SuBastian. a) Port view of the ROV where the BAC, component control enclosure, and ISMS were mounted. b) Front view of the ROV where the SeaBAT is kept in its cradle on the porch. The component control enclosure and BAC can be seen from this view. c) Starboard view of the ROV where the laser spectrometer is mounted. The SeaBAT can be seen on the ROV porch from this view, as well.

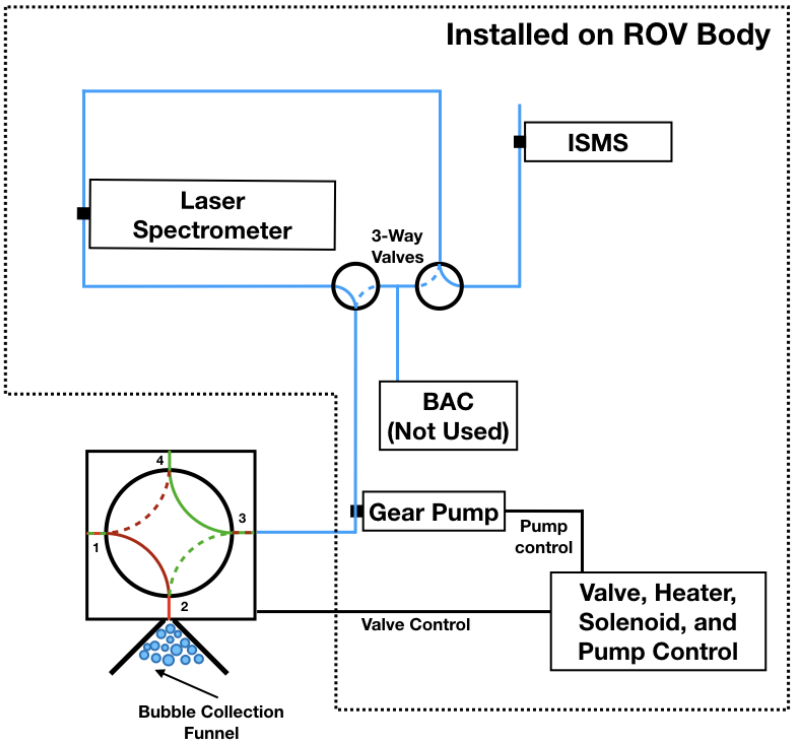

Figure 3-4: BDS cruise configuration. In the cruise configuration, the SeaBAT was used to send bubbles to an *in situ* laser spectrometer and ISMS for chemical analysis. Two three-way valves were used to route bubbles to the laser spectrometer, ISMS or both. The three-way valves were configured such that bubbles could be sent to the BAC, but due to the difficulties described in Section 3.2.1, the BAC was never plumbed to the membrane inlet of the ISMS. The component control was still connected as described in Section 2.6.1, but the heater power was disconnected at the power distribution board.

Section 3.2.2).

Finally, the difficulties with the BAC and HPA resulted in the BAC not being used during any of the sample collections. First, the flow control orifice in the HPA was too constrictive to allow high pressure air flow from the manifold to the BAC while operating at depth. With the flow control orifice removed, 50 μsec air bursts allowed the gas headspace to be refilled in a controlled manner. Once this modification was made, the three way valves were aligned to allow bubble samples to flow into the BAC, but this was not successful. The cause of this failure is unknown, but could have been due to plumbing errors or accumulation of gas hydrate in the sample lines that would not allow gas flow to the BAC. Regardless, the orifice modification did not occur until the end of the cruise and there was not enough time to continue troubleshooting the problem. The result of this modification is that the ISMS membrane inlet monitored the sample line directly and experienced slugs of gas rather than

continuously monitoring the gas headspace.

3.2.2 BDS Sampling

With the changes in the BDS configuration described in Section 3.2.1 came changes in the sampling regime that was described in Section 2.1. The first step of the sampling procedure still begins with bubbles collected in a funnel on the SeaBAT, but with power disconnected from the heater, if there were methane hydrate shells on the bubbles, they could not be melted. Instead, hydrate shells were broken by mechanical agitation of the SeaBAT and formed a single gas volume at the inlet to the SeaBAT. With the check valves removed and the pump moved downstream of the SeaBAT, the bubbles were actively collected using the pump suction rather than being pushed by the pumps discharge after passively rising into the valve head. In position 1, the gear pump is pulling seawater from the SeaBAT through ports 1 & 4 and groove B. Cycling the SeaBAT to position 2 aligns the pump's suction to the funnel and sampling is stopped by cycling the valve back to position 1. Modulating the time between cycles allows for control of the bubble sample size. Each collection of bubbles in the funnel was sampled 3-5 times before the bubbles were released and a new collection began.

Since the BAC was not used, the bubbles were pumped directly to the *in situ* instrument suite for analysis. By manipulating the two three-way valves in Figure 3-4, bubbles could be pumped to the *in situ* laser spectrometer, the ISMS, or both. In this configuration, the bubbles pass by the membrane inlets as a slug of gas rather than accumulating in the gas headspace of the BAC. Instead of discrete step-wise increases in signals over time, this sampling approach resulted in quasi-Gaussian sample peaks during time monitoring with the RGA software.

The ISMS was configured to monitor nine discrete ion masses (28 (N_2), 32 (O_2) 44 (CO_2), 15 (CH_4), 40 (argon), 34 (H_2S), 18 (water-18), 17 (water-17), and 2 (H_2) amu) on channels 1-9. Channels 1-3 correspond to the most abundant isotopologue of N_2, O_2, and CO_2. The most dominant isotopologue of CH_4 is 16 amu, but this signal is coincident with an oxygen-16 fragment from water vapor, which is very abundant in all underwater mass spectra [83]. Channel 4, with a mass of 15 amu, was used as a proxy for CH_4 despite not being the dominant species. Channels 5-9 correspond to argon, hydrogen sulfide (H_2S), water-16 ($H_2{}^{16}O$), water-17 ($H^{17}O$), and hydrogen (H_2). Channels 1-4 were monitored for

Table 3.1: Dive locations and depths.

Location	Depth (m)	Latitude (°)	Longitude (°)
McArthur Ridge	832	45.8484	-124.8955
Hydrate Ridge	787	44.5704	-125.1484
Heceta Deep	489	44.2507	-124.9783
Heceta Shallow	115	44.2034	-124.8514

the gas species of interest while channels 5-9 were monitored primary for troubleshooting and normalization.

3.3 Site Descriptions

Over the course of two weeks in August/September 2018, the modified BDS was deployed on seven dives at McArthur Ridge, Hydrate Ridge, and Heceta Bank (Table 3.1).

3.3.1 McArthur Ridge

The BDS was deployed three times at McArthur Ridge at seeps named Eldin's Bubbles 1, 2, & 3 within 150 m of one another at a depth of approximately 830 m. This was the first time McArthur Ridge was explored by an ROV. McArthur Ridge is on a bathymetric plateau at the edge of the shelf break approximately 25 km south of Astoria Canyon. Jagged authigenic carbonate formations surrounded by fine sediment mixed with small rocks and broken shell debris were characteristic of all three sites (Figure 3-5a) where each of the seeps emanated from the edges of the carbonate formations. We observed filamentous white bacteria at Eldin's Bubbles 1, 2 & 3 and yellow bacterial mats at Eldin's Bubbles 1 & 2 (Figures 3-5b & 3-5c).

3.3.2 Hydrate Ridge

The BDS was deployed twice at Hydrate Ridge at the Hester bubble flares. Both Hester 1 & 2 were within 200 m of each other at a depth of approximately 790 m. Hydrate Ridge is a bathymetric high that runs roughly north-south with a length of 25 km and width of 0.6 km that protrudes approximately 600 m from the surrounding seafloor. Both sites were covered in fine sediment and Hester 1 was littered with shell hash which was absent from Hester 2. We observed a 10 $\times$ 15 m pockmark roughly 25 m from the Hester 1 flare site

(Figure 3-5d). Bubbles from Hester 1 & 2 emanated from multiple holes in the seafloor that resembled small, round tunnels (Figure 3-5e). Hester 1 was covered with widespread white bacterial matting while none was observed at Hester 2.

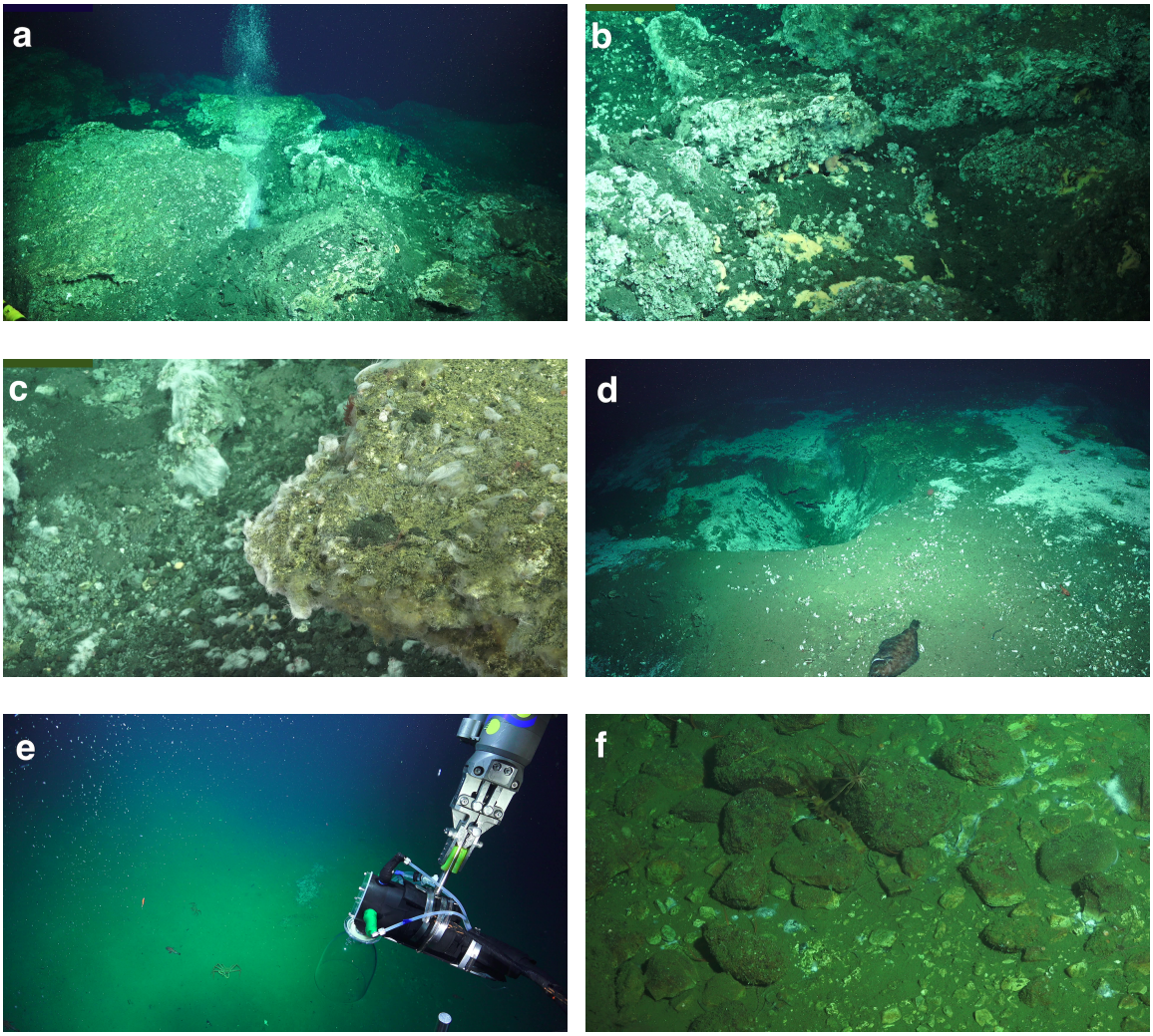

Figure 3-5: Dive site images. a) Vigorous flare at Eldin's Bubbles 2 (McArthur Ridge) emitting from the base of an authigenic carbonate formation. b) Yellow and white bacterial matting at Eldin's Bubbles 2. c) White filamentous bacterial on a carbonate outcrop above the bubble origin at Eldin's Bubbles 1 (McArthur Ridge). d) Large pockmark and white bacterial matting near Hester 1 (Hydrate Ridge). e) SeaBAT being maneuvered to collect bubbles being emitted from multiple locations at Hester 2 (Hydrate Ridge). f) Basalt rocks that litter the seafloor at Heceta Shallow.

3.3.3 Heceta Bank

Heceta Bank is a bathymetric feature approximately 40 km northwest of Florence, Oregon in which the continental shelf extends further seaward than the surrounding area. The extension is approximately 45 km in length and protrudes roughly 14 km greater than the surrounding area. The BDS was deployed twice to this area – once in a 115 m “shallow" region and once in a 480 m “deep" site. Heceta Deep is approximately 12 km northeast of Heceta Shallow and is a separate bathymetric high that occurs past the shelf break and is separated from Heceta bank by a 700 m submarine canyon.

The seafloor at Heceta Deep seep is covered in fine sediment while Heceta Shallow is littered with weathered basalt rocks with diameters between 0.1 m to 0.3 m (Figure 3-5f). Both Heceta Bank seeps had a single origin that resembled a small circular crater with a diameter of approximately 100 mm. No microbial mats were observed at Heceta Deep, but limited white microbial mats were noted around the perimeter of the rocks at Heceta Shallow.

3.4 Summary

The BDS was successfully deployed and collected bubble samples over the course of seven ROV dives at three locations. There were several modifications to the BDS subsystems that changed the flow pattern and resulted in only the SeaBAT being used for collection. As a result of these modifications, the sampling procedure was slightly altered allowing only one SeaBAT valve groove to be used for gas collection. Additionally, the collected samples were pumped directly to a membrane inlet assembly rather than the BAC resulting in different sample peaks than expected. In the following chapter, the data collected during this deployment are analyzed and the results are discussed.

Chapter 4

Results & Discussion

Over the course of seven dives, 95 bubble samples were collected at McArthur Ridge, Hydrate Ridge, Heceta Deep and Heceta Shallow at altitudes between 0.5-26 meters above the seafloor (masf). Ebullition rates from each of the seven dives were visually determined and are presented in Section 4.1. The collected data were parsed, analyzed, and truncated as described in Section 4.2. Finally, in Section 4.3, the chemical composition results are described and discussed.

4.1 Ebullition Rate

Ebullition rates were estimated visually from ROV video by counting bubbles for 15 s and extrapolating to rates in $^{\text{bubbles}}/_{\text{min}}$. Visual counts were only performed once because adequate dive footage was not available to perform multiple estimates. The rate at Eldin's Bubbles 2 & 3 were too great to count visually so no estimate for those sites is given. The lowest rate at McArthur Ridge was Eldin's Bubbles 1 at 150 $^{\text{bubbles}}/_{\text{min}}$. This seep was the only one observed with periodic bursts of several bubbles followed by 3-5 s of inactivity. At Hydrate Ridge, both sites visited had multiple bubble sources within 1 m of each other. Hester 1 had six individual bubble seeps with rates of 400 $^{\text{bubbles}}/_{\text{min}}$ each with an overall rate of 2,400 $^{\text{bubbles}}/_{\text{min}}$. Hester 2 was slightly less vigorous with individual seep rates of 300 $^{\text{bubbles}}/_{\text{min}}$ in each of its 4 flares for a total rate of 1,200 $^{\text{bubbles}}/_{\text{min}}$. At Heceta Deep, the ebullition rate was quite low: 48 $^{\text{bubbles}}/_{\text{min}}$ from each of its four seeps. The resulting total rate at Heceta Deep was 192 $^{\text{bubbles}}/_{\text{min}}$. Heceta Shallow had only one stream with a rate of 240 $^{\text{bubbles}}/_{\text{min}}$.

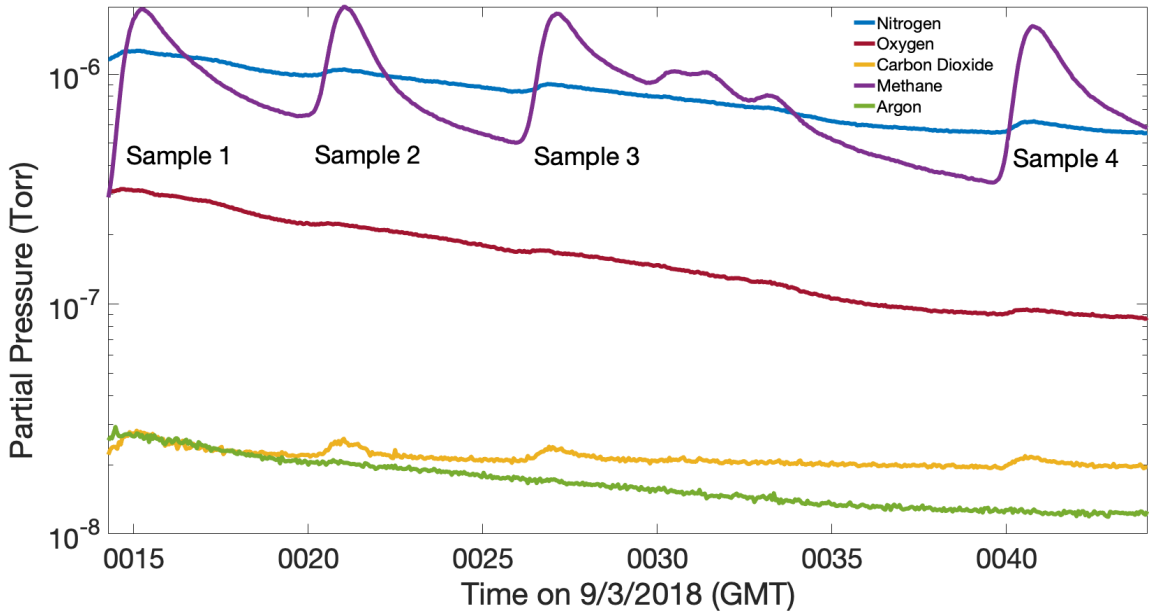

Figure 4-1: ISMS data output format for CH_4, CO_2, N_2, O_2, and Ar partial pressures at McArthur Ridge. There is a clear, large increase in the CH_4 with each sample and smaller increases in each of the other gases. The baseline of all gases is changing with time and the methods used to compensate for this are discussed in the text.

4.2 Data Processing

The data output from the ISMS reports the time course response of discrete ions representing dissolved gas partial pressures detected as mass/charge ratios (m/z) of chemical species. Figure 4-1 shows raw data from McArthur Ridge that is representative of the data collected from all sites. Each gas's contribution to the sample composition was calculated as follows:

$$F_i = \frac{S_i}{S_{CH_4} + S_{N_2} + S_{CO_2} + S_{O_2}} \tag{4.1}$$

where F is fraction of the bubble, S is gas signal, and i is the gas fraction to be calculated. Since the baseline for each of the gases was different before and after each sample (Figure 4-1), the difference between the signal's peak and where it first begins to rise is used to calculate S.

Over the course of seven dives, 95 bubble samples were collected, but there were two issues discovered in post-processing that complicated the analysis. The first problem discovered is that there were significant hydrogen sulfide (H_2S) signals at m/z 34 in some of the samples. It is unlikely that H_2S could have been directly measured by the ISMS as the

Teflon AF membrane is nearly impermeable to the gas [84]. The m/z 34 signal was likely due to a naturally occurring isotope of oxygen (^{18}O–^{16}O) that is commonly seen in the mass spectrum of O_2 at 0.35% of the predominant signal at 32 amu. In this study, each sample in which an m/z 34 signal was present, it always had a magnitude of 0.35±0.05% of the 32 amu signal.

The sites where the m/z 34 signal was non-zero were predominantly hypoxic so it is unlikely that the samples contained enough O_2 to see an m/z 34 signal. Additionally, the phenomenon was not consistent among samples within a dive or within a collection. The ratio of N_2:O_2:Ar:CO_2 in the samples in question were similar to that of atmospheric air (0.78 : 0.21 : 0.09 : 0.04). The only sources of air at the seafloor would have been in the ISMS housing or trapped in the sample lines in low-flow regions of the 3-way valves or fittings. Air intrusion from the ISMS housing is unlikely because if there was a leak in the ISMS, it would have stopped functioning due to its inability to maintain vacuum. The only remaining explanation is that the air was trapped in the sample lines when the ROV dove. All of the samples in which an m/z 34 signal was noted consisted of large volumes of gas as indicated by high total pressure measured by the ISMS. It is likely that the large volumes of gas moving through the samples lines dislodged these air bubbles and mixed with them before the sample was analyzed. There is no way to back out useful data from these contaminated samples, so if a sample's argon signal was non-zero, it was discarded. This conservative approach provides more confidence in the validity of the remaining data. The newly culled data set consisted of 61 samples.

The second concern was that the gas exchange between the bubbles collected in the funnel and the surrounding seawater would bias the data. To explore this phenomenon, the trend of gas fractions in each of the remaining collections was examined. In collections with more than one sample, the CH_4 fraction tended to rise with each sample while the fraction of the other gases decreased. These systematic changes indicate gas exchange occurring between the seawater and the gas collected in the SeaBAT funnel. The sampling procedure was not designed to constrain the rate at which this diffusion occurs so in the collections where there is more than one sample, only the first sample is assumed to be valid. This conservative parsing method leaves 22 samples from which statistical comparisons can be drawn (see Table 4.1), but bulk trends can still be seen in the larger data set. The plots showing the inter-collection gas fraction trends and table containing all 61 samples are

included in Appendix B, Figure B-1 and Table B.1.

4.3 Bubble Composition

As discussed in Section 1.4, bubble chemical composition can be used to help understand the fate of ebullitve CH_4 flux. In this study, bubble samples were collected from several geographic locations and altitudes in order to further constrain the spatial and temporal differences in CH_4 bubble chemical composition. First, the geographic differences will be analyzed by comparing each site regardless of the distribution of sample altitudes in Section 4.3.1. This will clearly identify anomalous sites before moving forward so they can be separated from the bulk data and the differences in bubble chemical compositions as a function of altitude is explored in Section 4.3.2. Finally, the results of this study are compared to others in Section 4.3.3.

4.3.1 Geographic Differences

Figures 4-2 and 4-3 show the distribution of gas fractions in all 61 samples. As discussed above, the collections in which more than one sample was taken cannot be used for a quantitative analysis, but these figures can provide a broad overview of major trends in the data. For instance, it is clear that the vast majority of each sample is comprised of CH_4. In general, the next most dominant gas is N_2 followed by CO_2. Oxygen does not often comprise more than 1% of the bubble composition. Of course, there are some collections and samples that do not follow this trend and they are discussed below.

The initial collection at Heceta Shallow has high levels of O_2 in samples 2 and 4. In sample 2, the large O_2 signal is accompanied by an anomalously high N_2 signal. These signals may be spurious, but Heceta Shallow is the only one of the four sites that was not hypoxic. It is possible for a large amount of O_2 to be stripped from the surrounding pore water or seawater. However, while the N_2 signal trends down as if it were diffusing out of the funnel collection between samples, the O_2 signal disappears completely in sample 3 and returns again in sample 4. This odd behavior casts doubt as to the validity of that measurement. As a whole, Heceta Shallow has less N_2 (often none) and slightly more CO_2 than any of the other sites. This results in CH_4 fractions close to 100%. This might result from a different form of CH_4 production that results in more pure gas than the other sites.

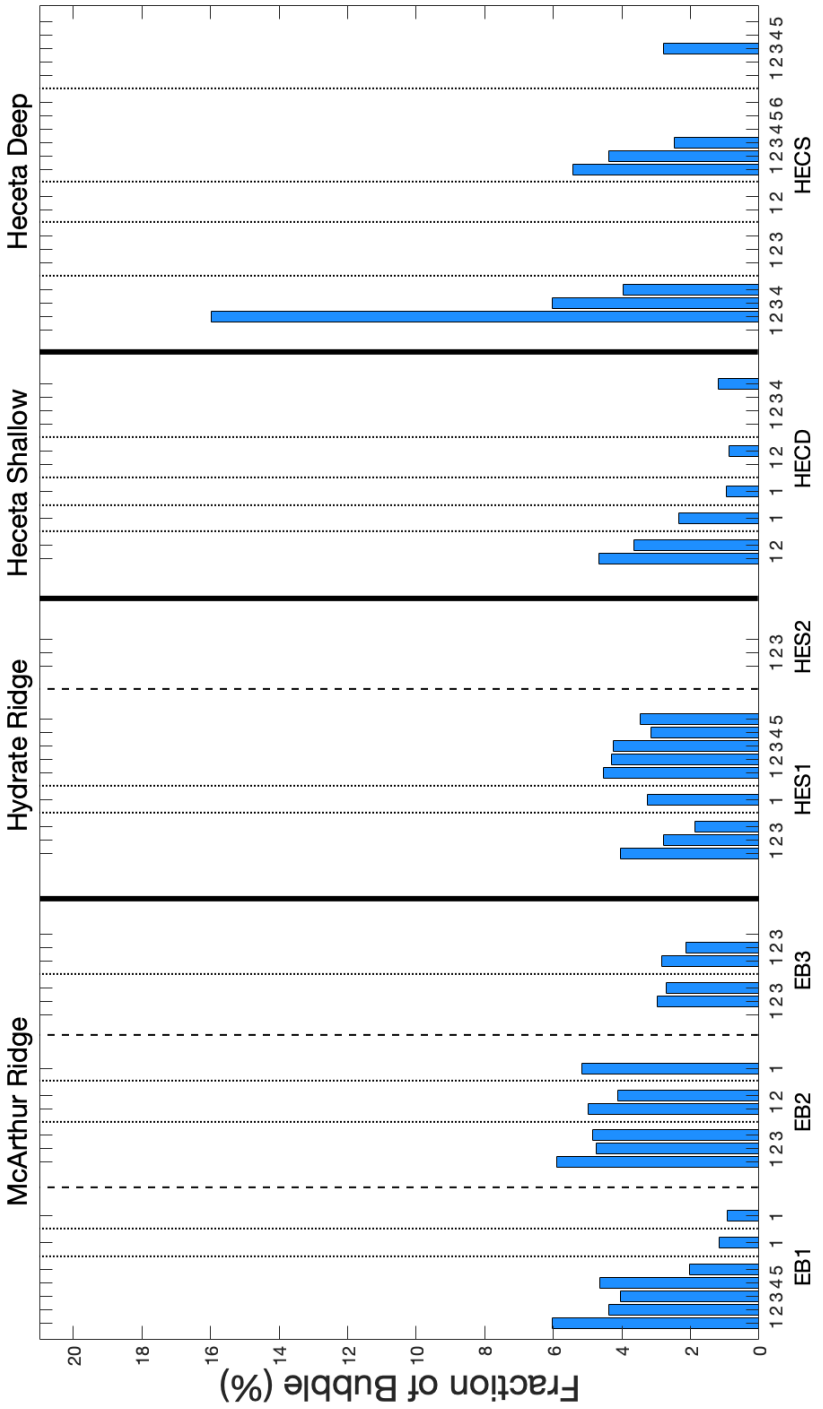

(a) N_2

Figure 4-2: Bar graphs displaying bubble composition for all samples broken out by gas. Bold lines separate the geographic sites, dashed lines separate dives at each site, and dotted lines separate collections during each dive. Data slots that are empty correspond to samples where none of the gas in question were present.

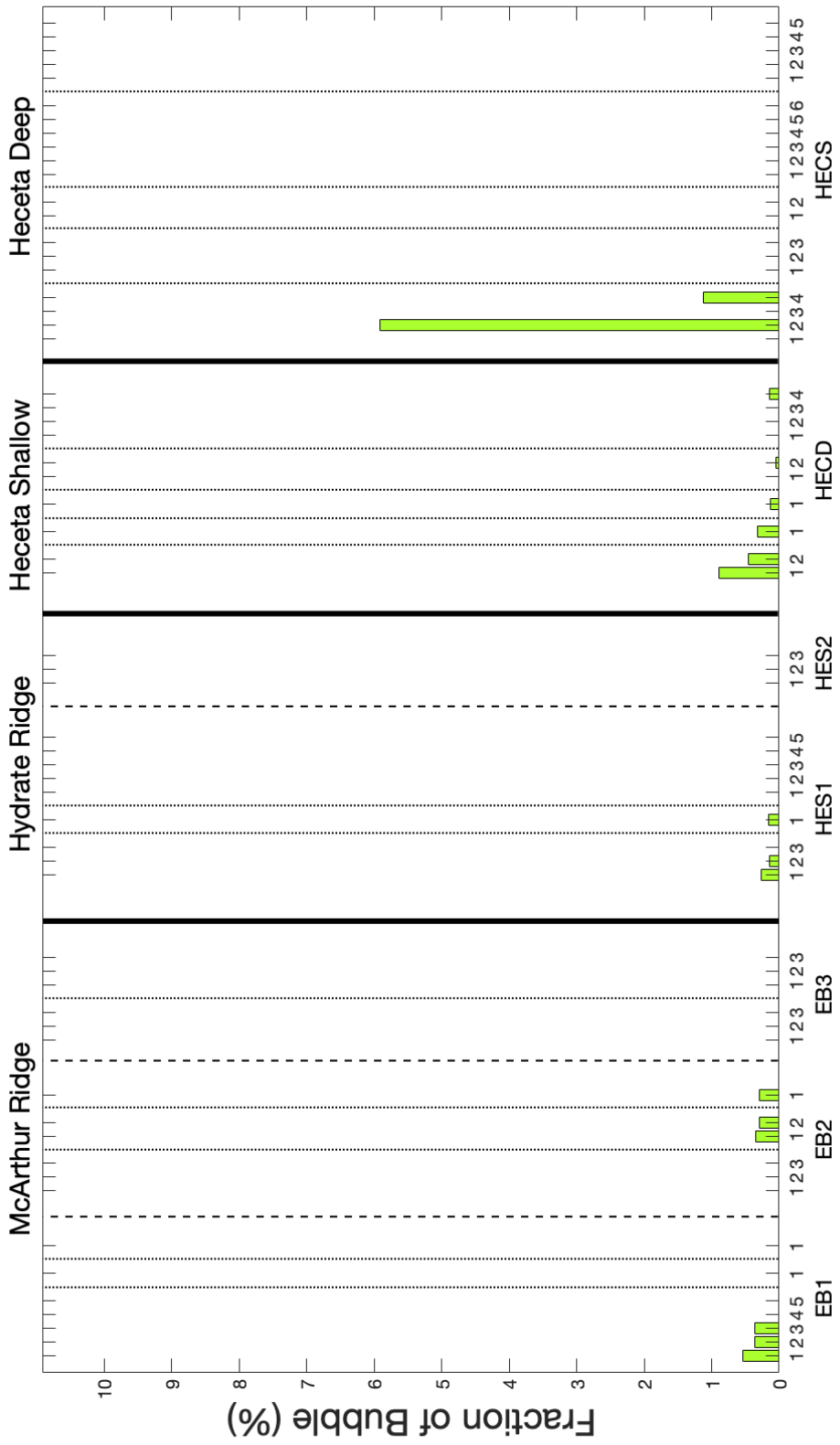

(b) O_2

Figure 4-2 continued.

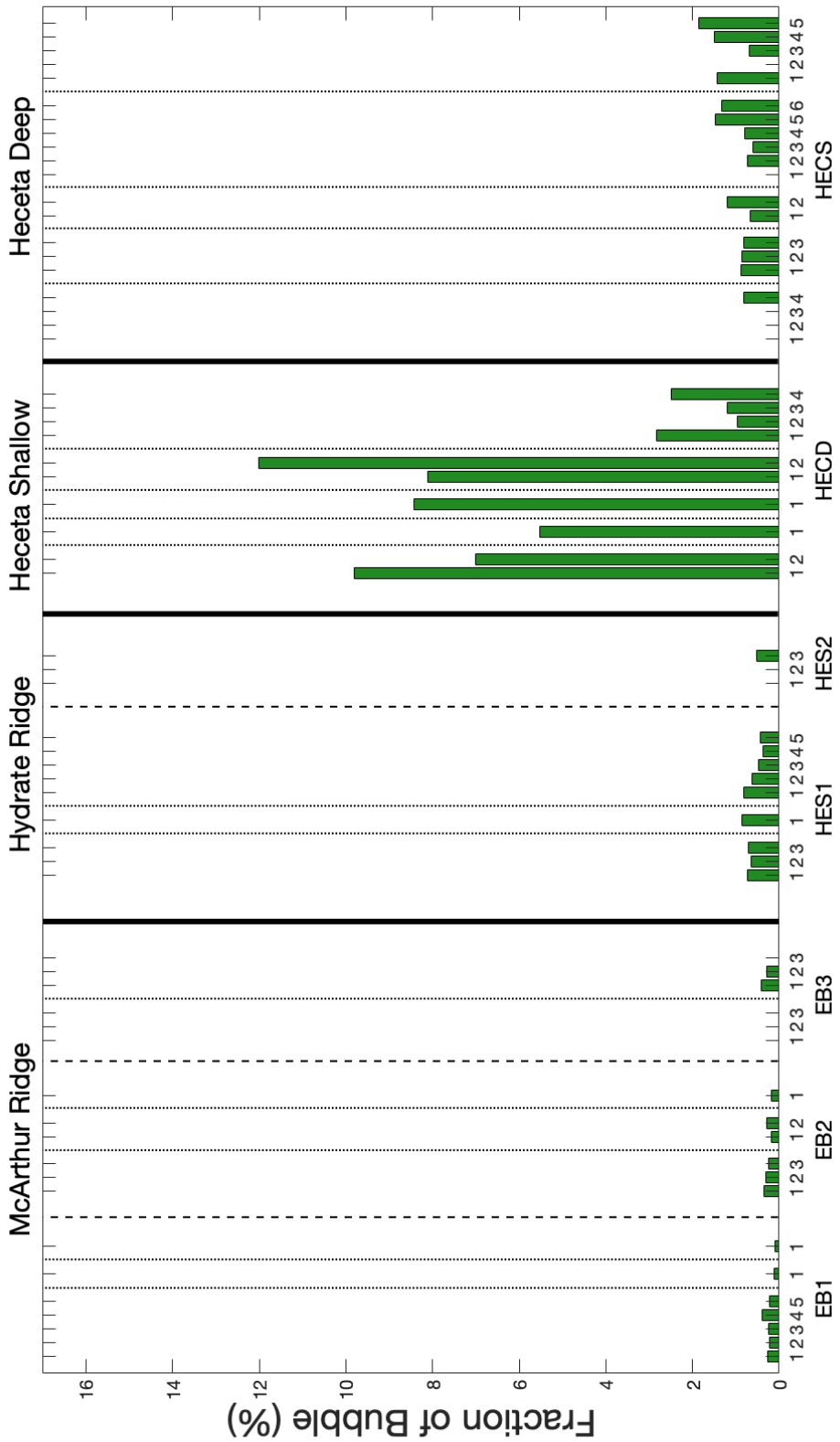

(c) CO_2

Figure 4-2 continued.

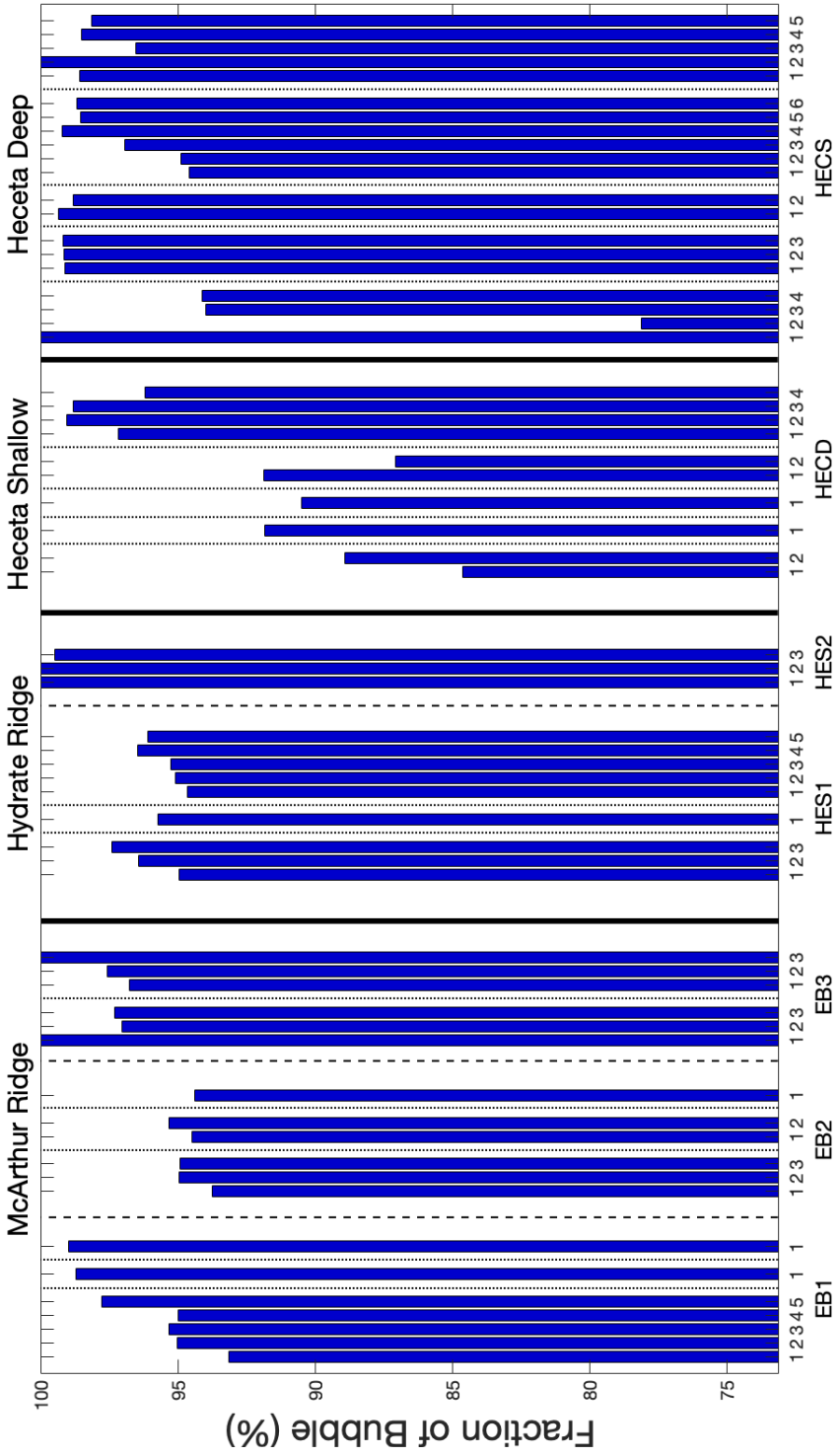

(d) CH_4

Figure 4-2 continued.

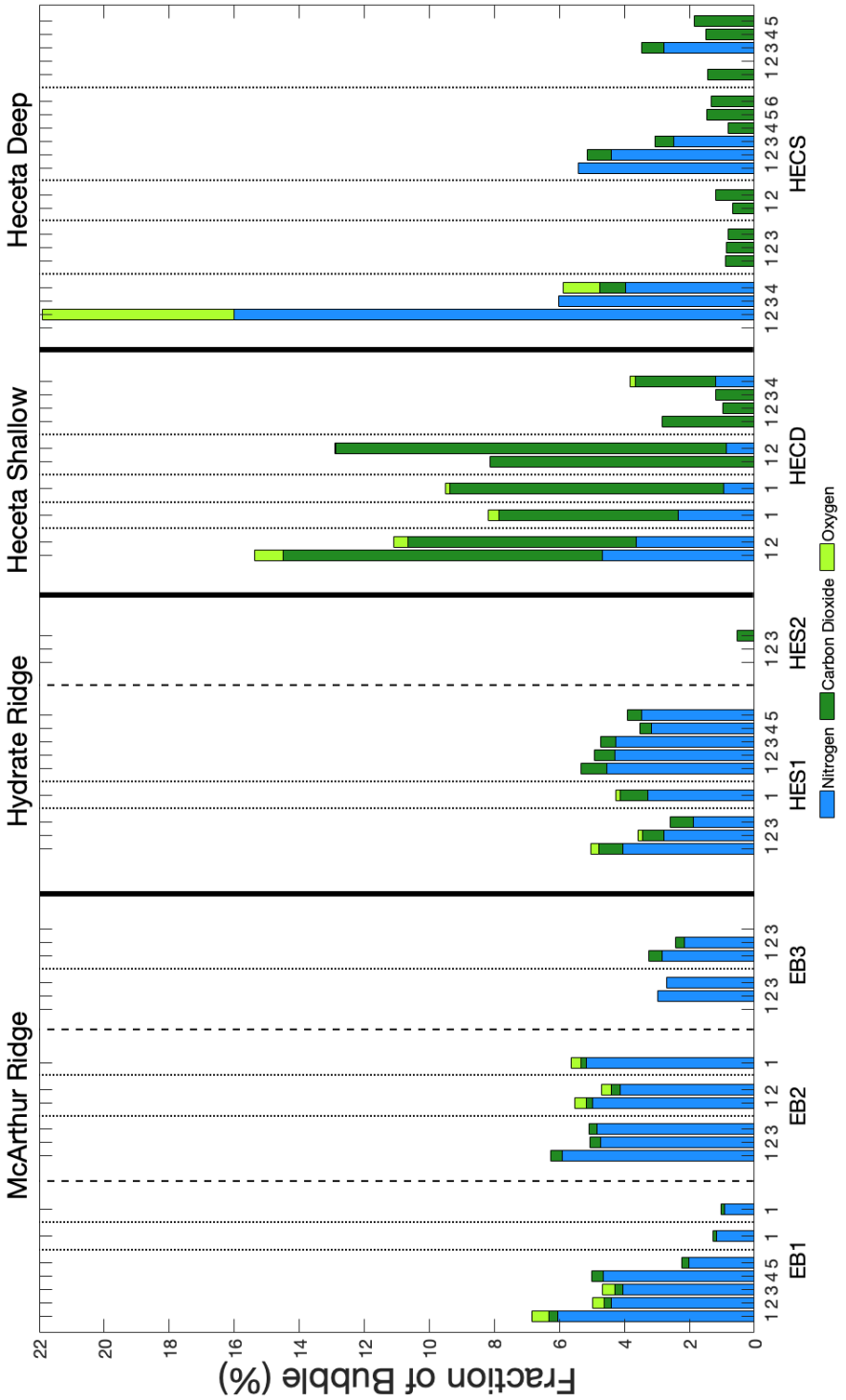

Figure 4-3: Bar graph displaying distribution of "ancillary" gases (N_2, CO_2, and O_2) for all samples. Data slots that are empty in the ancillary gas graph correspond to samples in which the bubble was 100% CH_4.

Table 4.1: List of sample depth, altitude, composition and ebullition rate. Ebullition rate is given in general terms where one dot is the least active and three dots is the most active.

					Fraction of Bubble (%)				
		Depth (m)	**Sample Id**	**Altitude (m)**	**CH_4**	**N_2**	**CO_2**	**O_2**	**Ebullition Rate**
McArthur Ridge	Eldin's Bubbles 1	832	EB1-1	1.0	93.2	6.0	0.3	0.5	○
			EB1-2	5.0	98.7	1.2	0.1	0.0	
			EB1-3	8.0	99.0	0.9	0.1	0.0	
	Eldin's Bubbles 2	830	EB2-1	0.5	93.7	5.9	0.3	0.0	○ ○ ○
			EB2-2	0.5	94.5	5.0	0.2	0.4	
			EB2-3	3.0	94.4	5.2	0.2	0.3	
	Eldin's Bubbles 3	829	EB3-1	3.0	100.0	0.0	0.0	0.0	○ ○ ○
			EB3-2	6.0	96.8	2.8	0.4	0.0	
Hydrate Ridge	Hester 1	787	HES1-1	0.5	95.0	4.1	0.7	0.3	○○
			HES1-2	0.5	95.7	3.3	0.9	0.2	
			HES1-3	10.0	94.7	4.5	0.8	0.0	
	Hester 2	775	HES2-1	10.0	100.0	0.0	0.0	0.0	○○
Heceta Bank	Heceta Deep	489	HECD-1	0.5	84.6	4.7	9.8	0.9	○
			HECD-2	0.5	91.8	2.3	5.5	0.3	
			HECD-3	0.5	90.5	1.0	8.4	0.1	
			HECD-4	0.5	91.9	0.0	8.1	0.0	
			HECD-5	26.0	97.2	0.0	2.8	0.0	
	Heceta Shallow	115	HECS-1	0.5	100.0	0.0	0.0	0.0	○
			HECS-2	0.5	99.1	0.0	0.9	0.0	
			HECS-3	0.5	99.3	0.0	0.7	0.0	
			HECS-4	0.5	94.6	5.4	0.0	0.0	
			HECS-5	0.5	98.6	0.0	1.4	0.0	

The most noticeable anomaly is the elevated CO_2 levels at Heceta Deep. It is not immediately clear what might have caused these CO_2 levels, but if the gas sampled at Heceta Deep had an increased residence time in the sediment, the bubbles might have stripped CO_2 from the surrounding pore water. The ebullition rate at Heceta Deep was among the lowest observed, but was not significantly different from the rate at Eldin's Bubbles 1 and Heceta Shallow. Heceta Deep lies at the edge of the THSZ while Eldin's Bubbles is well below the THSZ and Heceta Shallow is well above it. The effect of being at this boundary could explain an increased residence time. As discussed in Section 1.3, the migration of free CH_4 gas in sediment is not well understood. It is possible that the edge of the THSZ limits the vertical pathways available for free gas to reach the seafloor. In order to form bubbles, the gas might migrate greater horizontal distances than in other regions thus increasing the gas's residence time in sediments outside of the GHSZ. In deeper sites, the migration pathways are likely coated in hydrate so the gas is isolated from the surrounding sediments [44, 45]. This would not allow any other gases to be stripped from the surrounding pore water and would result in less CO_2 in the bubbles when they emerge from the seafloor. In shallower sites that are several hundred meters above the THSZ, the free gas must travel further in the sediment, but the migration pathways might have a more vertical structure with a less diffuse pattern resulting in shorter residence times.

In addition to THSZ proximity, the contents of the sediments at Heceta Deep may play a role in the increased CO_2 seen in those samples. If increased heterotrophic respiration exists at this site, it could have led to elevated levels of dissolved CO_2 in these sediments. This then would have increased the diffusion of CO_2 gas into the CH_4 migrating toward the sediment-water interface. Of course, increased CO_2 content in the sediment combined with long gas residence time could lead to elevated CO_2 fractions in the samples from Heceta Deep.

In order to quantify the bulk phenomena discussed above, only the first samples from each collection were used. The samples are not normally distributed, so median (M) and interquartile range (IQR) are reported in lieu of mean ±standard deviation (SD) in the text. However, all pertinent values (M, IQR, mean, SD, minimum, and maximum) are reported in Table 4.2.

The median CH_4 content in all of the samples was 95.3 % (n = 22; IQR = 5.2 %; Figures 4-4a, 4-5 - 4-7; Appendix B, Figure B-2; Table 4.2). The range of CH_4 content is rather

Table 4.2: Descriptive statistics categorized by site. The last two lines in each section give the statistics for all 22 samples with Heceta Deep removed to emphasize the overall effect the large CO_2 fractions have on the bulk statistics.

	CH_4	N_2	CO_2	O_2
Site	**M (IQR) (%)**			
McArthur Ridge	95.6 (4.8)	3.9 (4.5)	0.2 (0.2)	0.0 (0.3)
Hydrate Ridge	95.3 (3.1)	3.7 (2.7)	0.8 (0.5)	0.1 (0.2)
Heceta Deep	91.8 (4.2)	1.0 (2.9)	8.1 (3.9)	0.1 (0.5)
Heceta Shallow	99.1 (1.9)	0.0 (1.4)	0.7 (1.0)	0.0 (0.0)
All Samples	95.3 (5.2)	1.8 (4.7)	0.5 (1.3)	0.0 (0.3)
Less Heceta Deep	96.8 (4.6)	2.8 (5.0)	0.3 (0.7)	0.0 (0.2)
	Mean (SD) (%)			
McArthur Ridge	96.3 (2.7)	3.4 (2.4)	0.2 (0.1)	0.1 (0.2)
Hydrate Ridge	96.3 (2.5)	3.0 (2.0)	0.6 (0.4)	0.1 (0.1)
Heceta Deep	91.2 (4.5)	1.6 (2.0)	6.9 (2.8)	0.3 (0.4)
Heceta Shallow	98.3 (2.2)	1.1 (2.4)	0.6 (0.6)	0.0 (0.0)
All Samples	95.6 (3.8)	2.4 (2.3)	1.9 (3.1)	0.1 (0.2)
Less Heceta Deep	96.7 (2.5)	2.6 (2.6)	0.6 (0.5)	0.1 (0.1)
	Min (Max) (%)			
McArthur Ridge	93.2 (100.0)	0.0 (6.0)	0.0 (0.4)	0.0 (0.5)
Hydrate Ridge	94.7 (100.0)	0.0 (4.5)	0.0 (0.9)	0.0 (0.3)
Heceta Deep	84.5 (97.2)	0.0 (4.7)	2.8 (9.8)	0.0 (0.9)
Heceta Shallow	94.6 (100.0)	0.0 (5.4)	0.0 (1.4)	0.0 (0.0)
All Samples	84.6 (100.0)	0.0 (6.0)	0.0 (9.8)	0.0 (0.9)
Less Heceta Deep	93.2 (100.0)	0.0 (6.0)	0.0 (1.4)	0.0 (0.5)

large, spanning from 84.6 % to 100 %. The next most abundant gas was N_2 with a median measurement of 2.4 % (n = 22; IQR = 4.7 %; Figures 4-4b, 4-5 - 4-7; Appendix B, Figure B-3; Table 4.2) followed by CO_2 with a median measurement of 1.9 % (n = 22; IQR = 1.3 %; Figures 4-4c, 4-5 - 4-7; Appendix B, Figure B-4; Table 4.2). O_2 is the least abundant gas and never makes up more than 0.9 % of a sample of this truncated data set.

Now, looking closer at the median CH_4 fraction by site, Heceta Deep is anomalously low with a site median of 91.9 % (n = 5; IQR = 4.2 %; Figures 4-4a, 4-5; Appendix B, Figure B-2). Here there is a significant proportion of CO_2 as the next most abundant gas in the bubbles with a median fraction of 8.1 % (IQR = 3.9 %; Figures 4-4c, 4-5; Appendix B, Figure B-4). N_2 bubble contribution is lower than the all-sample median at 1.0 % (IQR = 2.9 %). O_2 is still present as a trace composition, but does not change from the all-sample median. Since Heceta Deep is so different than the other sites, it is useful to consider the rest of the

samples separately from its data. Table 4.2 compares each site as well as the statistics of all sites combined and without Heceta Deep. By doing this, the bias Heceta Deep imposes on the group statistics becomes clear.

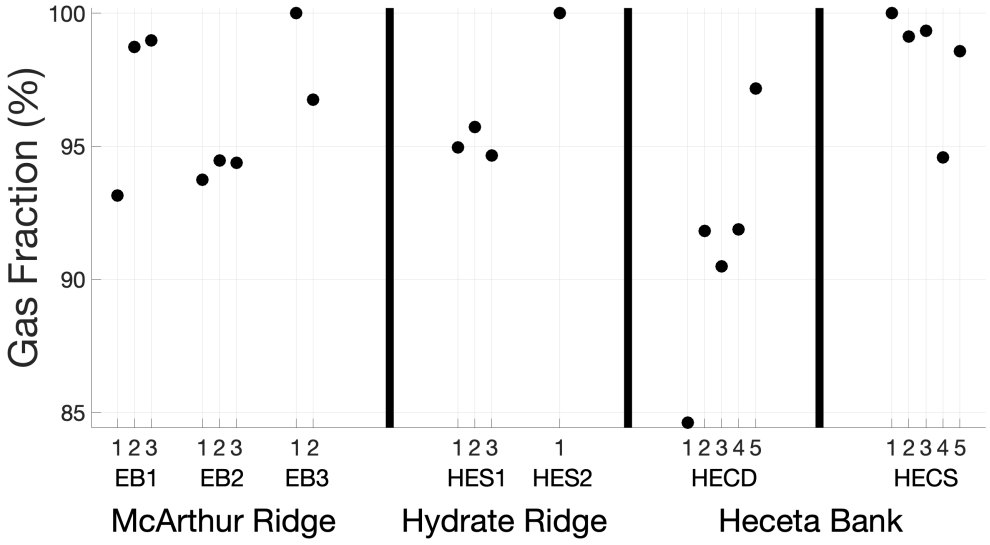

(a) CH_4 Distribution

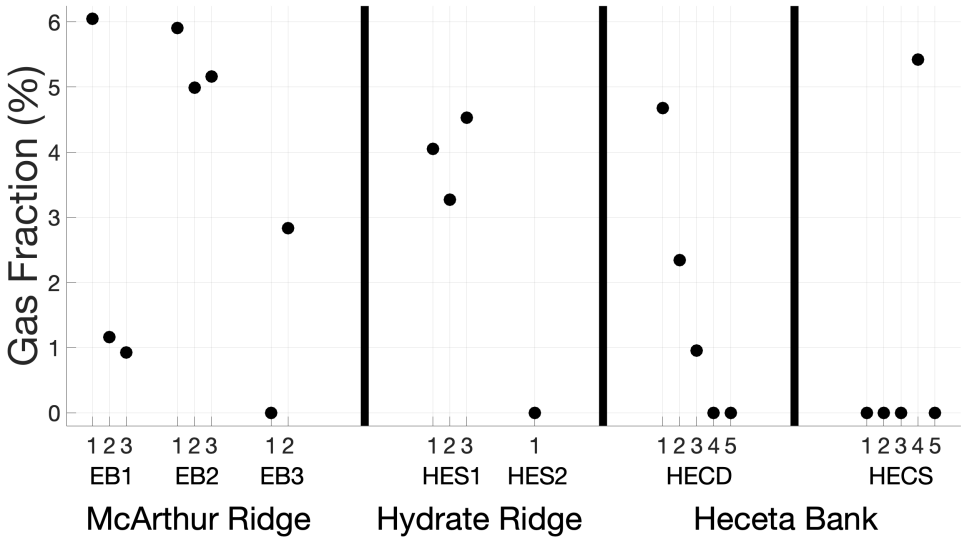

(b) N_2 Distribution

Figure 4-4: Scatter plots showing the distribution of each gas in all samples organized by location.

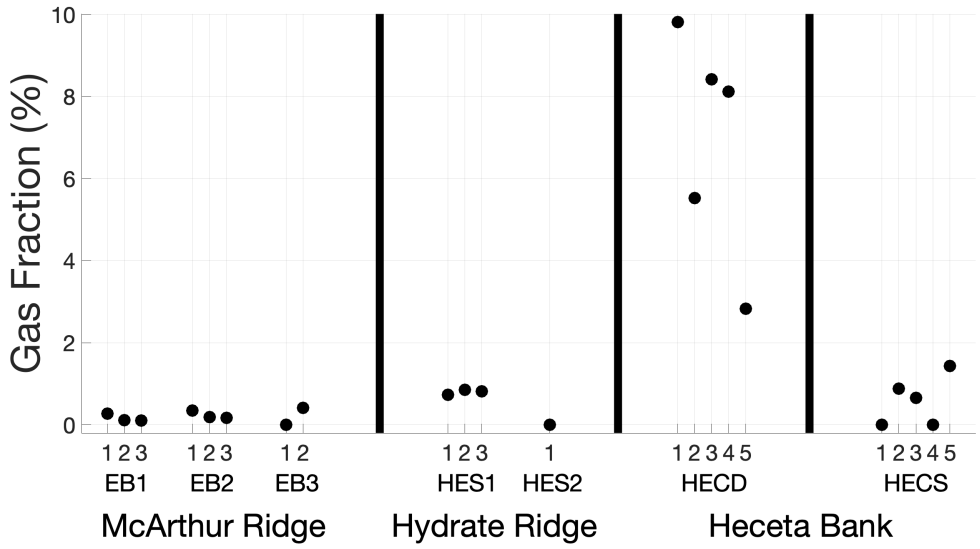

(c) CO_2 Distribution

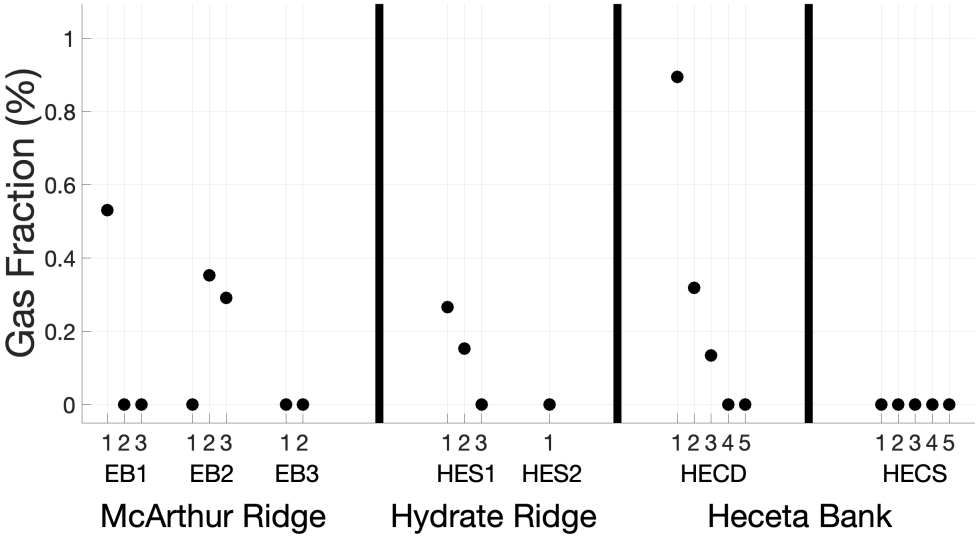

(d) O_2 Distribution

Figure 4-4 continued.

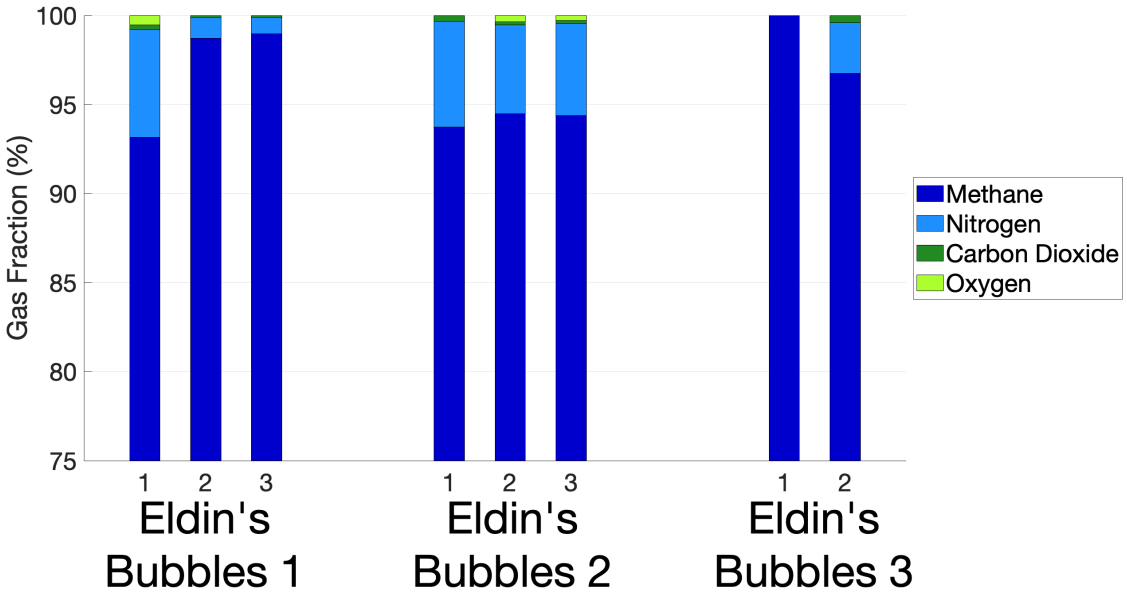

(a) McArthur Ridge Sample Composition

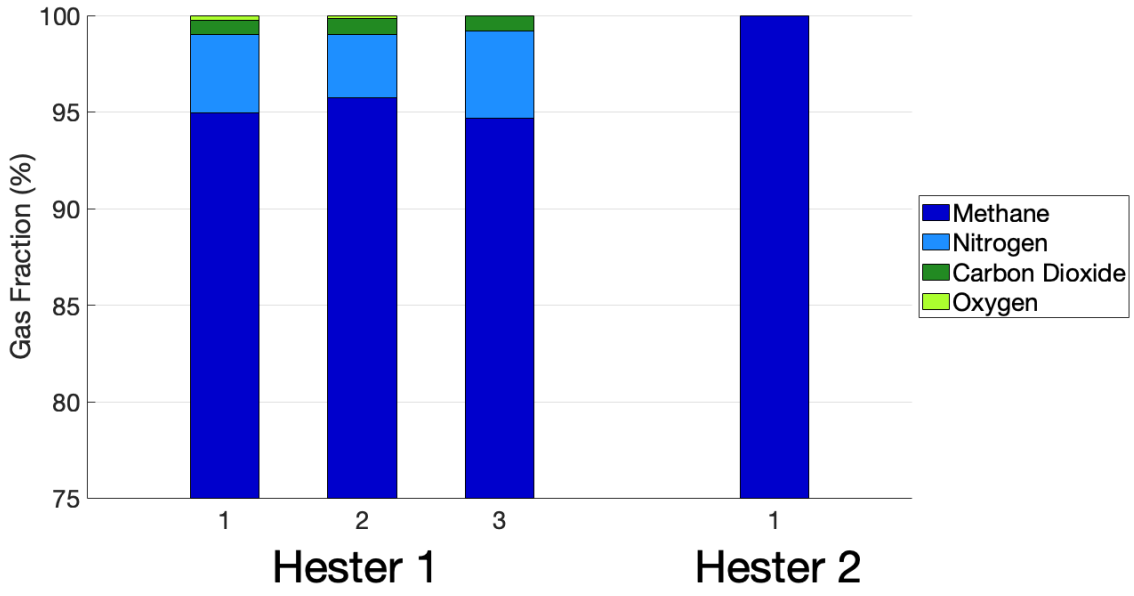

(b) Hydrate Ridge Sample Composition

Figure 4-5: Bar plots displaying the bubble composition organized by site.

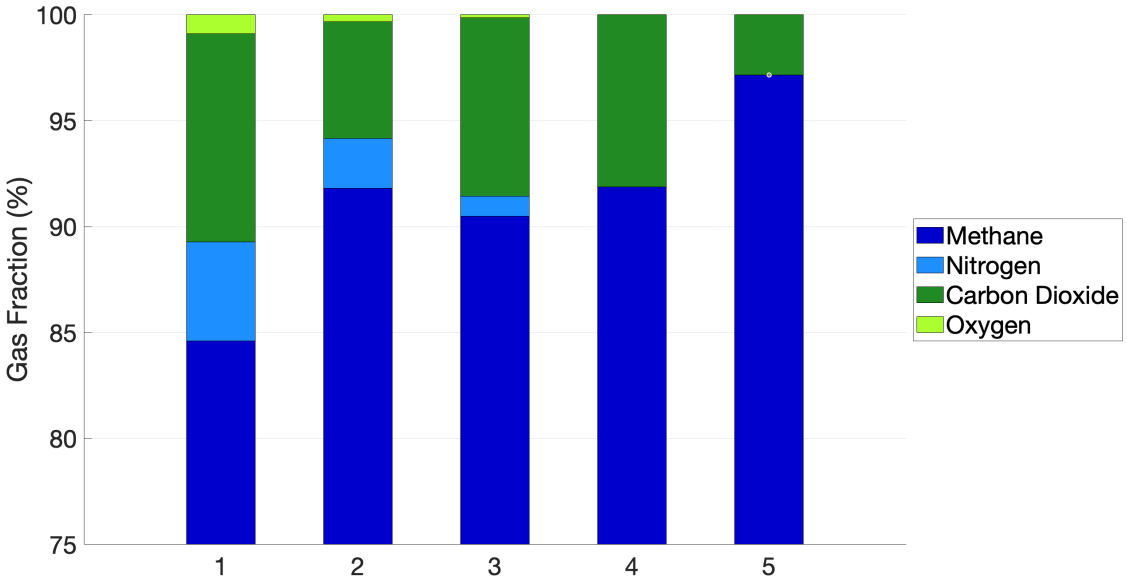

(c) Heceta Deep Sample Composition

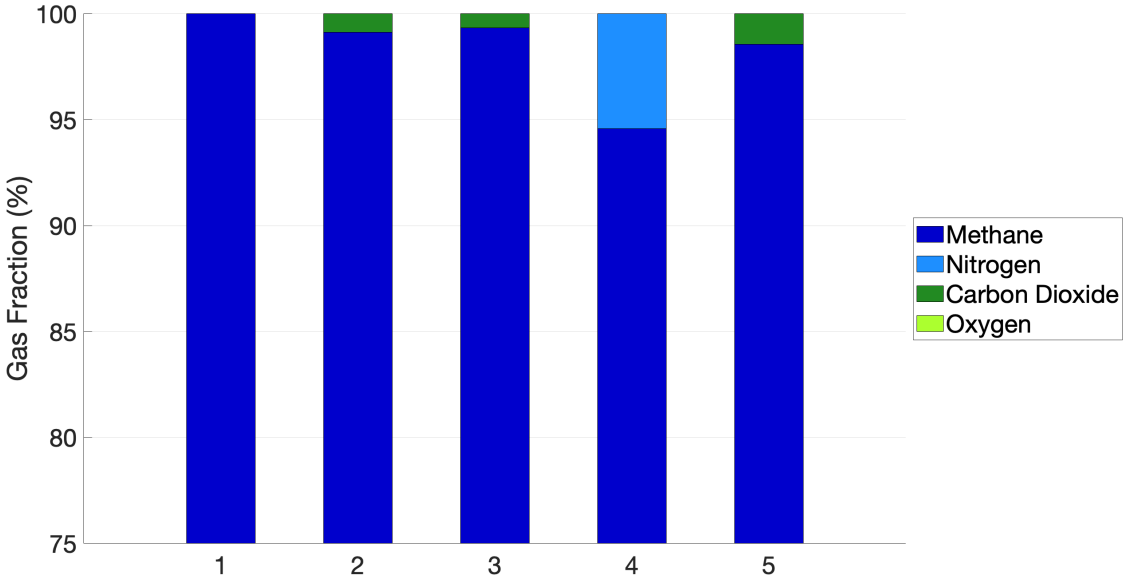

(d) Heceta Shallow Sample Composition

Figure 4-5 continued.

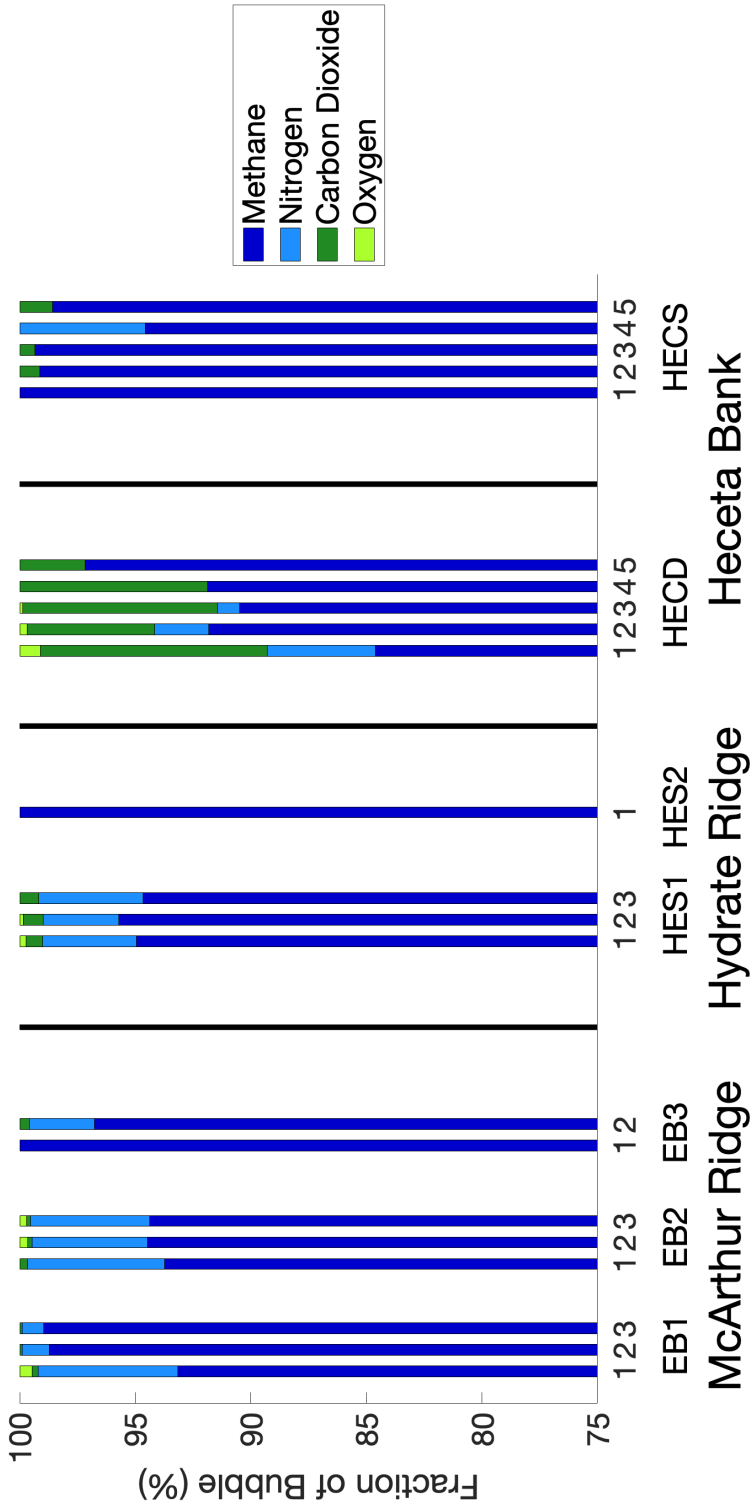

(a) All gases

Figure 4-6: Bar graphs displaying bubble composition for all samples. In the to plot, the full bubble composition is displayed while the bottom plot only displays the "ancillary" gases. Data slots that are empty in the ancillary gas graph correspond to samples in which the bubble was 100% CH_4.

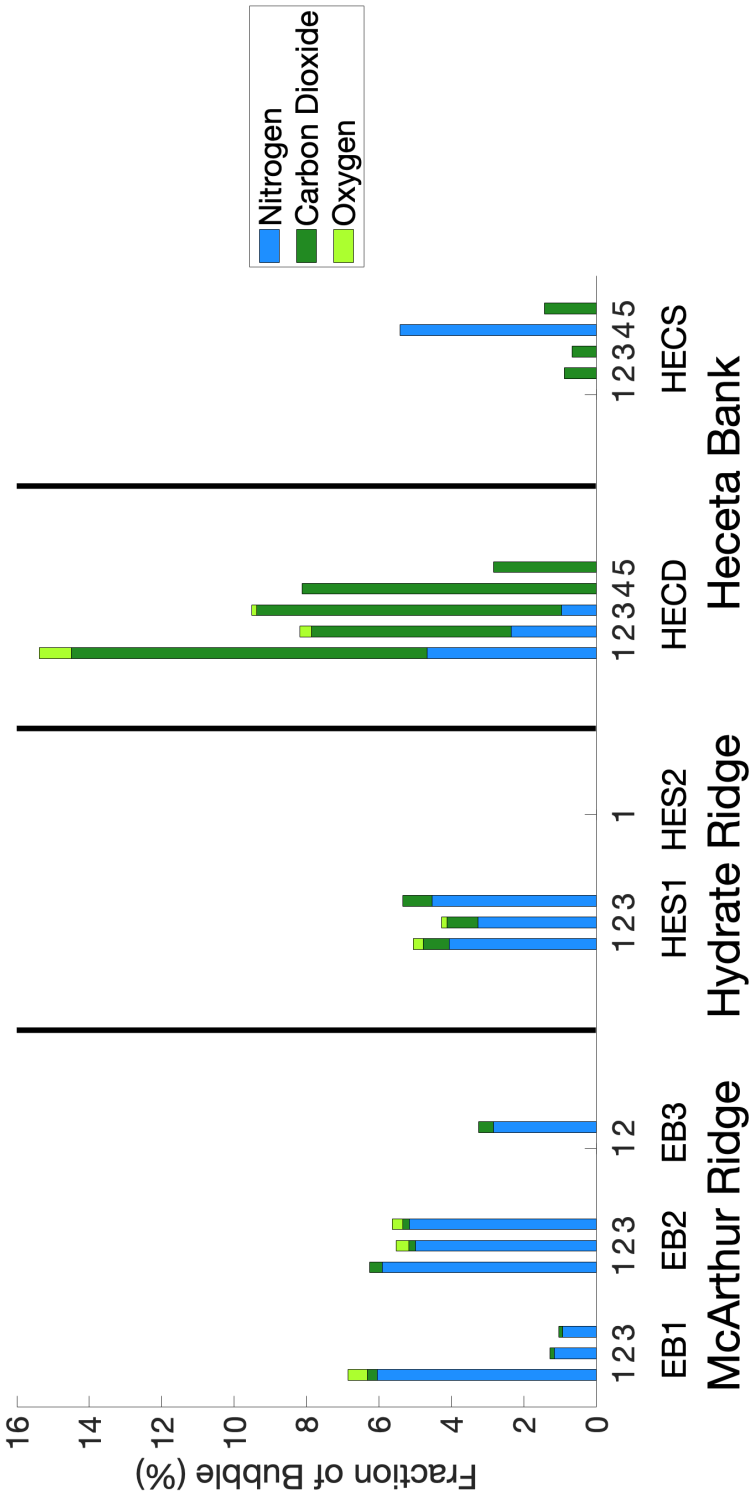

(b) Ancillary gases

Figure 4-6 continued.

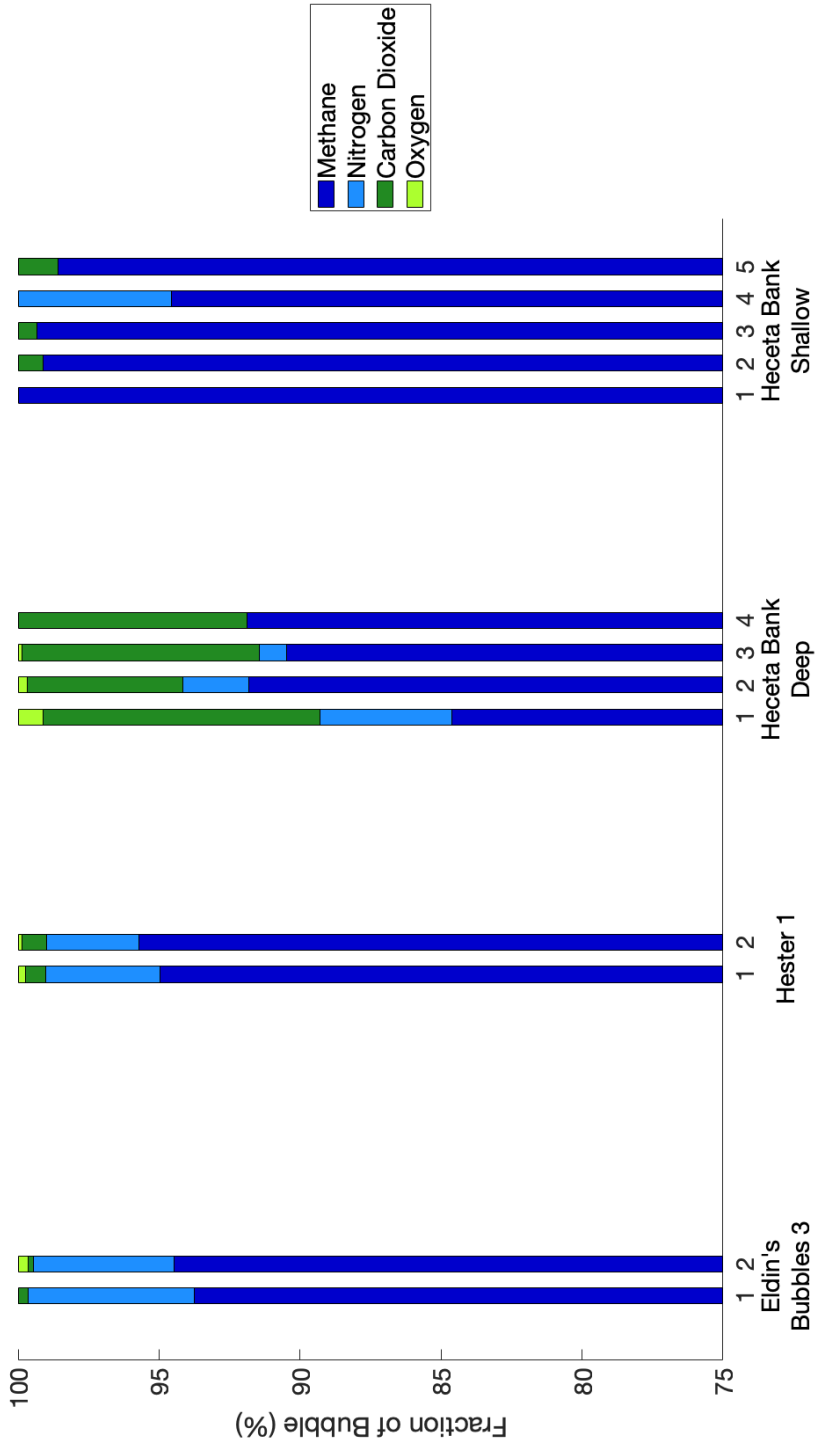

(a) All gases

Figure 4-7: Bar graphs displaying the composite picture of bubble composition of only the samples that were taken at an altitude of 0.5 m. The top graph shows the full bubble composition while the bottom graph shows only the ancillary gases. If there is an empty data slot in the ancillary gas graph, it corresponds to a sample in which the bubble was 100% CH_4.

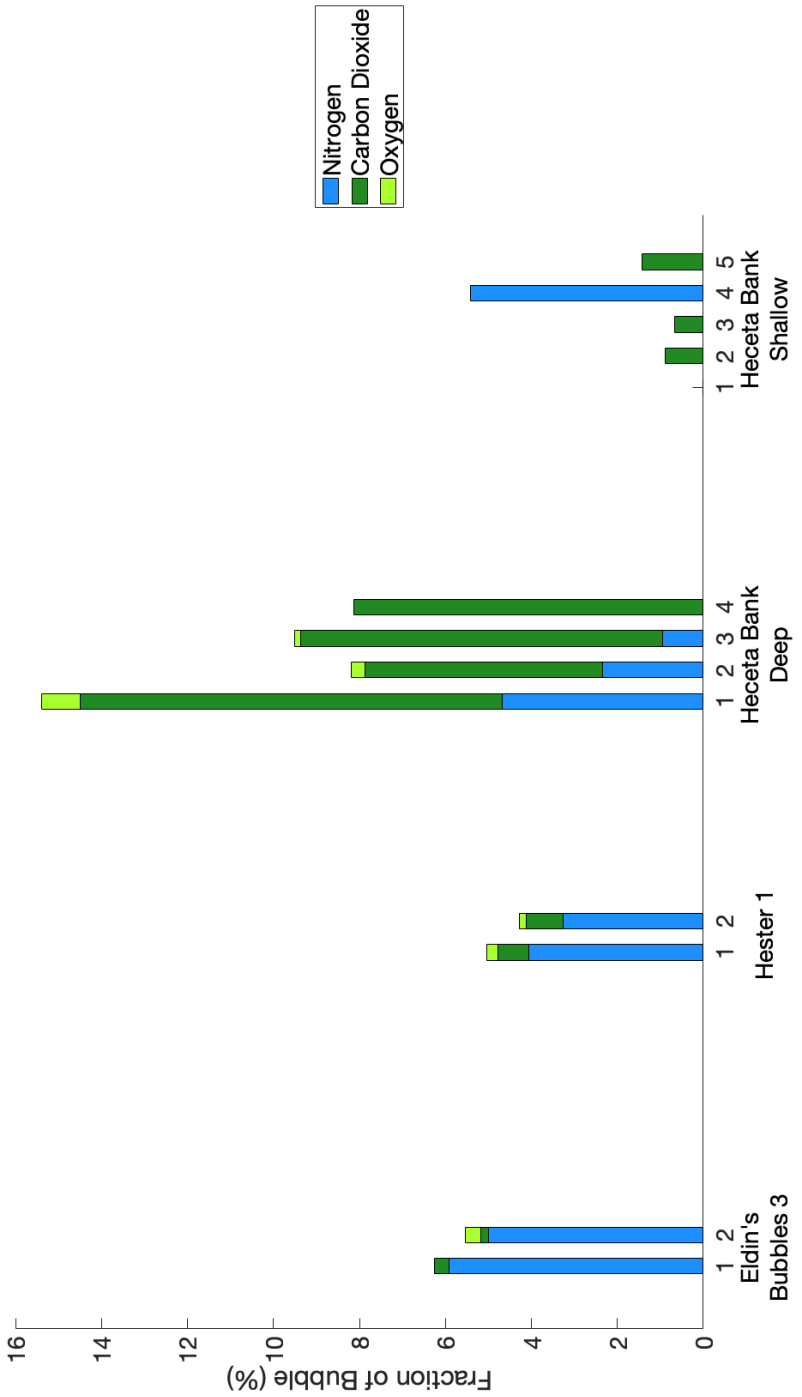

(b) Ancillary gases

Figure 4-7 continued

Table 4.3: Comparison between samples taken at 0.5 m (n = 9) and those taken above 0.5 m (n = 8) excluding those samples taken at Heceta Deep.

	CH_4	N_2	CO_2	O_2
	M (IQR) (%)			
0.5 m Samples	95.7 (4.6)	3.3 (5.1)	0.7 (0.7)	0.0 (0.2)
> 0.5 m Samples	97.7 (5.0)	2.0 (4.4)	0.1 (0.3)	0.0 (0.1)
	Mean (SD) (%)			
0.5 m Samples	96.7 (2.5)	2.6 (2.6)	0.6 (0.5)	0.1 (0.1)
> 0.5 m Samples	97.1 (2.7)	2.6 (2.4)	0.2 (0.3)	0.1 (0.2)
	Min (Max) (%)			
0.5 m Samples	93.7 (100.0)	0.0 (5.9)	0.0 (1.4)	0.0 (0.4)
> 0.5 m Samples	93.2 (100.0)	0.0 (6.0)	0.0 (0.8)	0.0 (0.5)

4.3.2 Altitude Differences

The most frequently sampled altitude in this study was 0.5 m with other samples sparsely distributed from 1-26 m. With such a wide range and sparse distribution of samples taken above 0.5 m, it is useful to approach this section with a binary view of the samples taken at and above 0.5 m. This will highlight major differences between samples taken very near the bubble source and those that have been exposed to seawater for several seconds. Heceta Deep is excluded from this analysis since four of the five samples taken there were at 0.5 m and the high levels of CO_2 will skew the results from the other sites.

There are quite large differences between the median measurements of CH_4, N_2, and CO_2 at and above 0.5 m (Table 4.3). O_2 remains the same with only slight changes in its IQR. The median CH_4 fraction increases from 95.7 % at 0.5 m to 97.7 % above 0.5 m. At 0.5 m there are higher fractions of both CO_2 and N_2. Figure 4-8 shows bubble composition broken down by gas, altitude, and site. This figure shows a general upward trend in the CH_4 fraction with altitude and a downward trend in the other gases.

Since only the ratio of gases in the bubbles is compared at each altitude, it is difficult to make any significant conclusions as to the absolute quantity of each gas because each individual fraction is dependent on the others. In other words, if O_2 leaves the bubble, it makes up a smaller part of the composition. If the other gases remain in the bubble, they will all make up a larger fraction of the composition. Thus, the trend with altitude described above could simply be an artifact of such large relative differences between the

gas fractions. For instance, consider a simple model in which all of the gases originally contained in the bubble transfer to the surrounding seawater at the same rate. The gases that make up the smaller fraction of the bubble will deplete the fastest and the gas that comprises the greatest fraction will appear to increase. The behavior of O_2 above 0.5 m is a good illustration of this phenomenon because O_2 consistently composes the smallest fraction of the samples. Additionally, there is almost no dissolved O_2 in the surrounding seawater, so any O_2 contained in the bubble will certainly dissolve quickly. Figure 4-8d shows a clear downward trend in the O_2 fraction with altitude with very low concentrations above 3 m. In reality, the dissolution rate of the gases contained in the samples is dependent on temperature, pressure, salinity, and concentration gradient and even under static conditions, each gas's solubility will differ. Taken out of context, these results can give the illusion that the dominant gas is dissolving more slowly than the other gases. In fact, previous work has suggested that 58.2 $\pm$31.1 % of the CH_4 present at the bubble origin has dissolved into the surrounding water within the range of altitudes examined in the current study [21]. The absolute concentrations of the gas inside and outside of the bubbles cannot be constrained using the current collection method so this study can make no definitive remarks on the amount of CH_4 remaining at a given altitude, but does show that the samples contain a greater fraction of CH_4 with increasing altitude in the first 26 m of travel.

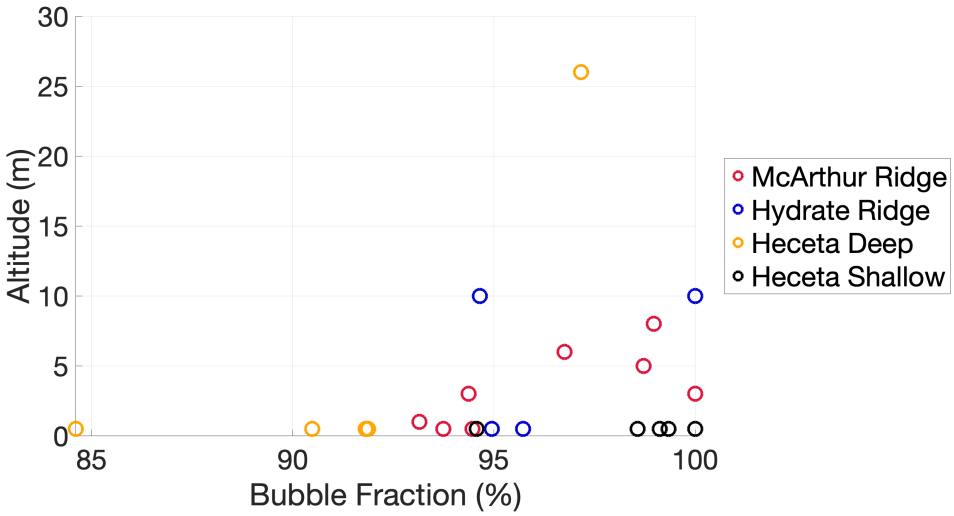

(a) CH_4 Altitude Distribution

Figure 4-8: Scatter plots showing the distribution of each gas in all samples organized by altitude.

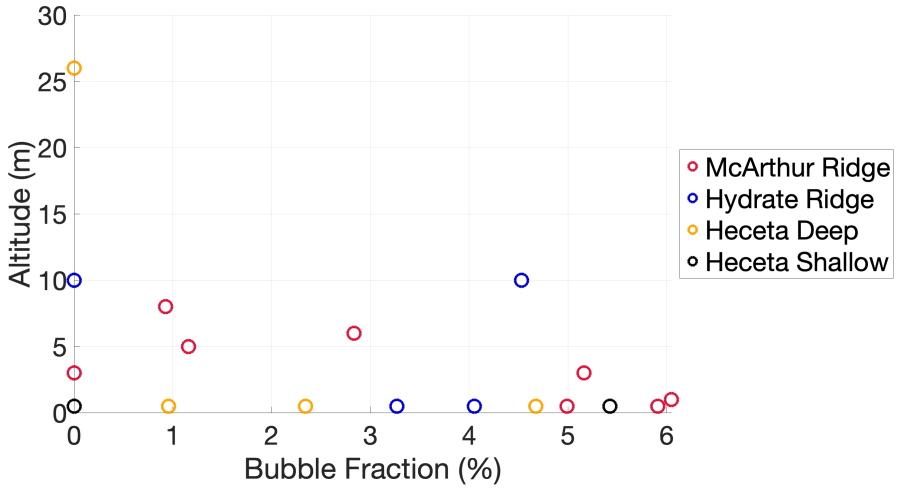

(b) N_2 Altitude Distribution

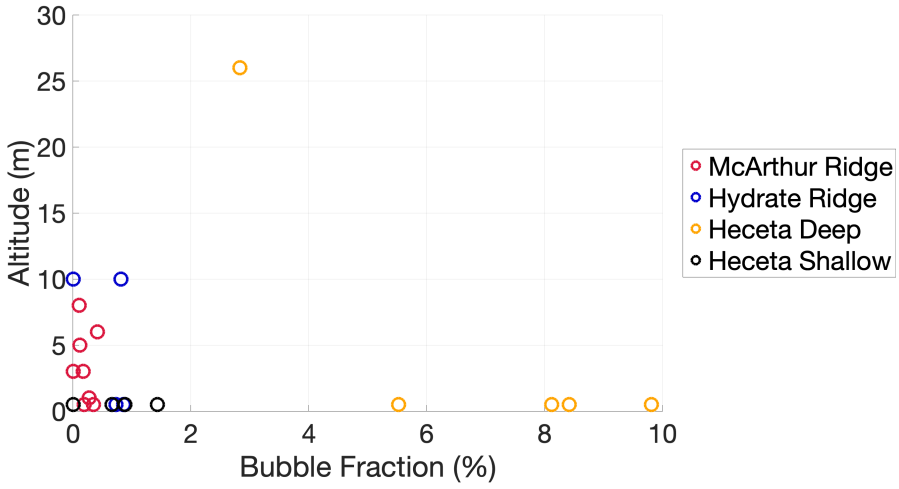

(c) CO_2 Altitude Distribution

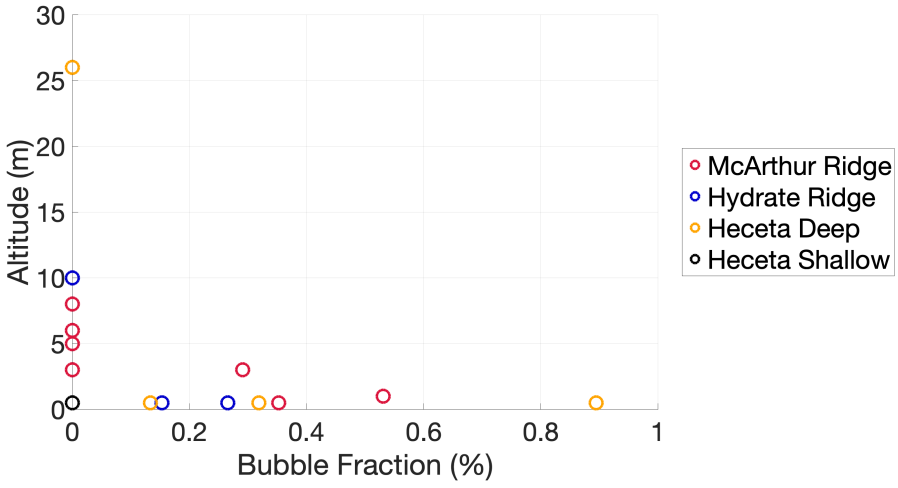

(d) O_2 Altitude Distribution

Figure 4-8 continued

4.3.3 Comparison to Other Studies

As described in Section 1.4, four other studies have performed chemical composition analyses on CH_4 bubbles. Of these studies, only one was performed in the CMSZ [71]. Baumberger *et al.* [71] found that each sample they analyzed contained greater than 98.9% CH_4 followed by small percentages of CO_2 and N_2. Of the five samples the study analyzed, the CO_2 fraction was greater than the N_2 fraction 80% of the time, but neither gas ever made up more than 0.51% of the sample.

While the study covered several locations along the CMSZ, none of the sample sites were co-located with any of the sites in the current study. The closest sample was on Heceta Bank, but is 35 km south of Heceta Deep at a depth of 1227 m. The other four sites were over 45 km from any of the sites in the current study. Disregarding geographic location, one site on the rim of Astoria Canyon in the Baumberger *et al.* study was at the edge of the THSZ at 494 m. The authors noted this site to have a vigorous bubble stream greater than any of the other sites studied. The gas from this site contained 99.6% CH_4, 0.18% CO_2, and 0.15% N_2.

These results indicate much higher levels fractions of CH_4 than did the current study. However, 36% the samples collected in the current study contained greater than 98.5% CH_4. The current study has higher temporal coverage at each seep and some of the variability (85-100% CH_4) seen in the samples from each collection could be caused by biogeochemical processes or variable gas residence times in the sediment before being released from the seafloor. On a larger temporal scale, the two studies are two years apart. Long-term changes in the morphology of the region might affect the bubble composition.

Outside of the CMSZ, three other studies with vastly different geographic and sampling conditions have been performed. Leonte *et al.* [21] reports two chemical compositions from bubble seeps in the Gulf of Mexico. Clark *et al.* has studied multiple shallow seeps (<65 m) at Coal Point off the coast of California in 2003 [85] and 2010 [54]. Despite the great spatial differences between the studies, it is useful to compare the results. Leonte *et al.* report CH_4 fractions around 70% followed by N_2 fractions between 16-19% and CO_2 fractions between 2-3%. The remainder of the bubbles consisted of higher hydrocarbons (ethane, propane, isobutane & n-butane) and O_2 was not reported. Clark *et al.* (2003) [85] report CH_4 fractions between 82-85% with CO_2 comprising a large portion of the remaining fraction

(10.5-13.4%) at the Shane seep. Finally, Clark *et al.* (2010) [54] report CH_4 fractions between 64-89% with CO_2 forming the next largest fraction between 3-25%. The authors noted that the sites with the largest CO_2 fractions also had the greatest observed oil seepage.

This final study explored three sites within 4 km of one another at Coal Point: Horseshoe, Trilogy, and La Goleta. Each of the sites were comprised of multiple seeps the authors designated sub-seeps. While the CH_4 fraction at these sites was generally smaller than that seen in the current study, the variability between the sites was quite large. In fact, at La Goleta, the CO_2 fraction at one of the sub-seeps is twice that of a second sample from the same day. This small-scale temporal variability affirms the possibility of the temporal differences seen in the current study.

4.4 Summary

Over the course of seven ROV dives, 95 bubble samples were collected between McArthur Ridge, Hydrate Ridge, Heceta Deep and Heceta Shallow. Of these 95 samples, 34 were discarded due to air intrusion and only 22 of the remaining 61 samples were used for quantitative analysis due to complications from gas diffusion during sample collection. Chemical compositional analysis revealed both horizontal and vertical spatial variation between samples. Samples from Heceta Deep contained large fractions of CO_2 that were not seen at other sites. Meanwhile, samples from Heceta Shallow were composed of more CH_4 than any other site. Vertically, samples taken at higher altitudes above the seafloor contained a greater fraction of CH_4 than samples taken at 0.5 m.

The current investigation collected more samples than any other study that has examined CH_4 bubble chemical composition. In general, the results of this study suggested lower fractions of CH_4 than did Baumberger *et al.* [71], the only other similar study performed on the CMSZ. However, this study analyzed samples *in situ* over a greater temporal range. Additionally, 36% of this study's samples were in the same range shown by Baumberger *et al.* [71]. Other studies performed at Coal Point near northern California and in the Gulf of Mexico showed bubble compositions quite different than those in the current investigation suggesting the importance of spatial differences in bubble composition [21, 54, 85].

THIS PAGE INTENTIONALLY LEFT BLANK

Chapter 5

Conclusions & Future Work

This thesis outlined the design and development of a novel *in situ* bubble sampling system and presented the findings from its first deployment. The system was deployed at the Cascadia Margin in 2018 where it was used to collect 95 bubble samples on a total of seven ROV dives at four sites: McArthur Ridge, Hydrate Ridge, Heceta Deep and Heceta Shallow. In post processing, 35 samples were discarded due to contamination leaving 61 samples – six times greater than any other study of its kind. Of the remaining samples in this subset, only 22 were used for quantitative analysis due to evidence of inter-collection gas diffusion, but the bulk set was used to observe bulk trends. This large increase in samples coupled with the use of *in situ* instrumentation resulted in unprecedented spatial and temporal coverage of CH_4 seep bubble chemical composition.

Understanding the spatial and temporal dynamics of CH_4 bubbles is critical for understanding ebullitive CH_4 flux to the shallow ocean and atmosphere. The results from the 2018 deployment revealed variable compositions over horizontal and vertical distributions. Additionally, the inter-sample composition revealed small-scale temporal variability. As a whole, the results presented here show that the BDS is a viable tool for future exploration of CH_4 bubble seep sites, but lessons learned from its deployment and questions raised from the composition of the samples it collected are worthy of future work.

5.1 Future Work

5.1.1 BDS and Sampling Improvements

There are several modifications that should be made to the BDS in order to improve the sampling process for future deployments. The three main features that should be addressed are (1) the reintegration of the BAC and HPA into the sampling procedure, (2) automation of sample collection procedure, and (3) simplification of the sample lines.

While the modifications of the BDS presented in Section 3.2.1 were successful, the ability to employ the BAC and HPA would better quantify the chemical composition of the samples. There are several problems with analyzing a slug of gas as it moves through the sample lines. First, the bubbles move past the membrane at $125\,^{\mathrm{mL}}/_{\mathrm{min}}$ so the gas only has a few seconds to diffuse across the membrane. Thus, the differential rates at which each gas of interest diffuses across the membrane might change the chemical composition results. Additionally, the gas moving through the samples lines diffuses into the water upstream and downstream of the slug and creates a gradient effect in the sample signal. The slowly rising and falling signal as a result of this gradient effect makes it difficult to establish a baseline or define a sample start and stop time when determining signal amplitude. Finally, the fluid flow through the membrane inlet used in the deployment configuration is tortuous with tight angles that can result in the slug breaking up into smaller bubbles and gas remaining in the membrane inlet after the sample.

Use of the BAC would mitigate the effects of all of these problems. Since the gas headspace in the BAC is constantly monitored by the ISMS, there is ample time for the gas in each sample to diffuse across the membrane for analysis. Some of the gas from the sample would still diffuse into the water up and downstream of the slug of gas moving from the SeaBAT to the BAC, but the gradient effect seen in the ISMS output would be minimal because the ISMS is not monitoring the water. While the flow path between the SeaBAT and the ISMS is still tortuous, the use of the BAC would eliminate the sharp angle introduced by the deployment membrane inlet so the fluid dynamics at the membrane would not need to be considered in processing the data.

The tortuous flow path between the SeaBAT and the BAC potentially resulted in the inability to transfer bubbles to the BAC. Reducing the number of fittings and valves between the SeaBAT and the BAC could improve the user's ability to use the BAC. Additionally,

reducing the number of fittings and valves would leave fewer places for air from the surface or hydrate-coated bubbles to collect, resulting in fewer air contaminated samples and trips out of the GHSZ to dissociate the accumulated hydrates. Removing the three-way valves would lower the sampling efficiency because the ISMS and laser spectrometer could not be used in tandem, but the improved sample quality could compensate for the loss. The number of fittings can be reduced by better planning the location of each of the components and using bent tubing rather than angled fittings to make turns.

The final major design improvement is the automation of the sampling procedure. The current method of toggling the SeaBAT valve is not precise as it relies on the user to dictate the amount of time the gear pump pulls gas out of the sample funnel. If the SeaBAT valve toggle signal was regulated by a microcontroller, the samples would be much more uniform and the reproducibility of the results would be improved.

5.1.2 Bubble Composition

While some possible explanations for the incongruous CO_2 fractions at Heceta Deep are presented in Section 4.3.1, the true cause is unknown. Analysis of sediment samples collected during the cruise could provide information about the microbial communities or organic material content might reveal clear differences from the other sites. Analysis of drill cores and seismic reflection surveys could provide interesting information regarding the bubble seep's exact proximity to the THSZ and the diffusivity of the gas migration pathways. Finally, simply returning to the site to collect more bubble samples could reveal that the abnormality resulted from temporal variability in the seep.

Improved vertical sample resolution could provide insight into the dissolution rate of each of the gases present in the bubble. As noted in Section 4.3.2, the resolution of this study only allowed for a binary view of the differences in bubble composition as a function of altitude. Samples taken at multiple altitudes at each site would reveal dissolution rates at each site during post processing. This information combined with detailed dissolved gas content of the ambient seawater can be used to refine the current models of CH_4 dynamics.

Appendices

Appendix A

Arduino Code

```
int in1 = 7; // relay 1 (Purge Valve)
int in2 = 6; // relay 2 (HP Valve)
int in3 = 5; // relay 3 (Heater)

// assign data types
unsigned long ticker;
unsigned long hpLong;
unsigned long hpShort;
unsigned long heater;

void setup() {
  // initialize serial communication at 9600 bps
  Serial.begin(9600);
  Serial.println("Serial Ready");
  pinMode(in1, OUTPUT); // defines function of in1 (pin 7) as an output pin
  pinMode(in2, OUTPUT); // defines function of in2 (pin 6 )as an output pin
  pinMode(in3, OUTPUT); // defines function of in3 (pin 5) as an output pin
  // relays begin open (not actuated) by setting pin output to LOW
  digitalWrite(in1, LOW);
  digitalWrite(in2, LOW);
  digitalWrite(in3, LOW);
}
void loop() {
  ticker = millis(); // mark time at beginning of loop
  handleSerial();  // handle incoming serial data
  waitTime(); // background timer function
```

```
}
// following function will take single byte commands from the emulator and cycle the relays.
void handleSerial() {
  while(Serial.available()>0){ // while there is data in the serial buffer
    char commandIn = Serial.read(); // read the first bye in the buffer
    switch(commandIn) {
//  Opens HP Valve for 3 seconds if the Purge valve is NOT open and shuts again with no further operator action
      case '1':
      if(digitalRead(in1) == LOW) { // check to see if the Purge Valve is open
        // if it is, display this error message
        Serial.println("Cannot Open HP Valve because Purge Valve is Open");
      }
      else { // if the Purge valve isn't open, then open the HP valve
      digitalWrite(in2, LOW);
      hpLong = millis(); // mark time for the long HP valve timer
      Serial.println("HP Valve Open");
      }
      break;

// Opens HP valve if the Purge valve is NOT open for 50 ms and shuts again with no further operator action
      case '2':
      if(digitalRead(in1) == LOW) { // check to see if the Purge Valve is open
        // if it is, display this error message
        Serial.println("Cannot Open HP Valve because Purge Valve is Open");
      }
      else { // if the Purge valve isn't open, then open the HP valve
      digitalWrite(in2, LOW);
      hpShort = millis(); // mark time for the short HP valve timer
      Serial.println("HP Valve Open");
      }
      break;

// Opens Purge Valve as long as HP Valve is not open.  No time limit.
      case '3':
      if (digitalRead(in2) == LOW) { // checks to see if the HP valve is open
        // if it is, display this error message
```

```
63          Serial.println("Cannot open Purge Valve because HP Valve is open");
64        }
65        else {
66          digitalWrite(in1, LOW); // if not, open the valve
67          Serial.println("Purge Valve Open");
68        }
69        break;
70 // Shuts Purge Valve
71        case '4':
72        digitalWrite(in1, HIGH); // shuts Purge valve
73        Serial.println("Purge Valve Shut");
74        break;
75
76 // Turns on heater for 30 seconds and turns off without operator action
77        case '5':
78        digitalWrite(in3, LOW); // energize heater
79        heater = millis(); // mark time for heater timer
80        Serial.println("Heater is ON");
81        break;
82
83 // Turns heater off
84        case '6':
85        digitalWrite(in3, HIGH); // secure heater
86        Serial.println("Heater is OFF");
87        break;
88
89 // Deenergizes all equipment
90        case'7':
91        digitalWrite(in3, HIGH); // secure heater
92        digitalWrite(in2, HIGH); // shut Purge valve
93        digitalWrite(in1, HIGH); // shut HP valve
94        Serial.println("All equipment has been deenergized");
95        break;
96      }
97    }
98 }
99 // Defines wait time function:  the basic use of this function is to track the
       mark time variables from the serialInput function from above and cycle
      valves/heater power as necessary.
```

```
100 void waitTime(){
101  // shut HP valve after 3 seconds
102  if (hpLong != 0 && ticker - hpLong == 3000UL){
103       digitalWrite(in2, HIGH); // shut the HP valve
104       Serial.println("HP Valve Shut");
105       Serial.println("HP valve was actuated for 3 seconds");
106       hpLong = 0; // resets the mark time variable to zero to stop repeat
      execution.
107   }
108   // shut HP valve after 50 milliseconds
109   if (hpShort != 0 && ticker - hpShort == 50UL) {
110     digitalWrite(in2, HIGH); // shut HP valve
111     Serial.println("HP valve opened for 50 miliseconds");
112     hpShort = 0; // resets the mark time variable to zero to stop repeat
      execution
113   }
114   // warn that heater has been on for 15 seconds
115   if (heater != 0 && ticker - heater == 15000UL) {
116         Serial.println("Heater will turn off in 15 seconds");
117   }
118   // secure heater after 30 seconds
119   if (heater != 0 && ticker - heater == 30000UL) {
120     digitalWrite(in3, HIGH); // secure heater
121     Serial.println("Heater was automatically turned off");
122     heater = 0; // resets mark time variable to zero in order to prevent
      repeat execution
123   }
124 }
```

Algorithm 2 `handleSerial()` — Takes incoming serial data and performs an action

Let $serialBuffer$ be an array of length n {$serialBuffer$ is a dynamic array whose length can change if data is received faster than it is processed}
while $n > 0$ **do**
  for $i = 1$ **to** n **do**
    $commandIn \leftarrow serialBuffer[1]$
    if $commandIn = 1$ **then**
      if $in1 = HIGH$ **then**
        $in2 \leftarrow LOW$; $hpLong \leftarrow millis()$ {$millis()$ is a built in Arduino function that marks the elapsed time since the Arduino booted up}
      else {$in1 = LOW$}
        Print: "Cannot open High Pressure Solenoid because Purge Valve is open."
      end if
    end if
    if $commandIn = 2$ **then**
      if $in1 = HIGH$ **then**
        $in2 \leftarrow LOW$; $hpShort \leftarrow millis()$
      else {$in1 = LOW$}
        Print: "Cannot open High Pressure Solenoid because Purge Valve is open."
      end if
    end if
    if $commandIn = 3$ **then**
      if $in2 = HIGH$ **then**
        $in1 \leftarrow LOW$
      else {$in1 = LOW$}
        Print: "Cannot open Purge Valve because High Pressure Solenoid is open."
      end if
    end if
    if $commandIn = 4$ **then**
      $in1 \leftarrow HIGH$
    end if
    if $commandIn = 5$ **then**
      $in3 \leftarrow LOW$; $heater \leftarrow millis()$
    end if
    if $commandIn = 6$ **then**
      $in3 \leftarrow HIGH$
    end if
    if $commandIn = 7$ **then**
      $in3 \leftarrow HIGH$; $in2 \leftarrow HIGH$; $in1 \leftarrow HIGH$
    end if
    $serialBuffer[1] = []$
    $serialBuffer$ is now an array of length $n - 1$ {Assuming no more data has entered the Serial Buffer}
  end for
end while

Algorithm 3 `waitTime()` — runs a timer in the background

1: **if** *hpLong* **not** equal to 0 **and** $ticker - hpLong = 3000$ **then**
2: $in2 \leftarrow HIGH$
3: Print: "HP Valve Shut" **and** "HP Valve was open for 3 seconds."
4: **end if**
5: **if** *hpLong* **not** equal to 0 **and** $ticker - hpShort = 50$ **then**
6: $in2 \leftarrow HIGH$
7: Print: "HP Valve Shut" **and** "HP Valve was open for 50 milliseconds."
8: **end if**
9: **if** *heater* **not** equal to 0 **and** $ticker - heater = 15000$ **then**
10: Print: "Heater will turn off in 15 seconds"
11: **end if**
12: **if** *heater* **not** equal to 0 **and** $ticker - heater = 30000$ **then**
13: $in3 \leftarrow HIGH$
14: Print: "Heater was automatically turned off."
15: **end if**

Appendix B

Additional Data Figures

Figures to supplement the discussion in Chapter 4 are provided on the following pages.

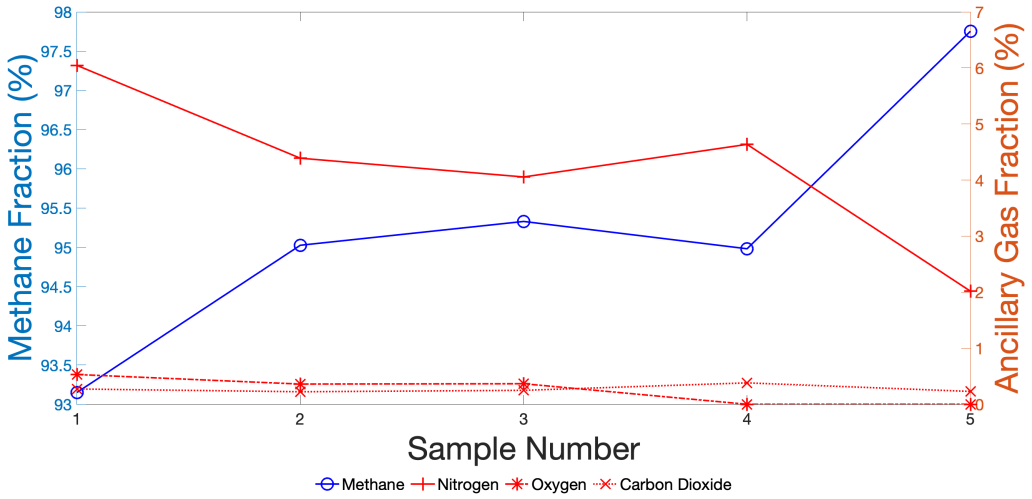

(a) Eldin's Bubbles 1 - Collection 1

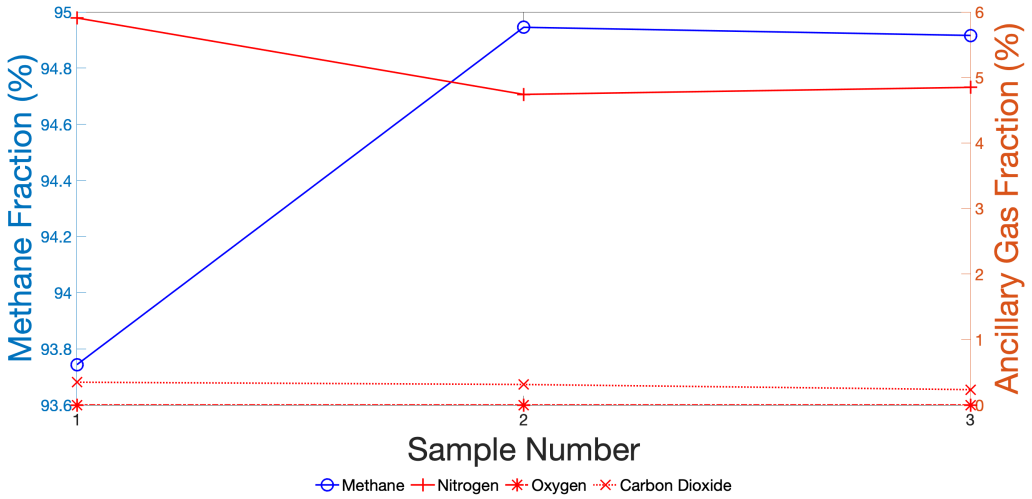

(b) Eldin's Bubbles 2 - Collection 1

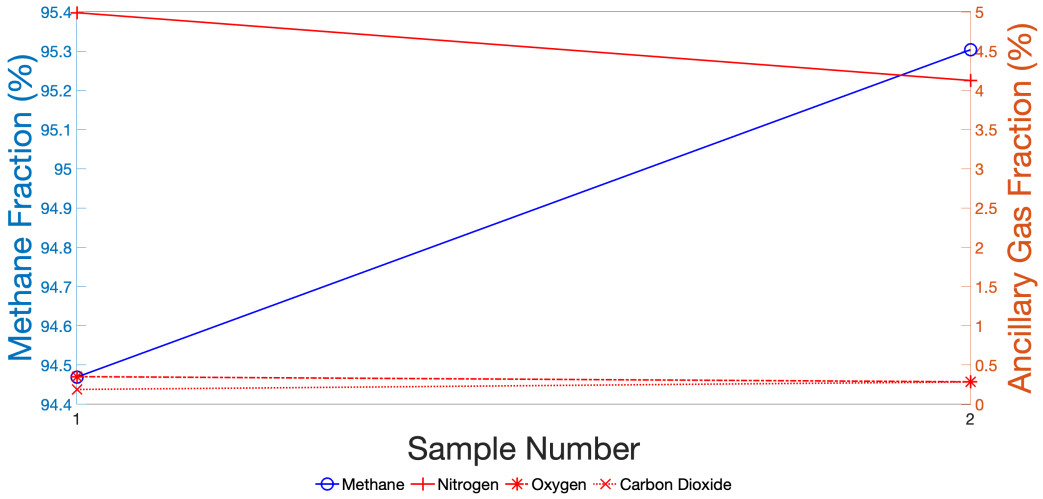

(c) Eldin's Bubbles 2 - Collection 2

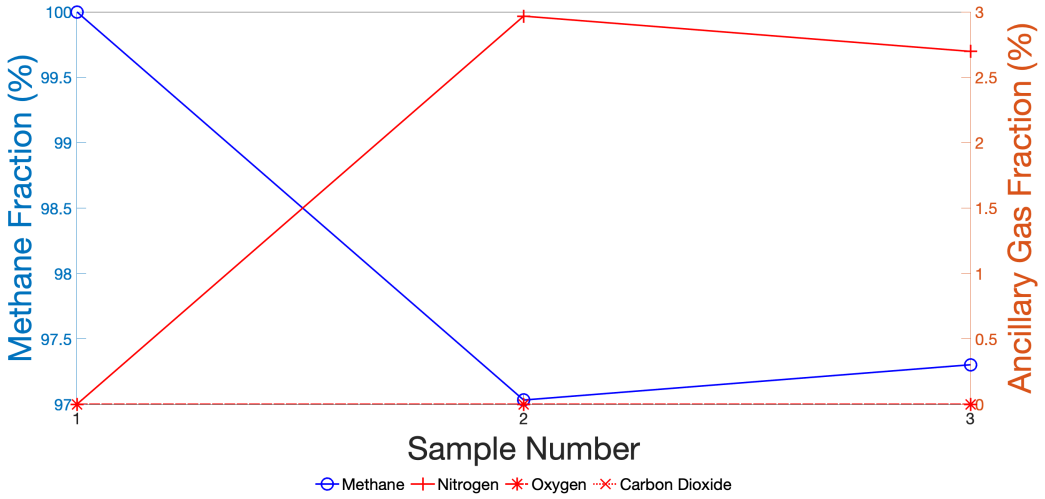

(d) Eldin's Bubbles 3 - Collection 1

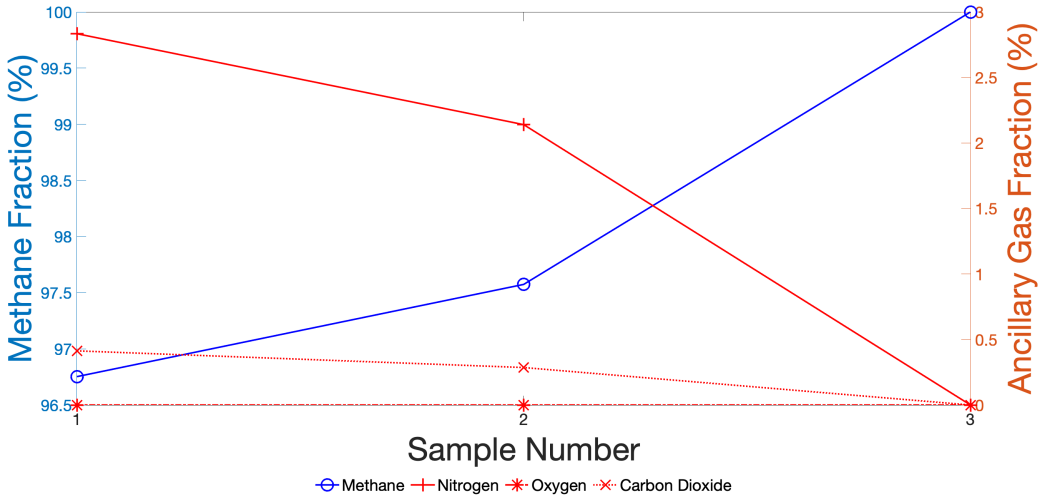

(e) Eldin's Bubbles 3 - Collection 2

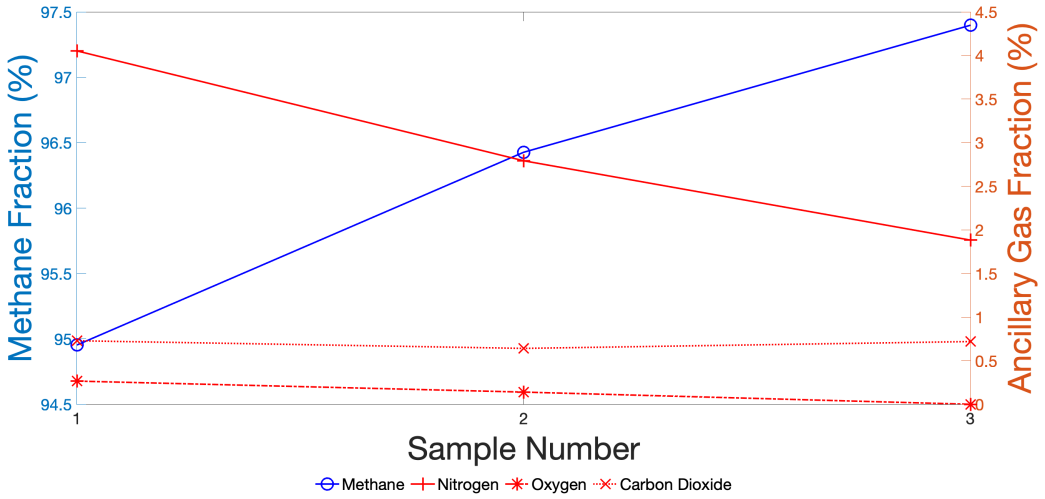

(f) Hester 1 - Collection 1

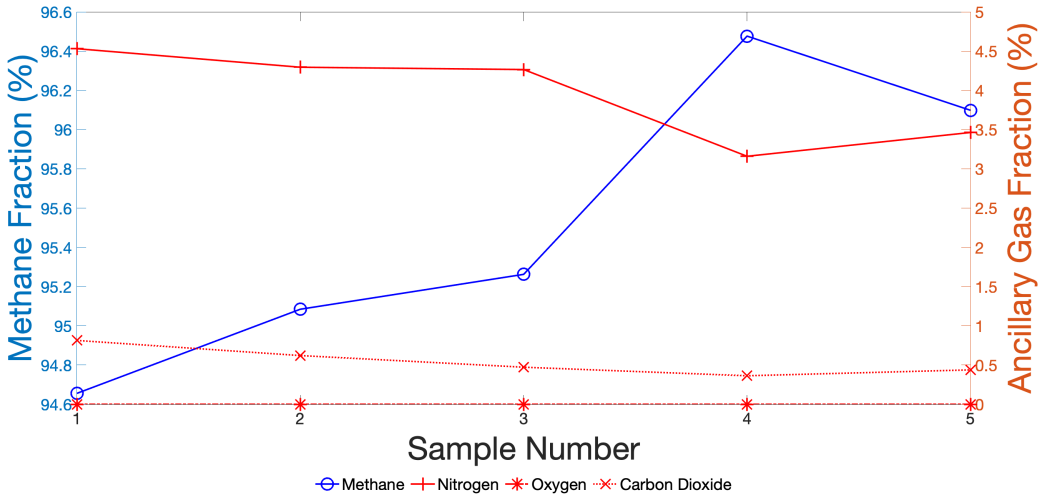

(g) Hester 1 - Collection 3

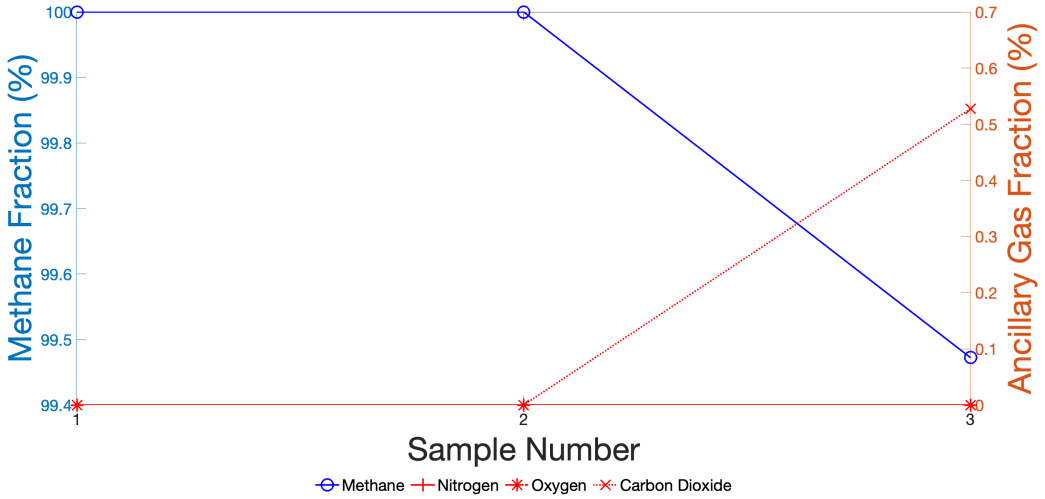

(h) Hester 2 - Collection 1

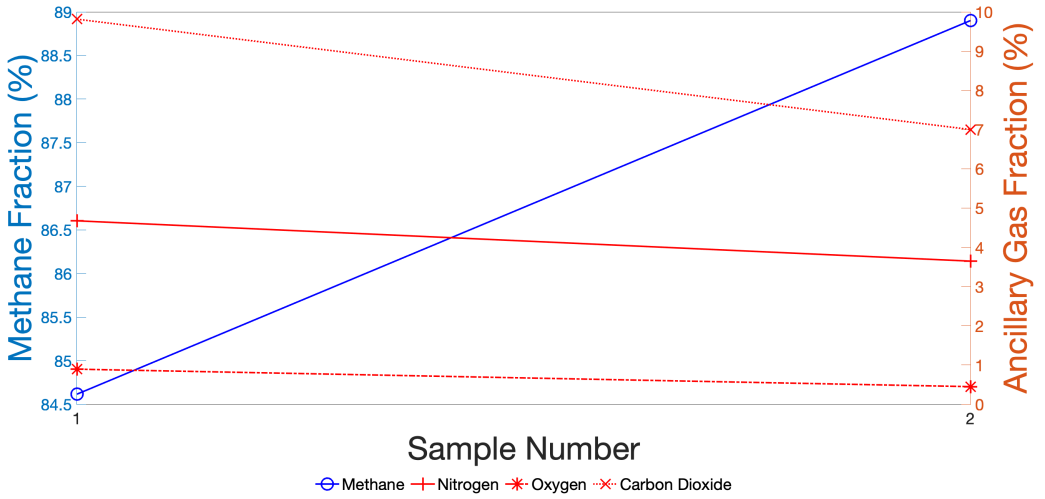

(i) Heceta Deep - Collection 1

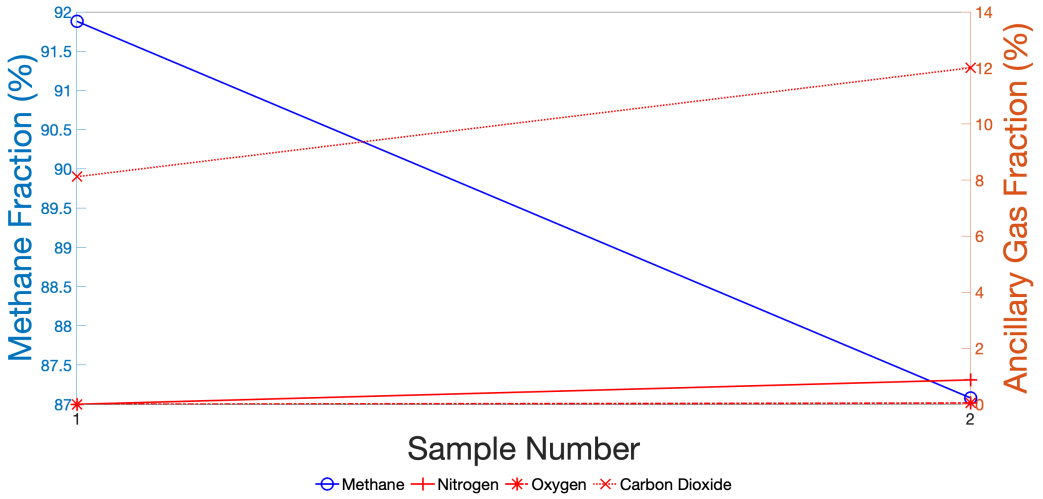

(j) Heceta Deep - Collection 4

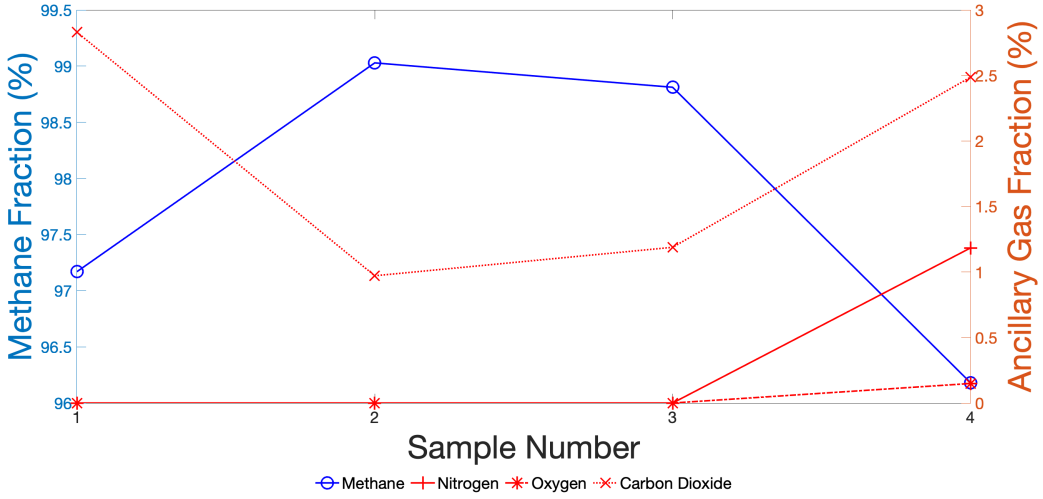

(k) Heceta Deep - Collection 5

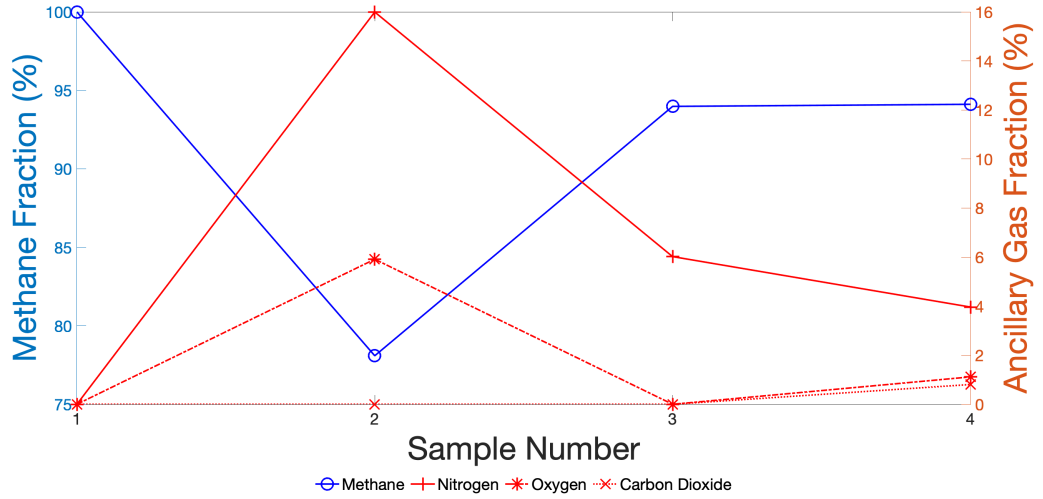

(l) Heceta Shallow - Collection 1

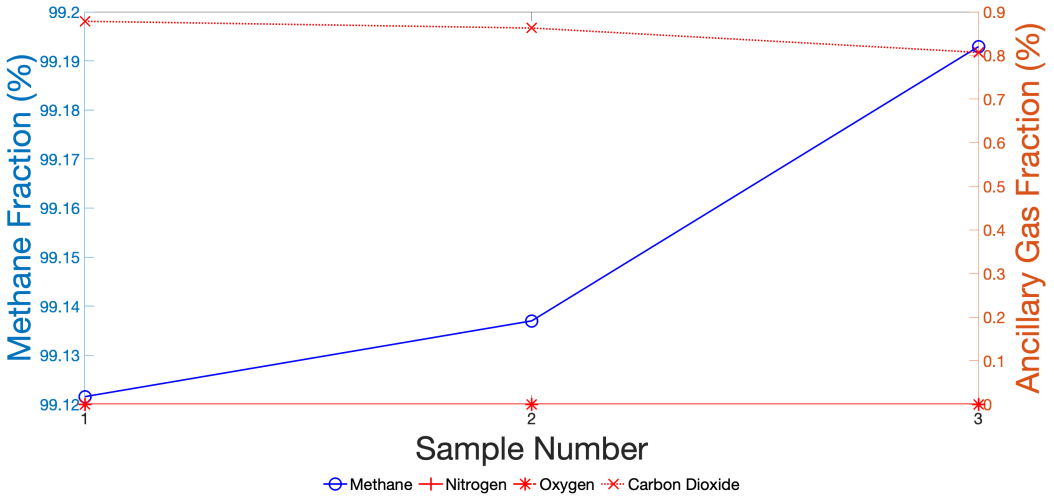

(m) Heceta Shallow - Collection 2

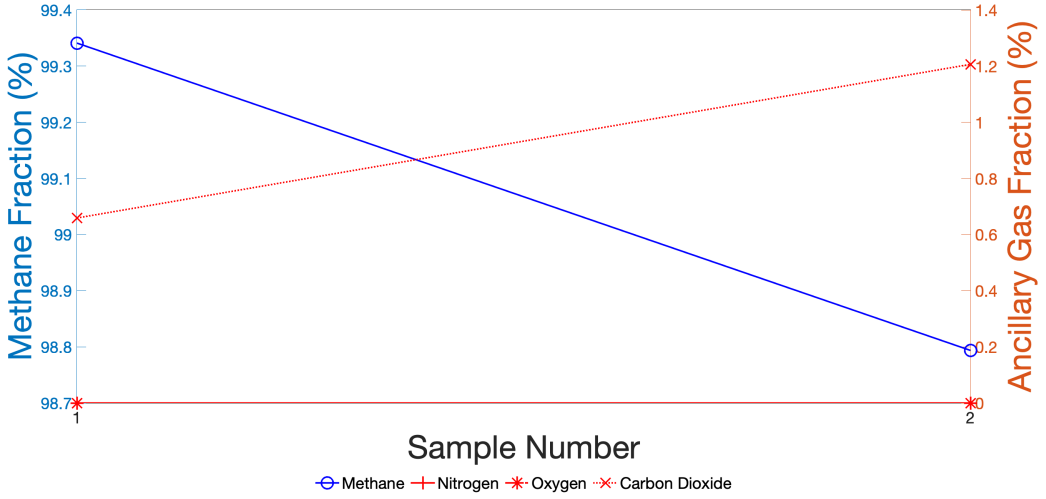

(n) Heceta Shallow - Collection 3

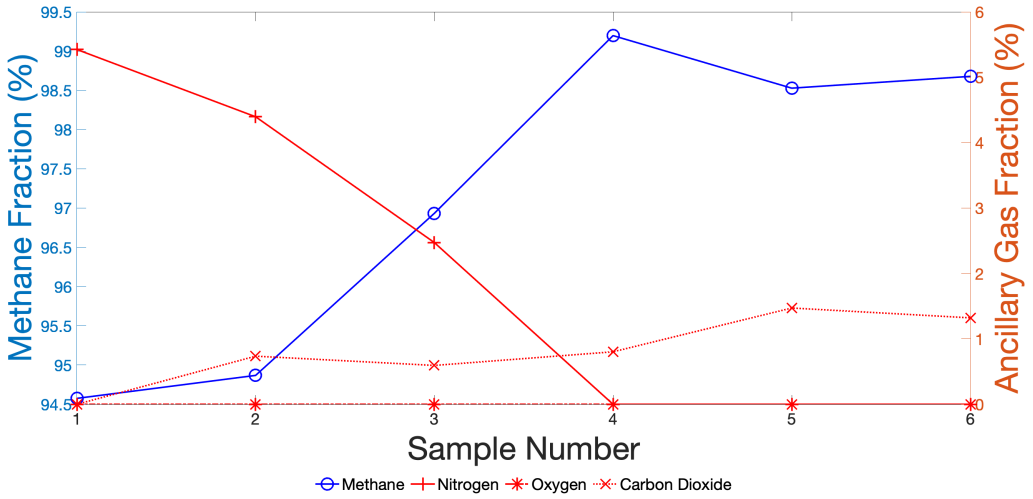

(o) Heceta Shallow - Collection 4

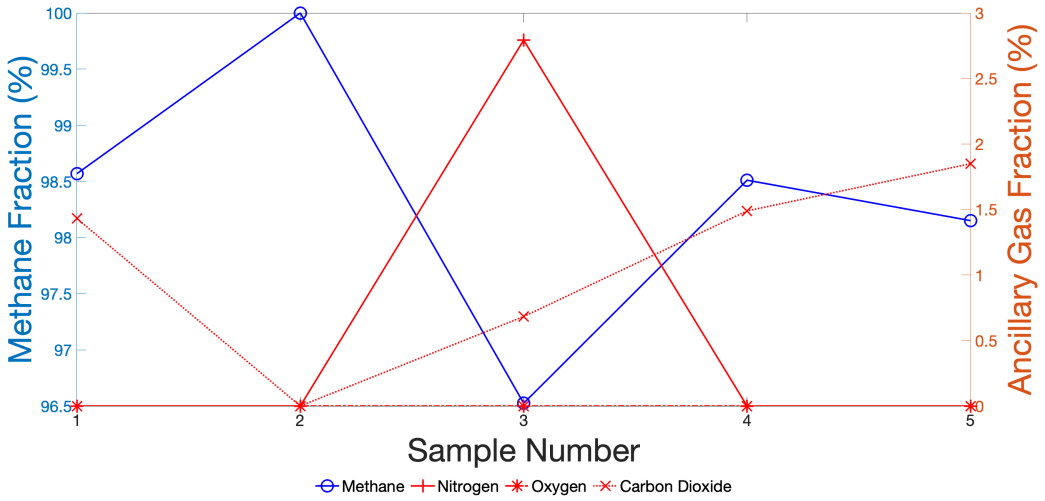

(p) Heceta Shallow - Collection 5

Figure B-1: Intercollection sample trends. Each figure shows the distribution of each gas's contribution to the sample composition in the collections that had more than one sample. CH_4 fraction is shown on the left axis in blue and the other gases (N_2, O_2 and CO_2) are shown in red and scaled on the right axis. Note that that the CH_4 fraction tends to increase with each subsequent sample while the other gas's contribution decrease. This phenomenon is discussed in more detail in Section 4.2.

Table B.1: List of sample depth, altitude, composition and ebullition rate. Ebullition rate is given in general terms where one dot is the least active and three dots is the most active.

McArthur Ridge	Eldin's Bubbles 1	EB1-1-1	832	1	6.0	0.5	0.3	93.2	○
		EB1-1-2	832	1	4.4	0.4	0.2	95.0	
		EB1-1-3	832	1	4.1	0.4	0.2	95.3	
		EB1-1-4	832	1	4.6	0.0	0.4	95.0	
		EB1-1-5	832	1	2.0	0.0	0.2	97.8	
		EB1-2-1	832	5	1.2	0.0	0.1	98.7	
		EB1-3-1	832	8	0.9	0.0	0.1	99.0	
	Eldin's bubbles 2	EB2-1-1	830	0.5	5.9	0.0	0.3	93.7	○ ○ ○
		EB2-1-2	830	0.5	4.7	0.0	0.3	94.9	
		EB2-1-3	830	0.5	4.8	0.0	0.2	94.9	
		EB2-2-1	830	0.5	5.0	0.4	0.2	94.5	
		EB2-2-2	830	0.5	4.1	0.3	0.3	95.3	
		EB2-3-1	830	3	5.2	0.3	0.2	94.4	
	Eldin's Bubbles 3	EB3-1-1	829	3	0.0	0.0	0.0	100.0	○ ○ ○
		EB3-1-2	829	3	3.0	0.0	0.0	97.0	
		EB3-1-3	829	3	2.7	0.0	0.0	97.3	
		EB3-2-1	829	6	2.8	0.0	0.4	96.8	
		EB3-2-2	829	6	2.1	0.0	0.3	97.6	

Table B.1 continued.

Site	Seep	Sample Id	Depth (m)	Altitude (m)	Fraction of Bubble (%)				Ebullition Rate
					CH_4	N_2	CO_2	O_2	
		EB3-2-3	829	6	0.0	0.0	0.0	100.0	
Heceta Bank	Hester 1	HES1-1-1	787	0.5	4.1	0.3	0.7	95.0	○○
		HES1-1-2	787	0.5	2.8	0.1	0.6	96.4	
		HES1-1-3	787	0.5	1.9	0.0	0.7	97.4	
		HES1-1-4	787	10	3.5	0.0	0.4	96.1	
		HES1-2-1	787	0.5	3.3	0.2	0.9	95.7	
		HES1-3-1	787	10	4.5	0.0	0.8	94.7	
		HES1-3-2	787	10	4.3	0.0	0.6	95.1	
		HES1-3-3	787	10	4.3	0.0	0.5	95.3	
		HES1-3-4	787	10	3.2	0.0	0.4	96.5	
	Hester 2	HES2-1-1	745	10	0.0	0.0	0.0	100.0	○○
		HES2-1-2	745	10	0.0	0.0	0.0	100.0	
		HES2-1-3	745	10	0.0	0.0	0.5	99.5	
Heceta Bank	Heceta Deep	HECD-1-1	489	0.5	4.7	0.9	9.8	84.6	○
		HECD-1-2	489	0.5	3.6	0.4	7.0	88.9	
		HECD-2-1	489	0.5	2.3	0.3	5.5	91.8	

Table B.1 continued.

Site	Seep	Sample Id	Depth (m)	Altitude (m)	Fraction of Bubble (%)				Ebullition Rate
					CH_4	N_2	CO_2	O_2	
		HECD-3-1	489	0.5	1.0	0.1	8.4	90.5	
		HECD-4-1	489	0.5	0.0	0.0	8.1	91.9	
		HECD-4-2	489	0.5	0.9	0.0	12.0	87.1	
		HECD-5-1	489	26	0.0	0.0	2.8	97.2	
		HECD-5-2	489	26	0.0	0.0	1.0	99.0	
		HECD-5-3	489	26	0.0	0.0	1.2	98.8	
		HECD-5-4	489	26	1.2	0.1	2.5	96.2	
	Heceta Shallow	HECS-1-1	115	0.5	0.0	0.0	0.0	100.0	○
		HECS-1-2	115	0.5	16.0	5.9	0.0	78.1	
		HECS-1-3	115	0.5	6.0	0.0	0.0	94.0	
		HECS-1-4	115	0.5	4.0	1.1	0.8	94.1	
		HECS-2-1	115	0.5	0.0	0.0	0.9	99.1	
		HECS-2-2	115	0.5	0.0	0.0	0.9	99.1	
		HECS-2-3	115	0.5	0.0	0.0	0.8	99.2	
		HECS-3-1	115	0.5	0.0	0.0	0.7	99.3	
		HECS-3-2	115	0.5	0.0	0.0	1.2	98.8	

Table B.1 continued.

Site	Seep	Sample Id	Depth (m)	Altitude (m)	Fraction of Bubble (%)				Ebullition Rate
					CH_4	N_2	CO_2	O_2	
		HECS-4-1	115	0.5	5.4	0.0	0.0	94.6	
		HECS-4-2	115	0.5	4.4	0.0	0.7	94.9	
		HECS-4-3	115	0.5	2.5	0.0	0.6	96.9	
		HECS-4-4	115	0.5	0.0	0.0	0.8	99.2	
		HECS-4-5	115	0.5	0.0	0.0	1.5	98.5	
		HECS-4-6	115	0.5	0.0	0.0	1.3	98.7	
		HECS-5-1	115	0.5	0.0	0.0	1.4	98.6	
		HECS-5-2	115	0.5	0.0	0.0	0.0	100.0	
		HECS-5-3	115	0.5	2.8	0.0	0.7	96.5	
		HECS-5-4	115	0.5	0.0	0.0	1.5	98.5	
		HECS-5-5	115	0.5	0.0	0.0	1.8	98.2	

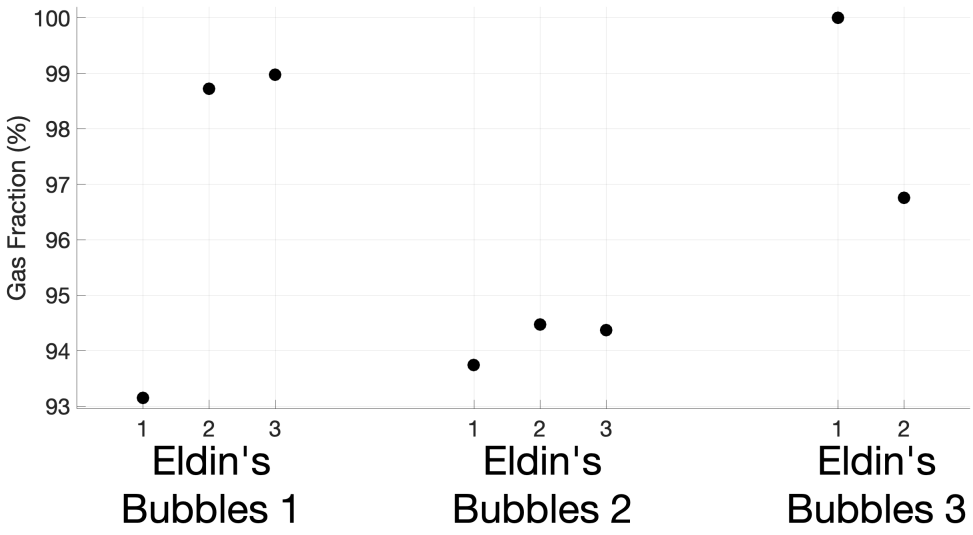

(a) McArthur Ridge

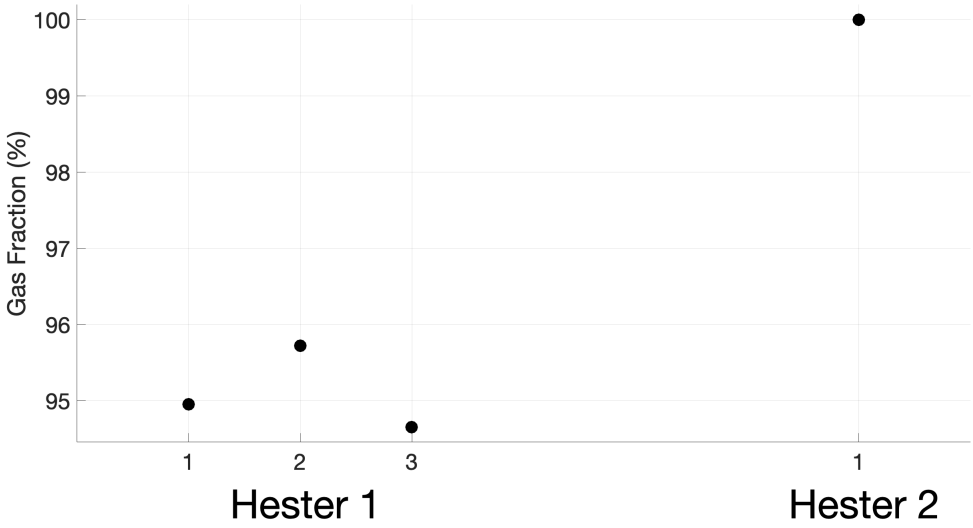

(b) Hydrate Ridge

Figure B-2: Scatter plots showing CH_4 fraction distribution by site. Sample number is shown on the x-axis.

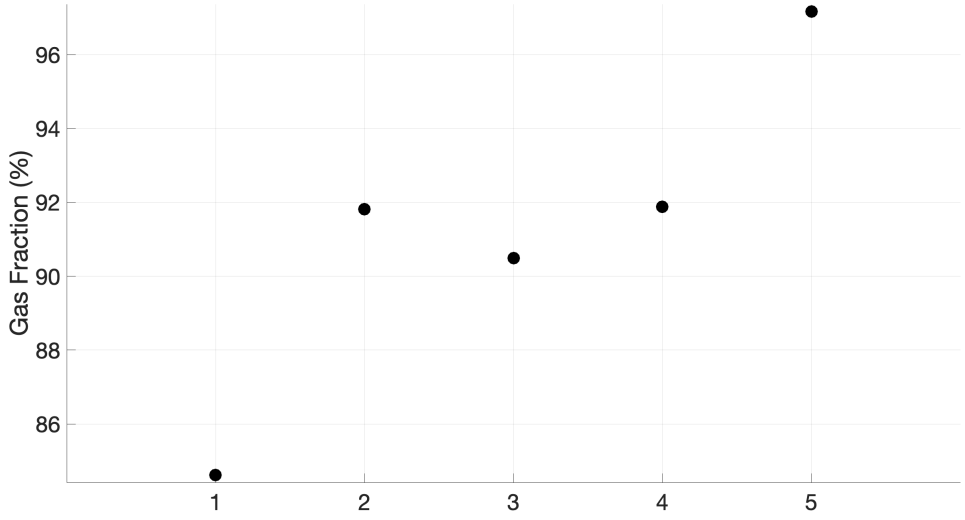

(c) Heceta Deep

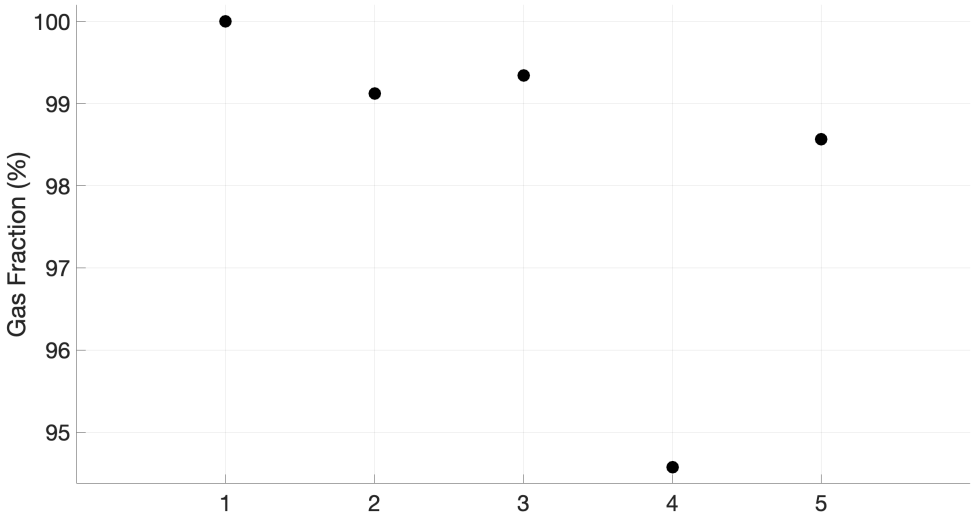

(d) Heceta Shallow

Figure B-2 continued

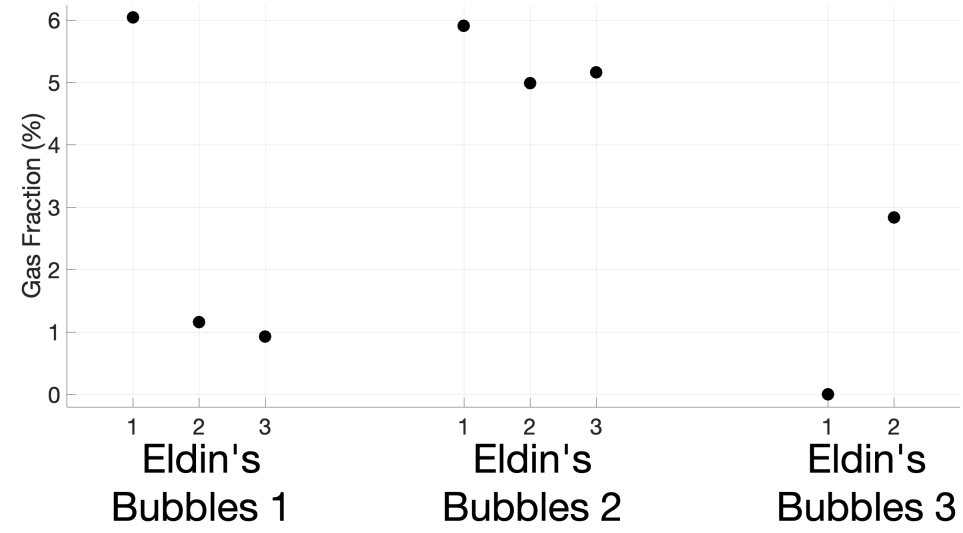

(a) McArthur Ridge

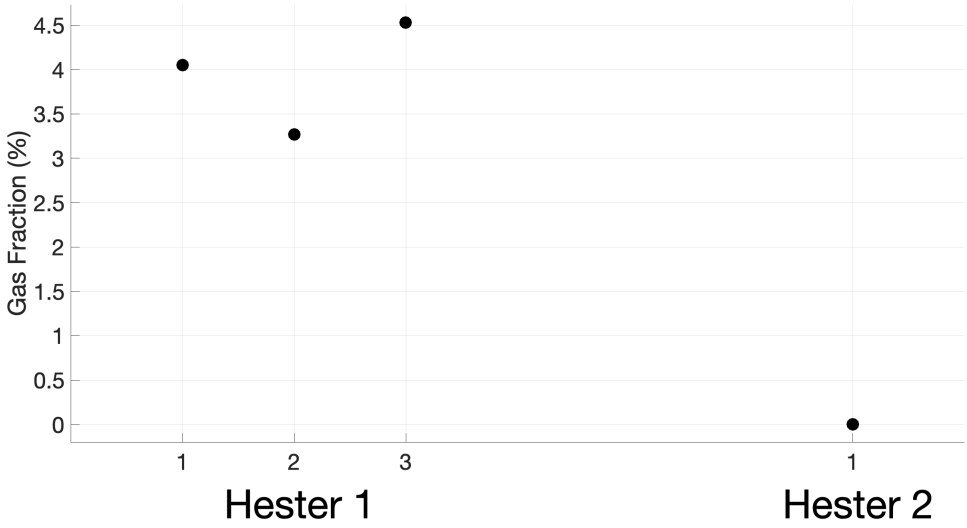

(b) Hydrate Ridge

Figure B-3: Scatter plots showing N_2 fraction distribution organized by site. Sample number is shown on the x-axis.

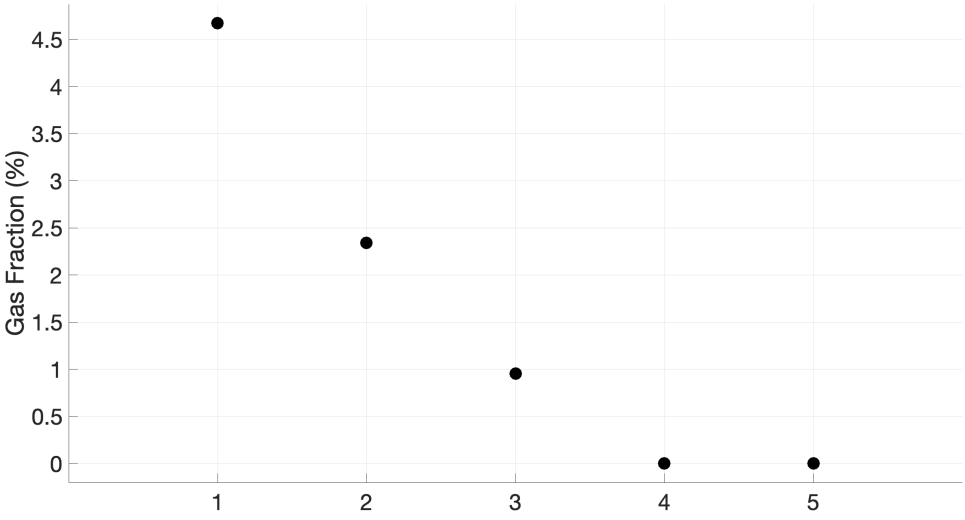

(c) Heceta Deep

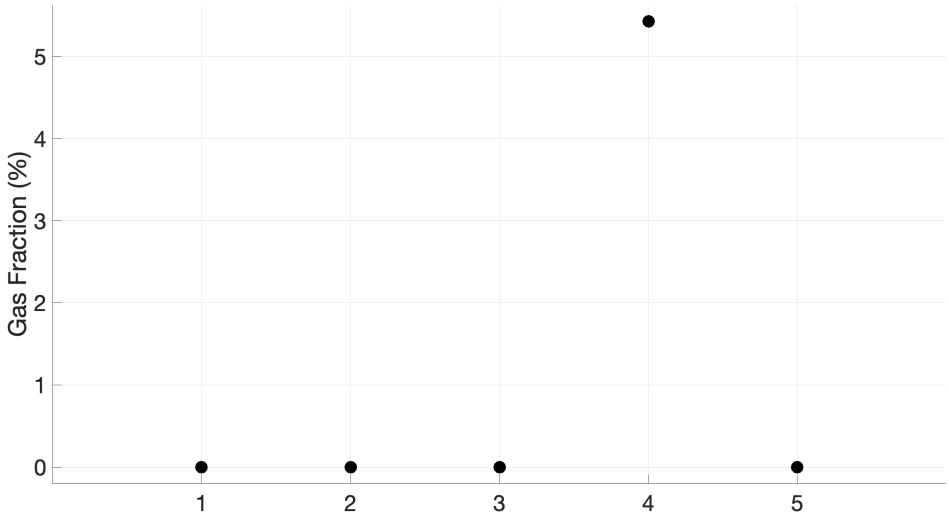

(d) Heceta Shallow

Figure B-3 continued.

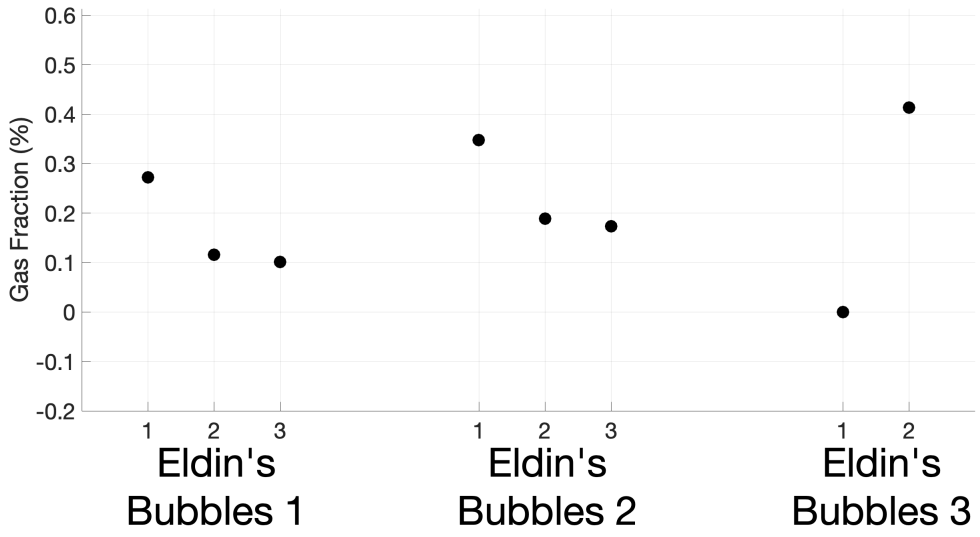

(a) McArthur Ridge

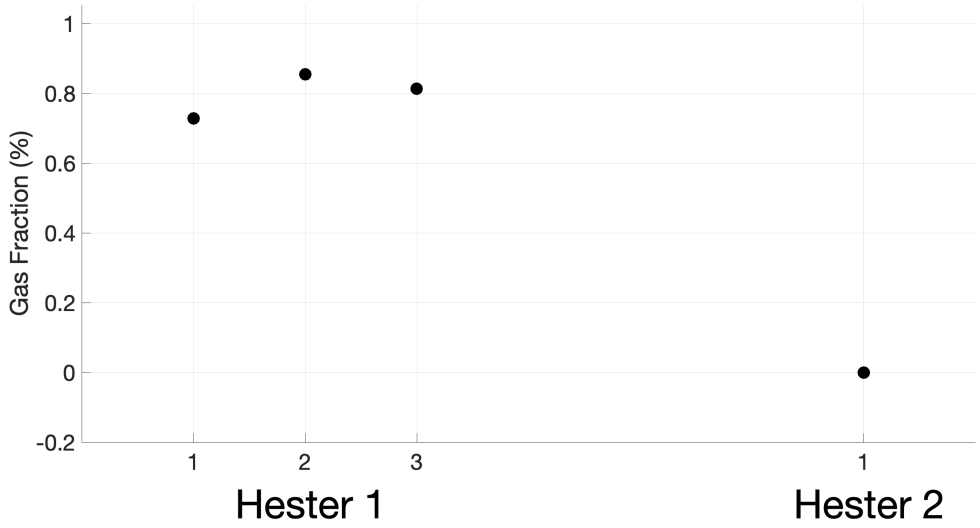

(b) Hydrate Ridge

Figure B-4: Scatter plots showing CO_2 fraction distribution organized by site. Sample number is shown on the x-axis.

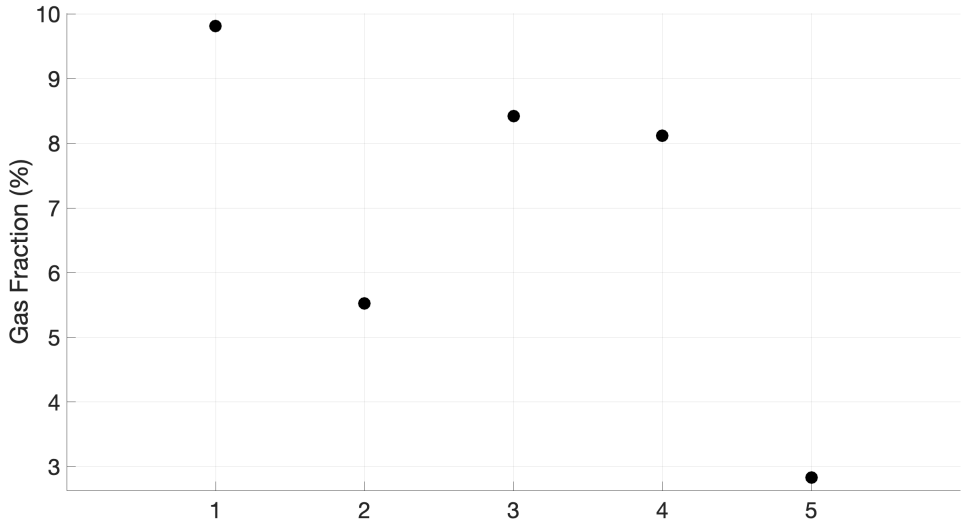

(c) Heceta Deep

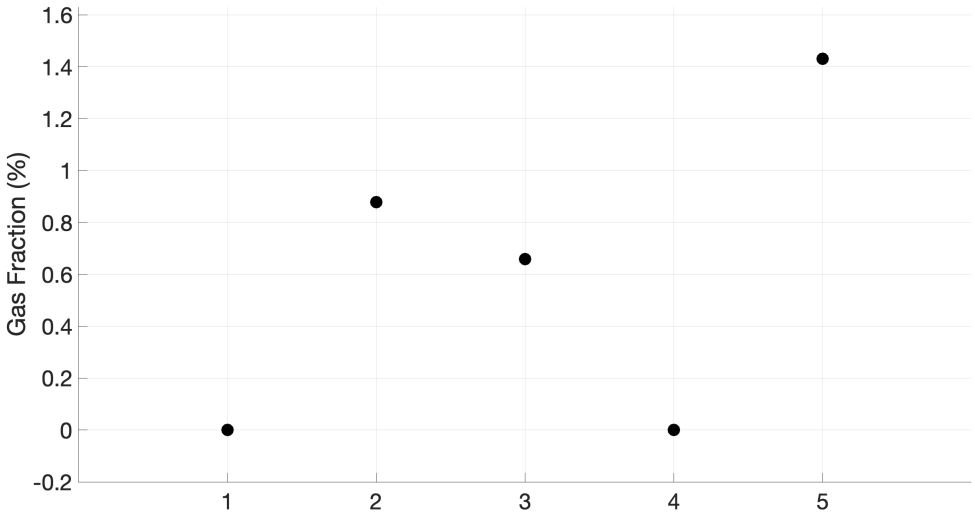

(d) Heceta Shallow

Figure B-4 continued.

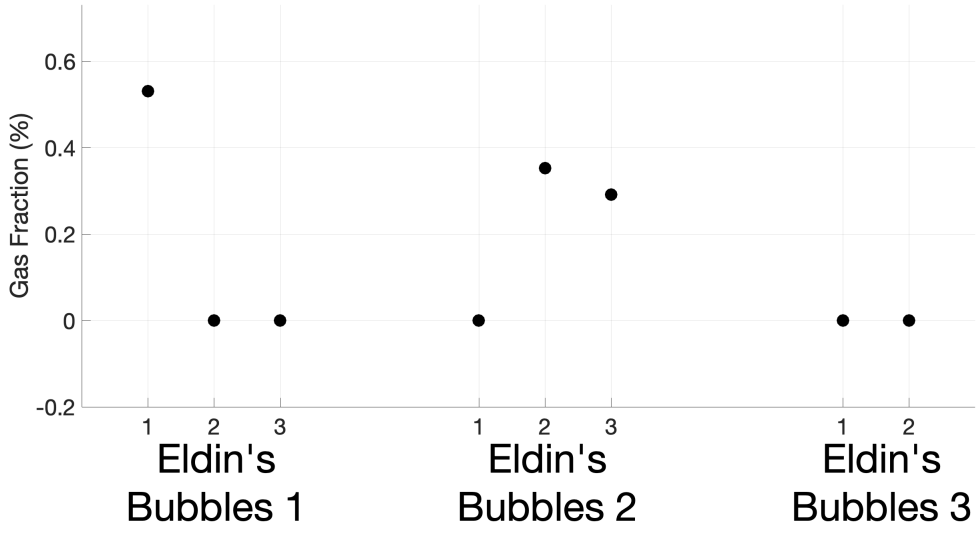

(a) McArthur Ridge

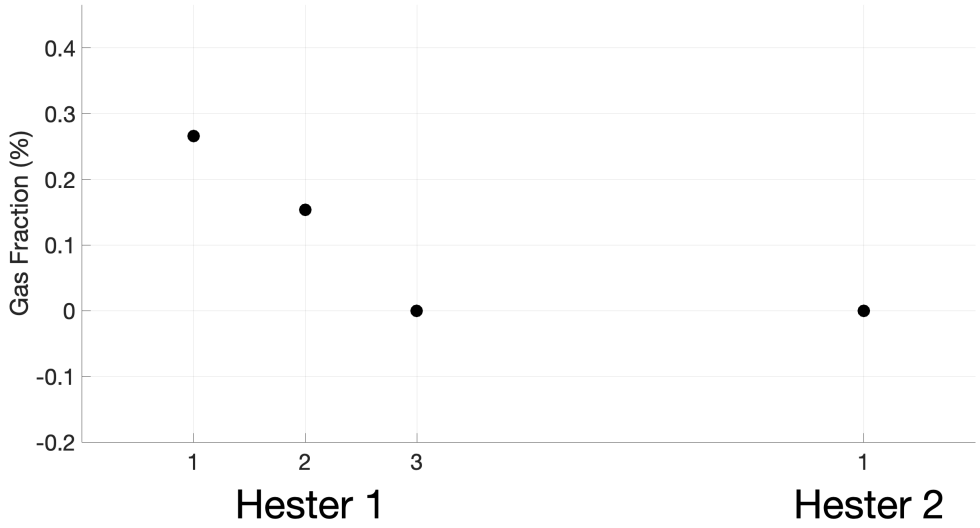

(b) Hydrate Ridge

Figure B-5: Scatter plots showing O_2 fraction distribution organized by site. Sample number is shown on the x-axis.

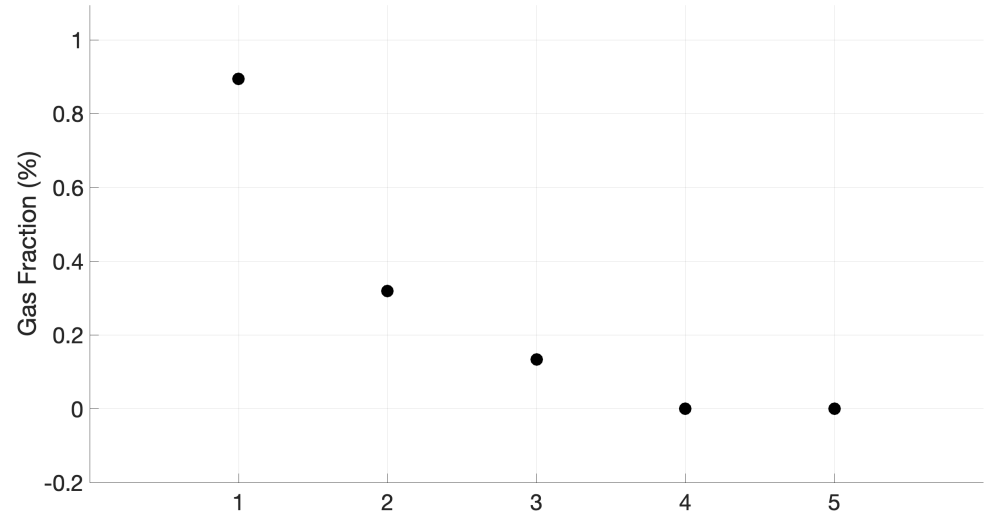

(c) Heceta Deep

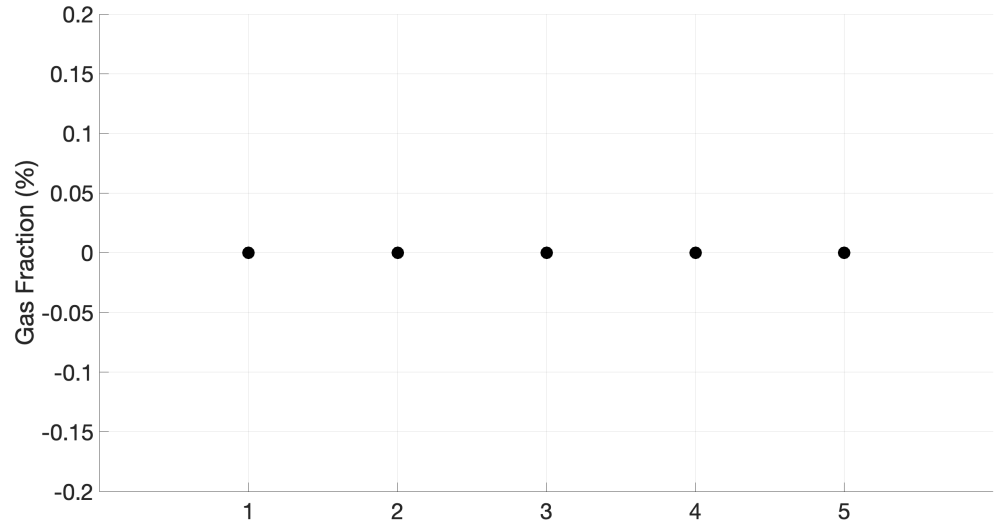

(d) Heceta Shallow

Figure B-5 continued

.

THIS PAGE INTENTIONALLY LEFT BLANK

Bibliography

[1] C. D. Ruppel and J. D. Kessler, "The interaction of Climate Change and Methane Hydrates," *Deep-Sea Research Part II: Topical Studies in Oceanography*, vol. 57, no. 1, pp. 1–20, 2016.

[2] W. S. Reeburgh, "Oceanic methane biogeochemistry," *American Chemical Society*, vol. 107, no. 2, pp. 486–513, 2007.

[3] A. M. Tréhu, C. D. Ruppel, M. Holland, G. Dickens, M. Torres, T. Collett, D. Goldberg, M. Riedel, and P. Schultheiss, "Gas Hydrates in Marine Sediments: Lessons from Scientific Ocean Drilling," *Oceanography*, vol. 19, no. 4, pp. 124–142, 2006.

[4] D. L. Valentine, "Emerging Topics in Marine Methane Biogeochemistry," *Annual Review of Marine Science*, vol. 3, no. 1, pp. 147–171, 2011.

[5] IPCC, *Climate Change 2013: The Physical Science Basis. Contribution of Working Group I to the Fifth Assessment Report of the Intergovernmental Panel on Climate Change*. Cambridge, United Kingdom and New York, NY, USA: Cambridge University Press, 2013.

[6] D. Archer, "Methane hydrate stability and anthropogenic climate change," *Biogeosciences*, vol. 4, no. 4, pp. 521–544, 2007.

[7] T. Parsons, A. M. Trehu, J. H. Luetgert, K. Miller, F. Kilbride, R. E. Wells, M. A. Fisher, E. Flueh, U. S. Ten Brink, and N. I. Christensen, "A new view into the Cascadia subduction zone and volcanic arc: Implications for earthquake hazards along the Washington margin," *Geology*, vol. 26, no. 3, pp. 199–202, 1998.

[8] E. D. Sloan and C. A. Koh, *Clathrates Hydrates of the Natural Gases*. Boca Ratton: CRC Press, 2008.

[9] G. J. MacDonald, "Role of methane clathrates in past and future climates," *Climatic Change*, vol. 16, no. 3, pp. 247–281, 1990.

[10] A. M. Tréhu, P. B. Flemings, N. L. Bangs, J. Chevallier, E. Gràcia, J. E. Johnson, C. S. Liu, X. Liu, M. Riedel, and M. E. Torres, "Feeding methane vents and gas hydrate deposits at south Hydrate Ridge," *Geophysical Research Letters*, vol. 31, no. 23, pp. 1–4, 2004.

[11] A. M. Tréhu, P. E. Long, M. E. Torres, G. Bohrmann, F. R. Rack, T. S. Collett, D. S. Goldberg, A. V. Milkov, M. Riedel, P. Schultheiss, N. L. Bangs, S. R. Barr, W. S. Borowski, G. E. Claypool, M. E. Delwiche, G. R. Dickens, E. Gracia, G. Guerin,

M. Holland, J. E. Johnson, Y. J. Lee, C. S. Liu, X. Su, B. Teichert, H. Tomaru, M. Vanneste, M. Watanabe, and J. L. Weinberger, "Three-dimensional distribution of gas hydrate beneath southern Hydrate Ridge: Constraints from ODP Leg 204," *Earth and Planetary Science Letters*, vol. 222, no. 3-4, pp. 845–862, 2004.

[12] J. Kessler, "Seafloor methane: Atlantic bubble bath," *Nature Geoscience*, vol. 7, no. 9, pp. 625–626, 2014.

[13] V. Krey, J. G. Canadell, N. Nakicenovic, Y. Abe, H. Andruleit, D. Archer, A. Grubler, N. T. Hamilton, A. Johnson, V. Kostov, J. F. Lamarque, N. Langhorne, E. G. Nisbet, B. O'Neill, K. Riahi, M. Riedel, W. Wang, and V. Yakushev, "Gas hydrates: Entrance to a methane age or climate threat?," *Environmental Research Letters*, vol. 4, no. 3, 2009.

[14] J. Bohannon, "Energy: Weighing the climate risks of an untapped fossil fuel," *Science*, vol. 319, no. 5871, p. 1753, 2008.

[15] A. Mascarelli, "A sleeping giant?," *Nature Reports Climate Change*, p. 46, mar 2009.

[16] S. L. Hautala, E. A. Solomon, H. P. Johnson, R. N. Harris, and U. K. Miller, "Dissociation of Cascadia margin gas hydrates in response to contemporary ocean warming," *Geophysical Research Letters*, vol. 41, pp. 8486–8494, 2014.

[17] G. R. Dickens, J. R. O. Neil, D. K. Rea, and R. M. Owen, "That Bottom Water Temperature Increased By More Than During a Brief Time Interval," *Paleoceanographic Currents*, vol. 10, no. 6, pp. 965–971, 1995.

[18] K. U. Hinrichs, L. R. Hmelo, and S. P. Sylva, "Molecular fossil record of elevated methane levels in late Pleistocene coastal waters," *Science*, vol. 299, no. 5610, pp. 1214–1217, 2003.

[19] M. J. Whiticar, "Carbon and hydrogen isotope systematics of bacterial formation and oxidation of methane," *Chemical Geology*, vol. 161, no. 1, pp. 291–314, 1999.

[20] G. D. Floodgate and A. G. Judd, "The origins of shallow gas," *Continental Shelf Research*, vol. 12, no. 10, pp. 1145–1156, 1992.

[21] M. Leonte, B. Wang, S. A. Socolofsky, S. Mau, J. A. Breier, and J. D. Kessler, "Using Carbon Isotope Fractionation to Constrain the Extent of Methane Dissolution Into the Water Column Surrounding a Natural Hydrocarbon Gas Seep in the Northern Gulf of Mexico," *Geochemistry, Geophysics, Geosystems*, vol. 19, no. 11, pp. 4459–4475, 2018.

[22] T. Pape, A. Bahr, J. Rethemeyer, J. D. Kessler, H. Sahling, K. U. Hinrichs, S. A. Klapp, W. S. Reeburgh, and G. Bohrmann, "Molecular and isotopic partitioning of low-molecular-weight hydrocarbons during migration and gas hydrate precipitation in deposits of a high-flux seepage site," *Chemical Geology*, vol. 269, no. 3-4, pp. 350–363, 2010.

[23] J. S. Booth, M. M. Rowe, and K. M. Fischer, "Offshore gas hydrate sample database: With an overview and preliminary analysis," tech. rep., United States Geologic Society, Woods Hole, 1996.

[24] W. S. Reeburgh, "Rates of Biogeochemical Processes in Anoxic Sediments," *Annual Review of Earth and Plantary Science*, vol. 11, p. 2, 1982.

[25] M. K. Davie and B. A. Buffett, "A steady state model for marine hydrate formation: Constraints on methane supply from pore water sulfate profiles," *Journal of Geophysical Research: Solid Earth*, vol. 108, no. B10, pp. 1–13, 2003.

[26] A. J. Smith, J. Mienert, S. Bünz, and J. Greinert, "Thermogenic methane injection via bubble transport into the upper Arctic Ocean from the hydrate-charged Vestnesa Ridge, Svalbard," *Geochemistry, Geophysics, Geosystems*, vol. 15, no. 5, pp. 1945–1959, 2014.

[27] N. L. Bangs, M. J. Hornbach, and C. Berndt, "The mechanics of intermittent methane venting at South Hydrate Ridge inferred from 4D seismic surveying," *Earth and Planetary Science Letters*, vol. 310, no. 1-2, pp. 105–112, 2011.

[28] M. Riedel, M. Scherwath, M. Römer, M. Veloso, M. Heesemann, and G. D. Spence, "Distributed natural gas venting offshore along the Cascadia margin," *Nature Communications*, vol. 9, no. 1, p. 3264, 2018.

[29] M. Römer, M. Riedel, M. Scherwath, M. Heesemann, and G. D. Spence, "Tidally controlled gas bubble emissions: A comprehensive study using long-term monitoring data from the NEPTUNE cabled observatory offshore Vancouver Island," *Geochemistry, Geophysics, Geosystems*, vol. 17, pp. 3797–3814, sep 2016.

[30] S. Mau, T. Gentz, J. H. Körber, M. E. Torres, M. Römer, H. Sahling, P. Wintersteller, R. Martinez, M. Schlüter, and E. Helmke, "Seasonal methane accumulation and release from a gas emission site in the central North Sea," *Biogeosciences*, vol. 12, no. 18, pp. 5261–5276, 2015.

[31] A. Skarke, C. D. Ruppel, M. Kodis, D. Brothers, and E. Lobecker, "Widespread methane leakage from the sea floor on the northern US Atlantic margin," *Nature Geoscience*, vol. 7, no. 9, pp. 657–661, 2014.

[32] J. D. Kessler, W. S. Reeburgh, J. Southon, and R. Varela, "Fossil methane source dominates Cariaco Basin water column methane geochemistry," *Geophysical Research Letters*, vol. 32, no. 12, pp. 1–4, 2005.

[33] B. Alpar, "Underwater Signatures of the Kocaeli Earthquake (August 17th 1999) 17 Agustos 1999 Kocaeli Depreminin Deniz Tabam ve Giincel < ; okeller Uzerindeki Etkileri," *Turkish Journal of Marine Sciences*, vol. 5, no. 3, pp. 111–130, 1999.

[34] I. KuÅ§çu, M. Okamura, H. Matsuoka, and Y. Awata, "Active faults in the Gulf of Ärzmit on the North Anatolian Fault, NW Turkey: A high-resolution shallow seismic study," *Marine Geology*, vol. 190, no. 1-2, pp. 421–443, 2002.

[35] I. KuÅ§çu, M. Okamura, H. Matsuoka, E. GökaÅ§an, Y. Awata, H. Tur, M. ÅđimÅ§ek, and M. Keçer, "Seafloor gas seeps and sediment failures triggered by the August 17, 1999 earthquake in the Eastern part of the Gulf of Ärzmit, Sea of Marmara, NW Turkey," *Marine Geology*, vol. 215, no. 3-4, pp. 193–214, 2005.

[36] G. Bayrakci, C. Scalabrin, S. Dupré, I. Leblond, J. B. Tary, N. Lanteri, J. M. Augustin, L. Berger, E. Cros, A. Ogor, C. Tsabaris, M. Lescanne, and L. Géli, "Acoustic monitoring of gas emissions from the seafloor. Part II: a case study from the Sea of Marmara," *Marine Geophysical Research*, vol. 35, no. 3, pp. 211–229, 2014.

[37] M. E. Field and A. E. Jennings, "Seafloor gas seeps triggered by a northern California earthquake," *Marine Geology*, vol. 77, no. 1-2, pp. 39–51, 1987.

[38] A. Obzhirov, R. Shakirov, A. Salyuk, E. Suess, N. Biebow, and A. Salomatin, "Relations between methane venting, geological structure and seismo-tectonics in the Okhotsk Sea," *Geo-Marine Letters*, vol. 24, no. 3, pp. 135–139, 2004.

[39] S. Mau, D. L. Valentine, J. F. Clark, J. Reed, R. Camilli, and L. Washburn, "Dissolved methane distributions and air-sea flux in the plume of a massive seep field, Coal Oil Point, California," *Geophysical Research Letters*, vol. 34, no. 22, pp. 2–6, 2007.

[40] L. Lapham, R. Wilson, M. Riedel, C. K. Paull, and M. E. Holmes, "Temporal variability of in situ methane concentrations in gas hydrate-bearing sediments near Bullseye Vent, Northern Cascadia Margin," *Geochemistry, Geophysics, Geosystems*, vol. 14, no. 7, pp. 2445–2459, 2013.

[41] L. L. Lapham, J. P. Chanton, C. S. Martens, P. D. Higley, H. W. Jannasch, and J. R. Woolsey, "Measuring temporal variability in pore-fluid chemistry to assess gas hydrate stability: Development of a continuous pore-fluid array," *Environmental Science and Technology*, vol. 42, no. 19, pp. 7368–7373, 2008.

[42] M. D. Tryon, K. M. Brown, M. E. Torres, A. M. Tréhu, J. McManus, and R. W. Collier, "Measurements of transience and downward fluid flow near episodic methane gas vents, Hydrate Ridge, Cascadia," *Geology*, vol. 27, no. 12, pp. 1075–1078, 1999.

[43] H. Daigle, N. L. Bangs, and B. Dugan, "Transient hydraulic fracturing and gas release in methane hydrate settings: A case study from southern Hydrate Ridge," *Geochemistry, Geophysics, Geosystems*, vol. 12, no. 12, pp. 1–15, 2011.

[44] M. Riedel, I. Novosel, G. D. Spence, R. D. Hyndman, R. N. Chapman, R. C. Solem, and T. Lewis, "Geophysical and geochemical signatures associated with gas hydrate-related venting in the northern Cascadia margin," *Bulletin of the Geological Society of America*, vol. 118, no. 1-2, pp. 23–38, 2006.

[45] E. Suess, M. E. Torres, G. Bohrmann, R. W. Collier, J. Greinert, P. Linke, G. Rehder, A. Trehu, K. Wallmann, G. Winckler, and E. Zuleger, "Gas hydrate destabilization: Enhanced dewatering, benthic material turnover and large methane plumes at the Cascadia convergent margin," *Earth and Planetary Science Letters*, vol. 170, no. 1-2, pp. 1–15, 1999.

[46] M. E. Torres, J. Mcmanus, D. Hammond, M. de Angelis, K. Heeschen, S. Colbert, M. Tryon, K. Brown, and E. Suess, "Fluid and chemical flux in and out of sediments hosting methane hydrate deposits on Hydrate Ridge, OR, I: Hydrological processes," *Earth and Planetary Science Letters*, vol. 201, no. 3-4, pp. 541–557, 2002.

[47] J. R. Boles, J. F. Clark, I. Leifer, and L. Washburn, "Temporal variation in natural methane seep rate due to tides, Coal Oil Point area, California," *Journal of Geophysical Research*, vol. 106, no. C11, pp. 27077 – 27086, 2001.

[48] S. K. Hsu, S. Y. Wang, Y. C. Liao, T. F. Yang, S. Jan, J. Y. Lin, and S. C. Chen, "Tide-modulated gas emissions and tremors off SW Taiwan," *Earth and Planetary Science Letters*, vol. 369-370, pp. 98–107, 2013.

[49] I. Leifer and J. Boles, "Turbine tent measurements of marine hydrocarbon seeps on subhourly timescales," *Journal of Geophysical Research: Oceans*, vol. 110, no. 1, pp. 1–12, 2005.

[50] A. Krabbenhoeft, G. L. Netzeband, J. Bialas, and C. Papenberg, "Episodic methane concentrations at seep sites on the upper slope Opouawe Bank, southern Hikurangi Margin, New Zealand," *Marine Geology*, vol. 272, no. 1-4, pp. 71–78, 2010.

[51] C. Johansen, A. C. Todd, and I. R. MacDonald, "Time series video analysis of bubble release processes at natural hydrocarbon seeps in the Northern Gulf of Mexico," *Marine and Petroleum Geology*, vol. 82, pp. 21–34, 2017.

[52] B. P. Scandella, C. Varadharajan, H. F. Hemond, C. D. Ruppel, and R. Juanes, "A conduit dilation model of methane venting from lake sediments," *Geophysical Research Letters*, vol. 38, no. 6, pp. 1–6, 2011.

[53] P. K. Kannberg, A. M. Tré Hu, S. D. Pierce, C. K. Paull, and D. W. Caress, "Temporal variation of methane flares in the ocean above Hydrate Ridge, Oregon," *Earth and Planetary Science Letters*, vol. 368, pp. 33–42, 2013.

[54] J. F. Clark, L. Washburn, and K. S. Emery, "Variability of gas composition and flux intensity in natural marine hydrocarbon seeps," *Geo-Marine Letters*, vol. 30, no. 3-4, pp. 379–388, 2010.

[55] I. Leifer and R. K. Patro, "The bubble mechanism for methane transport from the shallow sea bed to the surface: A review and sensitivity study," *Continental Shelf Research*, vol. 22, no. 16, pp. 2409–2428, 2002.

[56] K. U. Heeschen, A. M. Tréhu, R. W. Collier, E. Suess, and G. Rehder, "Distribution and height of methane bubble plumes on the Cascadia margin characterized by acoustic imaging," *Geophysical Research Letters*, vol. 30, no. 12, pp. 1–4, 2003.

[57] G. Rehder, I. Leifer, P. G. Brewer, G. Friederich, and E. T. Peltzer, "Controls on methane bubble dissolution inside and outside the hydrate stability field from open ocean field experiments and numerical modeling," *Marine Chemistry*, vol. 114, no. 1-2, pp. 19–30, 2009.

[58] B. T. Philip, A. R. Denny, E. A. Solomon, and D. S. Kelley, "Time-series measurements of bubble plume variability and water column methane distribution above Southern Hydrate Ridge, Oregon," *Geochemistry, Geophysics, Geosystems*, vol. 17, no. 3, pp. 1182–1196, 2016.

[59] G. Rehder, P. W. Brewer, E. T. Peltzer, and G. Friederich, "Enhanced lifetime of methane bubble streams within the deep ocean," *Geophysical Research Letters*, vol. 29, no. 15, pp. 21–1–21–4, 2002.

[60] S. M. Wiggins, I. Leifer, P. Linke, and J. A. Hildebrand, "Long-term acoustic monitoring at North Sea well site 22/4b," *Marine and Petroleum Geology*, vol. 68, pp. 776–788, 2015.

[61] I. Leifer, "Characteristics and scaling of bubble plumes from marine hydrocarbon seepage in the coal oil point seep field," *Journal of Geophysical Research: Oceans*, vol. 115, no. 11, pp. 1–20, 2010.

[62] S. Vagle, J. Hume, F. McLaughlin, E. MacIsaac, and K. Shortreed, "A methane bubble curtain in meromictic Sakinaw Lake, British Columbia," *Limnology and Oceanography*, vol. 55, no. 3, pp. 1313–1326, 2010.

[63] J. S. von Deimling, J. Greinert, N. R. Chapman, W. Rabbel, and P. Linke, "Acoustic imaging of natural gas seepage in the North Sea: Sensing bubbles controlled by variable currents," *Limnology and Oceanography: Methods*, vol. 8, no. MAY, pp. 155–171, 2010.

[64] B. T. Philip, D. S. Kelley, E. A. Solomon, and J. R. Delaney, "Monitoring methane emissions at Southern Hydrate Ridge using an OOI Cabled Array Acoustic Doppler Current Profiler," *OCEANS 2016 MTS/IEEE Monterey, OCE 2016*, pp. 0–4, 2016.

[65] D. F. McGinnis, J. Greinert, Y. Artemov, S. E. Beaubien, and A. Wüest, "Fate of rising methane bubbles in stratified waters: How much methane reaches the atmosphere?," *Journal of Geophysical Research: Oceans*, vol. 111, no. 9, pp. 1–15, 2006.

[66] B. Wang and S. A. Socolofsky, "A deep-sea, high-speed, stereoscopic imaging system for in situ measurement of natural seep bubble and droplet characteristics," *Deep-Sea Research Part I: Oceanographic Research Papers*, vol. 104, pp. 134–148, 2015.

[67] K. Thomanek, O. Zielinski, H. Sahling, and G. Bohrmann, "Automated gas bubble imaging at sea floor - A new method of in situ gas flux quantification," *Ocean Science*, vol. 6, no. 2, pp. 549–562, 2010.

[68] I. Leifer and D. Culling, "Formation of seep bubble plumes in the Coal Oil Point seep field," *Geo-Marine Letters*, vol. 30, no. 3-4, pp. 339–353, 2010.

[69] J. Gros, C. M. Reddy, R. K. Nelson, S. A. Socolofsky, and J. S. Arey, "Simulating gas-liquid-water partitioning and fluid properties of petroleum under pressure: Implications for deep-sea blowouts," *Environmental Science and Technology*, vol. 50, no. 14, pp. 7397–7408, 2016.

[70] J. Gros, S. A. Socolofsky, A. L. Dissanayake, I. Jun, L. Zhao, M. C. Boufadel, C. M. Reddy, and J. S. Arey, " Petroleum dynamics in the sea and influence of subsea dispersant injection during Deepwater Horizon ," *Proceedings of the National Academy of Sciences*, vol. 114, no. 38, pp. 10065–10070, 2017.

[71] T. Baumberger, R. W. Embley, S. G. Merle, M. D. Lilley, N. A. Raineault, and J. E. Lupton, "Mantle-Derived Helium and Multiple Methane Sources in Gas Bubbles of Cold Seeps Along the Cascadia Continental Margin," *Geochemistry, Geophysics, Geosystems*, vol. 19, no. 11, pp. 4476–4486, 2018.

[72] A. P. Michel, S. D. Wankel, J. Kapit, Z. Sandwith, and P. R. Girguis, "In situ carbon isotopic exploration of an active submarine volcano," *Deep-Sea Research Part II: Topical Studies in Oceanography*, vol. 150, pp. 57–66, 2018.

[73] S. D. Wankel, S. B. Joye, V. A. Samarkin, S. R. Shah, G. Friederich, J. Melas-Kyriazi, and P. R. Girguis, "New constraints on methane fluxes and rates of anaerobic methane

oxidation in a Gulf of Mexico brine pool via in situ mass spectrometry," *Deep-Sea Research Part II: Topical Studies in Oceanography*, vol. 57, no. 21-23, pp. 2022–2029, 2010.

[74] H. Gholizadeh, R. Burton, and G. Schoenau, "Fluid bulk modulus: A literature survey," *International Journal of Fluid Power*, vol. 12, no. 3, pp. 5–15, 2011.

[75] Valco Instruments Company, Inc., "Materials of Construction," 2018.

[76] S.-L. Li, C.-Y. Sun, G.-J. Chen, Z.-Y. Li, Q.-L. Ma, L.-Y. Yang, and A. K. Sum, "Measurements of hydrate film fracture under conditions simulating the rise of hydrated gas bubbles in deep water," *Chemical Engineering Science*, vol. 116, pp. 109–117, 2014.

[77] E. J. Chua, W. Savidge, R. T. Short, A. M. Cardenas-Valencia, and R. W. Fulweiler, "A Review of the Emerging Field of Underwater Mass Spectrometry," *Frontiers in Marine Science*, vol. 3, no. November, pp. 1–24, 2016.

[78] J. Severinghaus and T. Atwater, "Cenozoic Geometry and Thermal State of the Subducting Slabs Beneath Western North America," in *Basin and Range Extensional Tectonics Near the Latitude of Las Vegas, Nevada* (B. P. Wernicke, ed.), ch. 1, pp. 1–22, Boulder: The Geological Society of America, Inc., 1990.

[79] C. DeMets, R. G. Gordon, and D. F. Argus, "Geologically current plate motions," *Geophysical Journal International*, vol. 181, no. 1, pp. 1–80, 2010.

[80] H. Menard, "Fragmentation of the Farallon Plate by Pivoting Subduction," *The Journal of Geology*, vol. 86, no. 1, pp. 99–110, 1978.

[81] W. Wilcock, E. Solomon, E. Davis, and A. Trehu, "Investigating Cascadia Subduction Zone Geodynamics Through Scientific Ocean Drilling: Report of a Workshop," tech. rep., University of Washington, Seattle, 2015.

[82] S. D. Wankel, Y. W. Huang, M. Gupta, R. Provencal, J. B. Leen, A. Fahrland, C. Vidoudez, and P. R. Girguis, "Characterizing the distribution of methane sources and cycling in the deep sea via in situ stable isotope analysis," *Environmental Science and Technology*, vol. 47, no. 3, pp. 1478–1486, 2013.

[83] T. Gentz and M. Schlüter, "Underwater cryotrap-membrane inlet system (CT-MIS) for improved in situ analysis of gases," *Limnology and Oceanography: Methods*, vol. 10, no. 5, pp. 317–328, 2012.

[84] T. C. Merket and L. G. Toy, "Comparison of hydrogen sulfide transport properties in fluorinated and nonfluorinated polymers," *Macromolecules*, vol. 39, no. 22, pp. 7591–7600, 2006.

[85] J. F. Clark, I. Leifer, L. Washburn, and B. P. Luyendyk, "Compositional changes in natural gas bubble plumes: Observations from the coal oil Point marine hydrocarbon seep field," *Geo-Marine Letters*, vol. 23, no. 3-4, pp. 187–193, 2003.